FAKULTÄT FÜR PHYSIK

A beam detector for pion experiments and analysis of the inclusive Λ production in proton-proton reactions with HADES

Rafał Tomasz Lalik

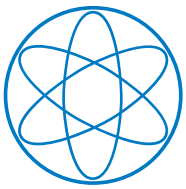

DER TECHNISCHEN UNIVERSITÄT MÜNCHEN

FACHBEREICH: DENSE AND STRANGE HADRONIC MATTER (E62)

2016

FAKULTÄT FÜR PHYSIK

DER TECHNISCHEN UNIVERSITÄT MÜNCHEN

FACHBEREICH: DENSE AND STRANGE HADRONIC MATTER (E62)

A beam detector for pion experiments and analysis of the inclusive Λ production in proton-proton reactions with HADES

Rafał Tomasz Lalik

Vollständiger Abdruck der von der Fakultät für Physik der Technischen Universität München zur Erlangung des akademischen Grades eines

Doktors der Naturwissenschaften (Dr. rer. nat.)

genehmigten Dissertation.

Vorsitzender:	Prof. Dr. Norbert Kaiser
Prüfer der Dissertation:	1. Prof. Dr. Laura Fabbietti
	2. Prof. Dr. Lothar Oberauer
	3. Prof. Dr. Concettina Sfienti (Schriftliche Beurteilung)

Die Dissertation wurde am 04.05.2016 bei der Technischen Universität München eingereicht und durch die Fakultät für Physik am 02.06.2016 angenommen.

Zusamenfassung

Die vorliegende Arbeit befasst sich mit zwei Fragestellungen, die im Rahmen des Messprogramms der HADES Kollaboration behandelt verden.

In ersten Teil wird die Entwicklung eines Detektorsystems zur Überwachung und Spurverfolgung von sekundären Pionen-Strahlen dargestellt. Dabei wird auf die verschiedenen Anforderungen im Hinblick auf Zählratenfestigkeit, Strahl-eigenschaften, Vakuumbetrieb u.a. eingegangen.

Zwei Detektorstationen aus jeweils einem doppelseitigen Siliziumstreifenzähler mit einer aktiven Fläche von $10\,\mathrm{cm} \times 10\,\mathrm{cm}$ und einer Ortsauflösung von $780\,\mu\mathrm{m}$ wurden im Pionenstrahlexperiment gebaut, getestet und eingesetzt. So wurde eine Impuls-auflösung von unter $5\,\%$ bei einer Strahlintensität von 32×10^6 Teilchen pro Sekunde auf dem gesamten Detektor und 2×10^6 Teilchen pro Sekunde pro Einzelkanal erreicht.

Nachdem im ersten Kapitel das Detektorkonzept und die Impulsrekonstruktion für die Pionen erläutert werden, wird im zweiten Kapitel der Siliziumdetektor und seine Ausleseelektronik im Detail vorgestellt. Dies wird ergänzt durch die Ergebnisse ausführlicher Kalibrationsmessungen im Labor. Danach werden die Erfahrungen und Resultate von zwei Strahlzeiten vorgestellt und Ergebnise der Strahlimpulsrekonstruktion diskutiert.

Der zweite Teil der Arbeit enthält die Ergebnisse zur inklusiven Produktion von Λ-Hyperonen, die für die Reaktion pp bei einer kinetischen Energie $E_p = 3.5\,\mathrm{GeV}$ mit dem HADES Spektrometer gemessen wurden. Neben differentiellen Wirkungsguerschnitten werden auch die verschiedenen Reaktionskanäle diskutiert, die zur Λ-Produktion führen, und mit Vorhersagen aus Modellrechnungen konfrontiert. Ein spezieller Fokus wird dabei auf die zur totalen Produktion beitragenden Resonanzen gelegt.

Das erste Ziel wird durch Messung der Impuls- und Ortsverteilungen der produzierten Λ erreicht. Hierauf werden Korrekturen der Detektoreffizienz und Akzeptanz angewendet. Das zweite kann durch den Vergleich der erhaltenen Ergebnisse mit Modellrechnungen zur Lambda Produktion verifiziert werden. So kann schließlich ein totaler Lambda-Hyperon Produktions Wirkungsquerschnitt von $\sigma(\mathrm{pp} \to \Lambda + X) = 201.3 \pm 1.3\,^{+6.0}_{-7.3} \pm 8.1\,^{+0.4}_{-0.4}\,\mu\mathrm{b}$ aus den Daten extrahiert werden, bei dem die Winkel-Anisotropie durch Legendre Polynome angegeben wird.

Im ersten Kapitel dieses Teils wird kurz das HADES-Spektrometer vorgestellt und die physikalische Fragestellung motiviert. Die Signalrekonstruktion sowie die notwendi-

gen Korrekturen zur Nachweiseffizienz und Raumwinkelakzeptanz werden in den beiden folgenden Kapiteln behandelt. Im letzten Kapitel werden dann die Wirkungsquerschnitte und Modellergebnisse vorgestellt und diskutiert.

Preface

This thesis presents the work focused on two topics related to the physics performed at the HADES detector.

In the first part, the development of the tracking detector playing an important role of online beam monitoring and the momentum reconstruction device in the secondary pion beam experiment is presented. Such a detector must fulfill various requirements regarding the operation in the vacuum, with accelerator beams and high count rates. Two detection stations employing double sided silicons strip sensors with an active area of $10\,\mathrm{cm} \times 10\,\mathrm{cm}$ and position resolution of $780\,\mu\mathrm{m}$, providing momentum resolution below $0.5\,\%$ and capable for operating with beams up to $32 \times 10^6\,\mathrm{particles/s}$ total and $2 \times 10^6\,\mathrm{particles/s}$ in a single channel have been constructed, tested and used in the pion beam experiments.

In the first chapter, general information about the production of the secondary, in particular, pion beams is presented. Further, description how the momentum is reconstructed using the information obtained from the tracking detector, and description of most important components of the system, namely the silicon sensor and front end electronics used for its readout is presented. In the second chapter, development of the detector, including all the components used or constructed for this particular purpose is presented. This section also includes description of the laboratory tests and calibrations performed to characterize the detector. In the end of the section, results from two of the beam runs employed for the tests of the detector are presented and discussed. The last third chapter presents results from the commissioning of the tracking detector in the final configuration. Momentum reconstruction feasibility is presented.

The second part of the thesis focuses on the analysis of inclusice production of the Λ hyperons in the nuclear reactions at the HADES energies. The aims of the analysis are to extract the differential cross-section of Λ production in pp center of mass system and pin down contributions of a various production channels, with special focus on the resonances contributing to the total production. The first goal is obtained by finding the momentum and the spatial distributions of the produced Λs and applying corrections emerging from detector efficiency and acceptance to the data. The second one can be verified by comparing obtained results with the Λ production model applied for the analysis. In the end, a total Λ-hyperon production cross-section of $\sigma(\mathrm{pp} \to \Lambda + X) = 201.3 \pm 1.3\,^{+6.0}_{-7.3} \pm 8.1\,^{+0.4}_{-0.4}\,\mu\mathrm{b}$ with the angular anizotropy expressed in terms of Leg-

endre polynomials have been extracted from the data.

In the first chapter of this part, general physics which motivates this analysis is presented, and brief description of the HADES detector is presented. In the next chapter, procedures of the signal reconstruction from the collected experimental data are described. The third section describes the production model used for comparision with the data and preparing all data corrections. The fourth section presents the differential analysis of the data and of the model, in the end comparision of these both data samples is presented and final results of the cross section extraction is presented.

Contents

Part I Pion Beam detector

Part I

Pion Beam detector

1

Introduction to pion beam at HADES

Most of the experiments performed at accelerators around the world use regular matter which can be found all around us, e.g. electrons, protons and even neutrons. Those are the only stable particles present and predicted (quark constituents of hadrons) by the Standard Model. While the employment of these particle species as accelerated beams is meanwhile rather straightforward with our scientific infrastructures and technologies, it becomes more complicated to perform experiment with anti-particles or non-stable particles. Usually we speak here about leptons like μ and ν, π or K mesons, anti-protons or anti-particles in general. Though they are available in cosmic radiation, it is nearly impossible to use them in well controlled initial conditions. Another way to use them is to produce them in nuclear reactions using stable particles beams.

For such experiments, so called secondary beam facilities are needed, where a primary beam of protons or ions is impinged on a solid target. In nuclear reactions triggered in such collisions, a large amount of nucleons, pions, Kaons, leptons and also antiparticles is produced. Cone-like shaped flux of secondary particles follows the direction of the impacting beam. By adjusting the properties of the beam and the target (e.g. the atomic number and the beam energy, etc.) one can optimize the production of the species of interest.

Produced charged particles are captured by properly adjusted system of magnets: quadrupoles and dipoles, and guided further to the experimental site. The role of quadrupole is to re-focus the flux of particles flying in most forward direction, whereas the rest of the flux is usually lost.

A secondary beam is composed of different, neutral and charged particles and has a rather achromatic energy spectrum, whereas experiments are usually performed with a

specific kind of particle and a rather precisely defined energy. Therefore dipoles are used as momentum separators, allowing to choose the appropriate polarity and momentum of the secondary beam particles. The quality of the secondary beam at the destination place (experimental target) depends on many factors. In general, the longer the secondary beam line, the more narrower the energetic spectrum of certain particle species is obtained along with a reduced beam flux. The flux decrease has two main rasons. First of all there is the momentum acceptance of the beam line, related to the magnets configuration in the beam line. The second source is related to limited life-time of the exotic species, which will continuously decay along the way to the experimental hall.

1.1 Pion beam at HADES

In general, secondary beam facilities are composed of three main components: *1*) a primary beam accelerator, typical accelerators used also for usual monochromatic beam experiments; *2*) a secondary beam production target, in which primary beam hits thick nuclear targets; *3*) and a secondary beam transport infrastructure. The last component of the beam line plays the role of momentum separator for the secondary beam.

The production target sees the nuclear reactions at high primary beam intensities, hence a very efficient shielding against radiation must be provided in the surrounding region. Production targets often share the same beam line with primary beams runs, and such target must be removable from the beam line.

There are many facilities around the world providing secondary beams. One of them is located GSI Darmstadt, which accelerator infrastructure is shown in Fig. 1.1. It consists of linear accelerator UNILAC which accelerates beam up to $11.4\,\mathrm{MeV/u}$ kinetic energy. The next accelerating stage, SIS18 synchrotron, accelerates beams further to

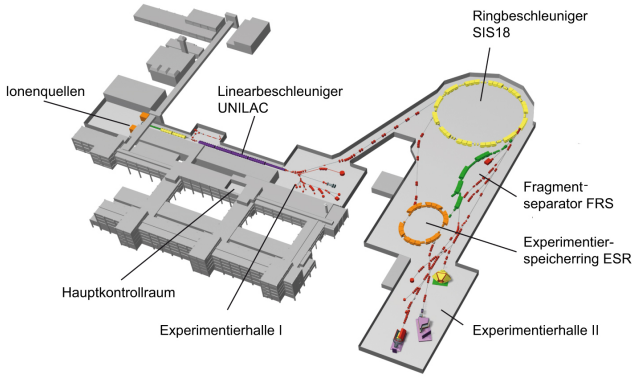

Figure 1.1: Drawing of the accelerator infrastructure in GSI Darmstadt [Dar].

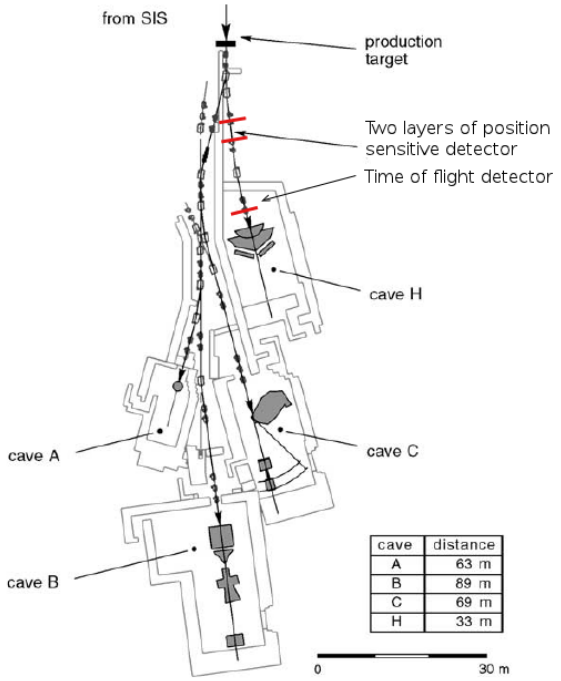

Figure 1.2: Technical drawing of the pion production facility in GSI Darmstadt. From [Dıa+02].

kinetic energy of 3.5 GeV for protons and 1.25 GeV for Au ions. GSI runs experiments employing primary beams from both of the accelerating stages.

GSI has two operating infrastructures for producing secondary beams. The first one, together for Fragment-Separator (FRS), is dedicated to radioactive beams of heavy elements and is used for study of exotic nuclei. The second hosts a production target and a transport chicane for secondary pion beams that can be transported to the FOPI and HADES experiments. A drawing of the infrastructure for pion beam production is shown in Fig. 1.2. Cave H and B show the location of the HADES and FOPI experiments, respectively.. The SIS18 synchrotron, delivering primary beam to the production target, is not shown in the figure and is located above the picture (arrow indicates direction of the beam).

The pion production target was constructed for the pion experiment at HADES. The beam line part between the production target and the HADES target is called pion chicane and is presented in Fig. 1.3.

The production target, shown in Fig. 1.4 is surrounded by thick walls made of concrete blocks shielding the outer area from high radiation generated in the target during pion production. The target is mounted on a vertical arm, which can be lifted up and down to remove or put target into the beam axis. Accessing the target requires dismounting of the concrete walls.

Elements Q1 to Q9 in Fig. 1.3 are quadrupoles focusing the incoming beam. FOPI denotes the dipole used to drive the beam to the cave B where the FOPI experiment

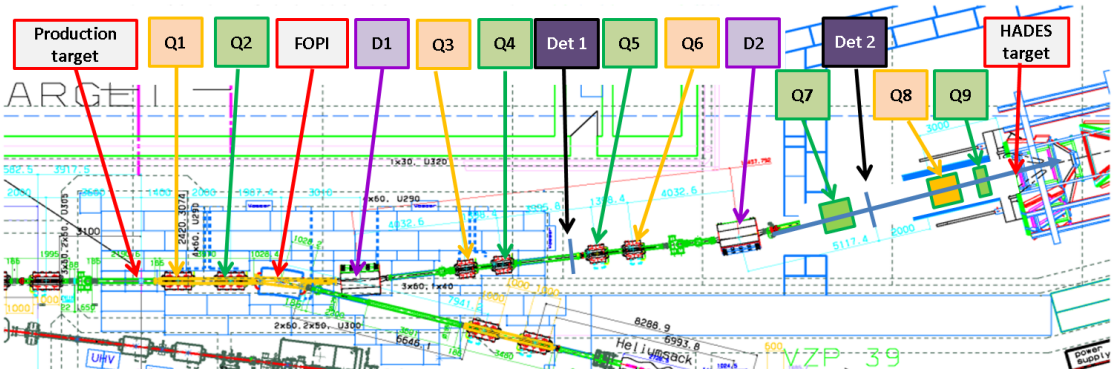

Figure 1.3: Drawing of the pion chicane at SIS18 in GSI Darmstadt.

was located. Dipoles D1 and D2 drive particles of primary and secondary beams to the HADES cave. Det1 and Det2 depicts the locations of the tracking detectors employed in the pion experiments. Detector Det1 is located in the NE5 area of GSI. Det2 is placed inside HADES cave and dedicated locations for the pion tracker tracking stations. Pion beam line was commissioned in 2002 [Dıa+02].

The production of the negative pion beam is initiated by colliding primary Nitrogen beam on Beryllium target. The maximum beam intensity of Nitrogen ions at SIS18 is 5×10^{11} particles/spill, where one spill is 4 s long. The pions intensity at the HADES target depends on selected central momentum and reaches maximum of 5×10^6 part /spill at 1 GeV/c momentum (Fig. 1.5). At 1.7 GeV beam momentum, intensity of pions drops to 2×10^6 particles/spill. Although thess measurements were done with a primary Carbon beam, values for Nitrogen will be similar due to similar atomic mass.

The beam line transmission for the central momentum was calculated to be $\approx 85\,\%$ at the first Det1 location and $\approx 56\,\%$ at the HADES target. The overall transmission to

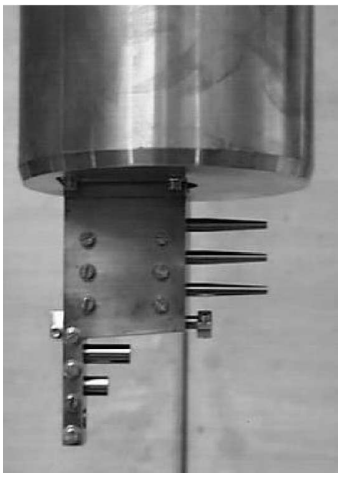

Figure 1.4: Production target in the holder. From [Dıa+02].

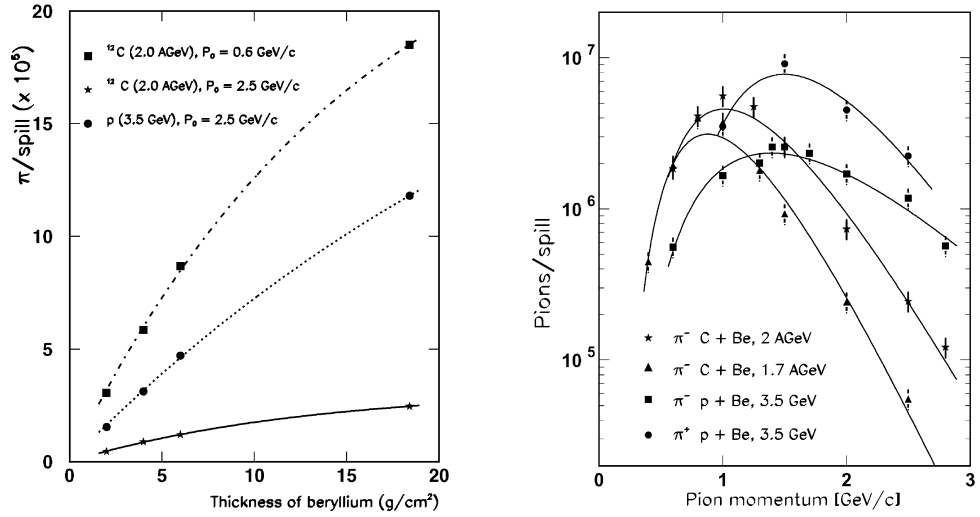

Figure 1.5: Intensity of pions at the HADES target for different (left) primary target thickness and (right) primary beams types and energies. From [Dıa+02].

the HADES target for a range of the beam momentum $\pm 6\,\%$ around the central value is estimated to be $18.6\,\%$. The same calculations estimate the rate at D1 to be five times higher than at the target position. Additionally beam line acceptance is bigger at the Det1 location. One can then safely assume that beam rates at the first detector station are ten times bigger that at the HADES target.

1.2 Beam transport

The transport of particles in the beam line can be described using the properties of the optical elements. Each part of the beam line, magnet, quadrupole, pipe, can be represented by equivalent optic (lens) element, e.g. a dipole can be described by a prism and quadrupole pairs by pairs of focusing and defocusing lenses. In the first approximation, all magnets can be treated as thin lenses. For very fast particles, lengths of the magnets of order of $1\,\mathrm{m}$ are very small with respect to the particles velocity and hence with the time the particles are interacting with magnetic fields. Hence higher order effects like achromacity can be abandoned. In reality, the magnets parameters are particle momentum dependent, similar like the lens properties, namely the refraction index $n(\lambda)$ is wavelength dependent, and if aiming for higher precision, they must be also considered. A complete study of the beam transport theorem is presented by in [Bro68].

In its usual notation, and in the absence of acceleration devices, each particle is described by a six-dimensional vector:

$$\vec{X} = (x, \theta, y, \phi, l, \delta)\,, \tag{1.1}$$

where x and y are the spatial coordinates of the particle, θ and ϕ are the horizontal and vertical angles defined as $\tan\theta = \frac{\mathrm{d}x}{\mathrm{d}z} = \frac{p_x}{p_z}$ and $\tan\phi = \frac{\mathrm{d}y}{\mathrm{d}z} = \frac{p_y}{p_z}$, and represent the flight direction. $\delta = (p_0 - p)/p_0$ denots the deflection from the central beam momentum p_0. The value l describes the path length difference between any arbitrary path and the central trajectory and usually is set to 0.

Each beam line element, e.g. magnet or vacuum pipe, is described by the first and the second order matrices T_{ij} and T_{ijk}. The particle transport from the initial point $\vec{X(0)}$ to the exit of the element can be parametrized as follows:

$$X_i = \sum_{j=1,6} T_{ij} \cdot X_j(0) + \sum_{\substack{j=1,6 \\ k=j,6}} T_{ijk} \cdot X_j(0) X_k(0), \tag{1.2}$$

where i enumerates the $\vec{X}$ vector coordinates in range 1 to 6.

The commissioning of the GSI pion beam in 2002 showed that the acceptance of the beam line is around $10\,\%$ [Dıa+02]. It means that for a selected central momentum, the spread of the pions momenta at the target will be $10\,\%$ in each direction. For performing precise measurements with dilepton exclusive reaction channels resolution on level of $0.5\,\%$ is required[Bie+15][1].

It was shown in [Bie+15][2] that by measuring the particle position at two independent locations, and by omitting third-order effects and contributions smaller than half of the effects resulting from the resolution of position measurements, Eq. (1.2) can be solved and the particle position at the HADES experimental target can be calculated. Finally, this allows to calculate the reaction geometry in the target. The precision of the calculations depends on the precise position measurement and determination of the transport coefficients. If the detector sits at the beam line dispersive plane, its momentum measurement resolution is independent from the hit position on the detector. In case of pion tracker, the first detector was located downstream the dispersive plane to leave place for thicker shielding of the production target. This lead to a momentum resolution dependent on the hit position on the detector. This effect is seen in the results of the proton beam calibration during the commissioning of the pion tracker.

The calculation procedure is iterative. In the first stage, from two position measurements $\vec{X}$ and $\vec{X}'$, the initial coordinates $\vec{X}(0)$ at the beginning of the beam line are

[1] Chapter 1.
[2] Chapter 2.

calculated with following set of equations:

$$\begin{cases} X &= T_{12}\cdot\theta_0 + T_{14}\cdot\varphi_0 + T_{16}\cdot\delta + \\ & \quad T_{126}\cdot\theta_0\delta + T_{146}\cdot\varphi_0\delta + T_{166}\cdot\delta^2 \\ X^{'} &= T^{'}_{12}\cdot\theta_0 + T^{'}_{14}\cdot\varphi_0 + T^{'}_{16}\cdot\delta + \\ & \quad T^{'}_{126}\cdot\theta_0\delta + T^{'}_{146}\cdot\varphi_0 + T^{'}_{166}\cdot\delta^2 \\ Y &= T_{32}\cdot\theta_0 + T_{33}\cdot y_0 + T_{34}\cdot\varphi_0 + T_{36}\cdot\delta + \\ & \quad T_{336}\cdot y_0\delta + T_{346}\cdot\varphi_0\delta + T_{366}\cdot\delta^2 \\ Y^{'} &= T^{'}_{32}\cdot\theta_0 + T^{'}_{33}\cdot y_0 + T^{'}_{34}\cdot\varphi_0 + T^{'}_{36}\cdot\delta + \\ & \quad T^{'}_{336}\cdot y_0 + T^{'}_{346}\cdot\varphi_0\delta + T^{'}_{366}\cdot\delta^2, \end{cases} \tag{1.3}$$

where variables and coefficients are those from Eqs. (1.1) and (1.2).

Since there are five unknown parameters in the vector $\vec{X}$ and only four independent coordinate measurements, one of the parameters with least significance is neglected, here it is $x_0 = 0$ which has smallest coupling to the horizontal terms.

As a next step, coordinates at the HADES target can be found using initial values of the beam particle:

$$\begin{aligned} \theta_H &= T^{\mathrm{H}}_{22}\cdot\theta_0 + T^{\mathrm{H}}_{23}\cdot y_0 + T^{\mathrm{H}}_{26}\cdot\delta \\ &\quad + T^{\mathrm{H}}_{226}\cdot\theta_0\delta + T^{\mathrm{H}}_{246}\cdot\varphi_0\delta + T^{\mathrm{H}}_{266}\cdot\delta^2, \\ \varphi_H &= T^{\mathrm{H}}_{42}\cdot\theta_0 + T^{\mathrm{H}}_{43}\cdot y_0 + T^{\mathrm{H}}_{44}\cdot\varphi_0 + T^{\mathrm{H}}_{46}\cdot\delta \\ &\quad + T^{\mathrm{H}}_{426}\cdot\theta_0\delta + T^{\mathrm{H}}_{436}\cdot y_0\delta + T^{\mathrm{H}}_{446}\cdot\varphi_0\delta + T^{\mathrm{H}}_{466}\cdot\delta^2. \end{aligned} \tag{1.4}$$

The relevant quantities for kinematical reconstruction of the events, p_x, p_y and p_z at the HADES target, are derived from the values of θ_0, φ_0 and δ through the formulae:

$$\begin{aligned} p &= p_{spec}(1+\delta), \\ p_x &= {}^{p\tan(\theta_H)}\big/\sqrt{1+\tan^2(\theta_H)+\tan^2(\varphi_H)}, \\ p_y &= {}^{p\tan(\varphi_H)}\big/\sqrt{1+\tan^2(\theta_H)+\tan^2(\varphi_H)}, \\ p_z &= {}^{p}\big/\sqrt{1+\tan^2(\theta_H)+\tan^2(\varphi_H)}. \end{aligned} \tag{1.5}$$

where θ_H and φ_H were obtained from the previous step. All the T_{ij} and T_{ijk} coefficients used in formulas above are obtained from the beam transport calculation. Details of the alculations and values of the coefficients are given in [Bie+15].

1.3 Beam detector

A successful determination of the pion momentum requires the measurement of the pion position at two different and carefully selected locations along the beam line. A scheme of the tracking setup is shown in Fig. 1.6. The two silicon detectors measure the particle position and the Start detector provides the reference time information for TOF detectors

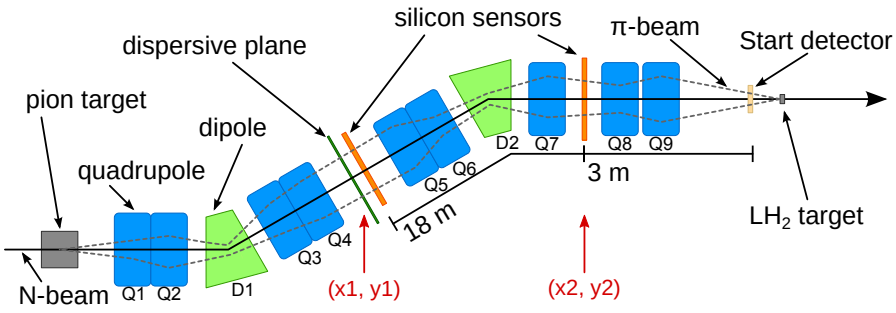

Figure 1.6: Tracking setup at the HADES pion beam.

at HADES. The pion beam interacts with the liquid hydrogen LH_2 or with the solid target in the HADES detector.

The beam detectors employed for this task must fulfill several demanding requirements. First of all, must cope with beam rates on order of $10^7\,\mathrm{counts/s}$ at the first tracking station. This limit results from the pion rates measured during commissioning of the pion beam, presented already in the introduction. High beam intensity over many days of beam taking requires radiation hard detectors and work in a high vacuum environment. The size of the beam spot determines required active detection area. From the simulations, a beam spots of $8\,\mathrm{cm} \times 4\,\mathrm{cm}$ and $8\,\mathrm{cm} \times 8\,\mathrm{cm}$ on the first and second location respectively have been determined. The beam intensity distributions at different locations along the beam line are shown if figure Fig. 1.7.

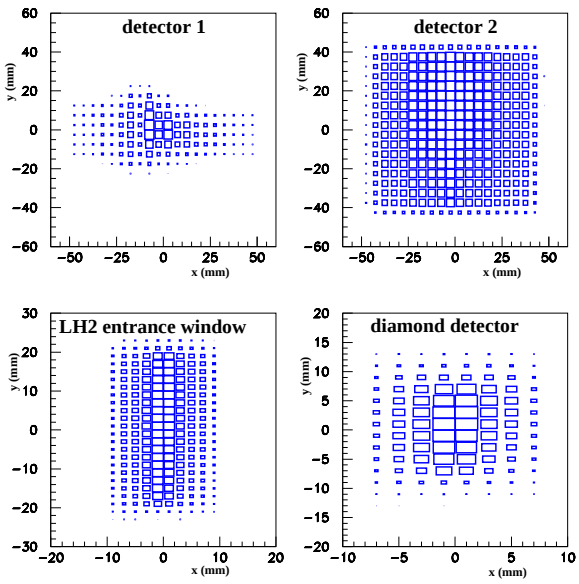

Figure 1.7: Occupancy distribution at the different locations in the beam line, starting from top left and clockwise: the first detector station, the second detector station, the diamond start detector, the LH_2 target entrance window. Z-axis, represented by squares, is linear. From [Bie+15].

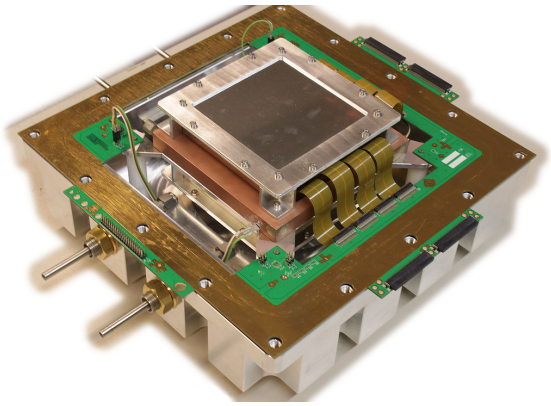

Figure 1.8: Phto of single tracking station with removed upper halve of the detector chamber.

To fullfil above requirements, a pion tracker beam detector called CERBEROS[3] consisting of two tracking stations, each of exactly the same design, has been constructed at TUM. A photo of one of the two tracking stations is shown in Fig. 1.8.

The core part of a single tracking station is a double-sided silicon strip sensor with an active area of $10\,\mathrm{cm} \times 10\,\mathrm{cm}$ and enhanced radiation hardness having a p-type bulk. As a solid state detector, it can work in vacuum conditions. The sensor is further read-out by two front-end electronics modules with the n-XYTER chip [Bro+06].

The front end electronics send out digitized data, which are collected by a TRB3 readout board [Tra+11]. The TRB3 provides a trigger and data-readout interface for the data acquisition, and integrates the tracking stations into HADES control, trigger and acquisition network.

Three working groups were involved in the development of the pion tracker system components. The group, in which author of this thesis was involved, was responsible for: *(i)* testing of the silicon sensors and front end electronics, *(ii)* construction of the vacuum chambers and cooling systems for both tracking stations, *(iii)* assembling the chambers and performing all required tests, *(iv)* preparing software for system control and monitoring, *(v)* writing libraries for unpacking the data, calibration and momentum reconstruction in the data analysis framework. A second group, working on TU Munich and in GSI Darmstadt was responsible for integration of the n-XYTER readout in the TRB3 readout system. A third working group from IPN Orsay and UJ Kraków was responsible for pion beam transport calculations and simulations.

1.3.1 Silicon sensors

Silicon sensor is an example of asymmetric pn-junction working in reverse bias mode. An asymmetric junction is made of two layers of semiconducting material, typically sil-

[3] Central Beam Tracker for Pions.

icon[4], doped with charge donor atoms for n-type and with charge acceptor atoms for p-type. A charge donor is a material whose Z-charge number is higher than of the base semiconductor and this provides extra electron to the conduction band. A charge acceptor is a material with a smaller Z number generating holes in the valence band. Doping of the silicon can be done either during crystal growing process or after the wafer is created. In the silicon sensor production, the second method is used.

Standard process of a silicon wafer production with Czochralski method [Czo18] used in the electronics chip industry results with to many inpurities in the silicon and is not sufficient for a silicon sensor. Instead, a Float Zone process of producing a high purity silicon monocristals is used [Mer; Rio97].

Production of typical pn asymmetric (n is a bulk) silicon sensor is initiated with the creation of n-doped silicon wafers. The thickness of the layer determines the final thickness of the detector and typically is equal to $300\,\mu\mathrm{m}$. In the next step, a thin layer of p-doped semiconductor with a concentration of acceptors N_a is created on one side of the crystal (the junction side). Typically the p-type layer has thickness of $10\,\mu\mathrm{m}$. Concentrations are adjusted to obey simple relation of $d_d N_d = d_a N_a$, where d_a and d_d are the thicknesses of donor and acceptor layers. The connection between both silicon layers is called a junction. The opposite side is called ohmic side. On the end, both sides of the sensor are doped with higher concentrations of donors and acceptors respectively, to form the conductive readout structures like strips or pads. Depending on the technology, whether this is DC or AC coupled sensor, additional layers of insulators, semiconductors or metals can be added. Review of the silicon sensors production, types and properties can be found in excellend book of Lutz in [Lut07].

Free charge carriers in the region of the pn junction recombine and create charge free depletion layer. Since the junction is asymmetric and the concentration of charge carriers in the thicker layer is lower, the depletion zone arises strongly in the n-type direction direction. Charges located away from the junction, and which did not recombine, create an intrinsic electric field in the junction region. The size of the junction can be modified by applying external biasing. The junction is polarized in the conduction direction, by applying higher potential on the p-type side. Both charges move along an external field toward the junction, where the recombination process starts and the current is flowing through the junction. If the junction is polarized in reverse mode by applying higher potential on the n-type side, an external electric field pushes charges away from junction. Hence, free of charge the depletion zone is increased in size. The stronger the field, the bigger the depletion zone, which can be enlarged to the total thickness of the n-type detector detector. This is the so called full depletion operation.

The depleted layer is the active detection volume in the sensor. Charged particle

[4]For high resolution atomic and nuclear experiments germanium is used. It has lower ionization energy and therefore allows for production of higher numbers of electron-holes pairs and much better energy resolution, but requires strong cooling against thermal charge generation.

traversing this area ionizes atoms creating free pairs of charge carriers: electrons and holes. These charge carriers, undergo the electric field and drift in opposite directions. When reaching the edges of the detector, they are collected by electrodes and read out in the attached electronics.

At room temperatures the thermal energy of the electrons in the crystal lattice is high enough to trigger spontaneous pair generation. These free carriers are also collected by electrodes and contribute to the leakage current of the sensor, worsening the energy resolution of the measurement. The thermal current depends on the temperature T and the energy band gap E_g of the silicon, and follows $I_0 \sim T^2 \exp\left(-E_g/2k_BT\right)$ law. The energy resolution of the whole detector can be improved by the sensor temperature reduction.

Energy deposition in silicon sensors

The energy deposition mechanism described by Bethe and Ashkin in [BA53] is based on the energy transfer between the projectile and the valence electrons of the traversed medium. The amount of energy transferred from a projectile to the valence electron in a single interaction is proportional to the *impact parameter* b defined as the closest distance between the projectile and the atom in the medium. The amount of energy is proportional to the of the path length $\mathrm{d}x$ of the particle in the active detection volume.

The stopping power, which express how much energy the particle is loosing while traversing the medium, depends on additional factors, like generation of δ-electrons, radioactive looses, radiative energy emission.

In general, the energy deposition mechanism is universal and valid for various par-

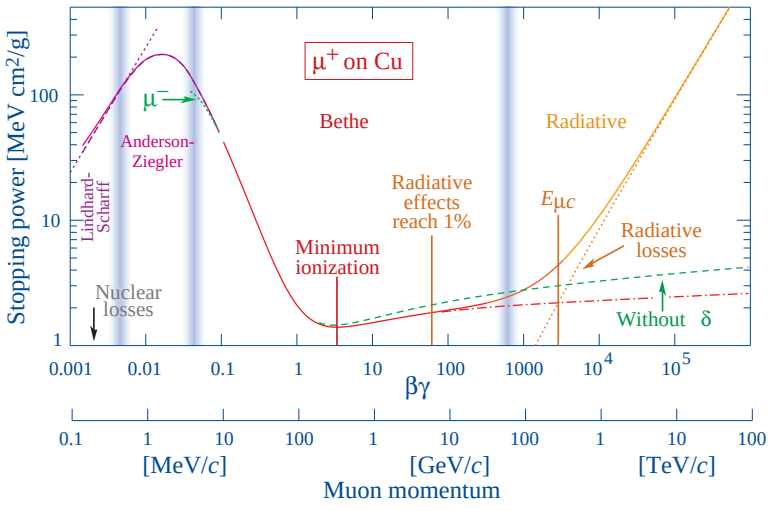

Figure 1.9: Energy deposition of muon in the Copper. From [Oli+14].

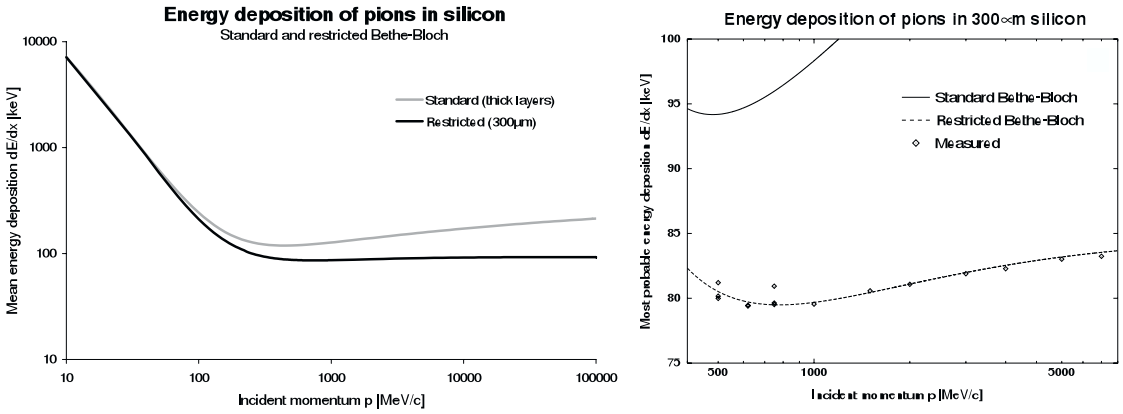

(a) **(b)**

Figure 1.10: Energy deposition in silicon for pions: (a) theoretical and (b) measured. From [Fri01]

ticles, ions and materials. Figure 1.9 show example of the stopping power for muons in Copper.

While Bethe formula describes the average energy deposition in the material, the amount of energy deposited by the particle follows the Landau distribution [Lan44].

In a thin layer like $300\,\mu\mathrm{m}$ thick silicon detector, the particles traversing the detector area are knocking out δ-electrons. These electrons have a certain probability to not be reabsorbed in the active volume and therefore can carry away part of the energy lost by pions. This effect is proportional to the momentum and leads to growing decrease of the energy measured in the detector and corrections in the deposition curve lead to the *restricted formula* (thick black line in the figure).

This effect was measured at BNL by HEPHY and MIT groups [Fri01]. Figure 1.10b shows the relation between the theoretical curve and the measured values. The effect of the thin layer leads to an effective move of the minimum-ionizing point from $450\,\mathrm{MeV/c}$ to $750\,\mathrm{MeV/c}$.

Measurements at HADES are planned at $0.8\,\mathrm{GeV/c}$ for LH_2 (or polyethylen) target and at $1.6\,\mathrm{GeV/c}$ for solid targets. In the first case pions are considered to be minimum ionizing. Although at $1.6\,\mathrm{GeV/c}$ radiative loses start to play a role, their influence is negligible at this momentum value. For the both momentum values pions will therefore deposit around $80\,\mathrm{keV}$ of the energy.

1.3.2 The n-XYTER Front-End Electronics Readout

The n-XYTER [Bro+06] ASIC is an example of a modern readout electronics systems for silicon detectors readout. It was designed for neutron experiments by the DETNI collaboration. The name n-XYTER itself stands for *(neutron) X, Y, Time and Energy*

Readout. The internal architecture of the n-XYTER is presented in Fig. 1.11.

n-XYTER has 128 individual, self-triggered signal channels allowing to work with either positive or negative signal polarities, configurable in the chip logic. Self-triggering requires that each channel has his own trigger logic, based on the energy discriminator, though the reference value for the discriminator is common for all channels. Input signals for which a trigger decision is positive, are accepted and a time-stamp is assigned to the event by an internal clock. Afterwards, it is stored in the internal FIFO register of four words length for each channel.

The signal used for discriminating is generated by the fast shaper circuit, which is optimized for time determination (cooperates with time-stamp tagging logic). The shaper has a peaking time of $18.5\,\mathrm{ns}$, the base-line restoring to $10\,\%$ level is amplitude dependent and takes up to $100\,\mathrm{ns}$ for maximum input signals. Simultaneously, the energy is measured in a parallel slow shaper circuit, optimized for energy resolution with ENC[5] of $12.7\,\mathrm{e/pF} + 233\,\mathrm{e}$ and a peaking time of the order of $170\,\mathrm{ns}$ [Tru]. The decay can takes up to $700\,\mathrm{ns}$.

Since the base line restoring times of the slow and fast circuit differ almost by one order of magnitude, there is a risk that the fast shaper can register two or more proper input signal while the slow shaper will experience significant pile-up. Therefore, for each channel a single monostable generator triggered by the discriminator is implemented. If a second trigger appears during monostable period, the second event is discarded. Due to pile-up effects in the slow shaper, the first event is marked with a *pile-up* flag, alerting about possible error in the energy measurement.

[5]Equivalent Noise Charge, describes the intrinsic noise of the electronics device. The ENC value expresses the number of electrons on the input generating the same response like intrinsic noise does.

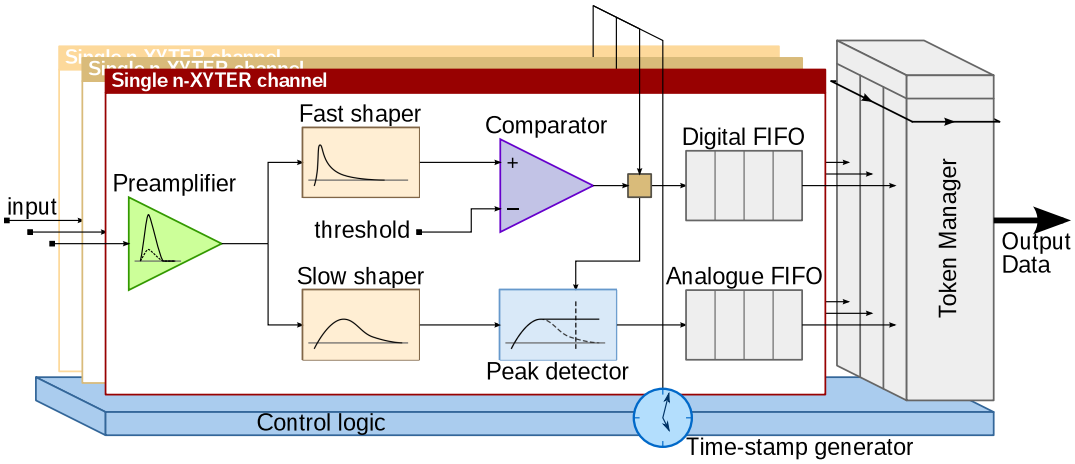

Figure 1.11: Block diagram of the n-XYTER architecture.

The energy is measured using the Peak Hold logic, which detects the highest amplitude registered on its input during the monostable period. The length of the monostable determines therefore the dead time of the single channel, and varies in a range from $100\,\mathrm{ns}$ to $4000\,\mathrm{ns}$. Since themonostable is individual for each channel, it assures that the other channels are all time ready to measure incoming events. The read time introduced by the monostable is not re-triggerable, which means that the monostable is not extended by the pile-up events.

The analogue information is stored in the analogue FIFO registers of also four words length, parallel and correlated with the digital FIFO for the time-stamp. The presence of these buffers prevents extra dead time related to the chip readout.

The peak detector can work only with a positive input signal, therefore the slow shaper consists of two stages, which can invert the input signal if needed, depending on the polarity settings of the channel input.

The input range with linear gain of the pre-amplifier is limited to $6\,\mathrm{MIPS}$ (for standard $300\,\mu\mathrm{m}$ silicon sensors). If only the time stamp information is required, the n-XYTER can be operated in saturation mode with higher input signal. Due to the increase of the base-line restoration time, higher input signals reduce the maximal input rate each channel can cope with.

Both four words deep storage FIFO memories are used for buffering and derandomizing of input events. Buffering mean that the data is stored there while the output is busy with sending out data from other channels. The derandomization assures that data is sent with a fixed frequency of $32\,\mathrm{MHz}$, and either valid data frames with hit information, or empty frames are streamed out. To avoid an overflow of the FIFO buffers, the readout (realized by the Token Manager architecture) iterates constantly over all channels, and at each pass only one word from a single buffer is read out. If the buffer is full, all further events are discarded and the last event in the buffer gets an *overflow* flag.

The output contains mixed analogue-digital information, where time stamp, channel number and status flags are sent out in digital pattern, and the energy as an analogue signal. This implies that an external ADC converter must be used together with the n-XYTER chip.

Overall, assuming that all the input channels are operating with the standard readout clock frequency of $256\,\mathrm{MHz}$, the average hit rate per channel is limited to $160\,\mathrm{kHz}$ with a $10\,\%$ dead-time.

Every single analogue channel can be switched off, by a power off procedure. This reduces power consumption, it has however the side effect of changing the working conditions of the neighbour channels. This is due to fact that the chip is implemented on a single silicon crystal (wafer) and parasitic capacitances are present between all channels. Switched off channels translates into different static and the dynamic working point for their neighbours. For this reason, two dummy channels are implemented on both ends of the group of 128 ($+1$ test channel) channels to provide an equal environment for all

channels.

A more effective way to remove single channels from the readout chain is to mask the channel using mask registers, which results in the disconnection of the analogue part of the channel from the FIFO buffers. These channels therefore are not delivering any data to the readout manager. At the same time analogue part of the channel works in his usual way.

n-XYTER control

The n-XYTER is configurable via sets of 32 8-bit registers over an I2C interface. The first sixteen registers control the mask registers array which is 128 bits long, with each bit controlling a single channel. As described above, the masking allows to remove single channels from the internal data readout.

The next 14 registers are DAC[6] register. These registers control working point of the analogue signal processing channels and the settings are common for all the channels.

Despite of the fact that so many registers are accessible to a final user, the settings for most of them were optimized during a preliminary the design and simulation step and default (recommend) values should be used. Among all of them, five registers are of particular importance to the user and should be managed:

- register 18, Vth – controls the threshold of the internal discriminators;
- register 20, VbiasF – controls base line of the output of fast shaper;
- registers 21 and 22, VbiasS and VbiasS2, control the output voltages of both slow shapers outputs, also influence the reference level of the analogue output;
- register 24, cal – controls the amplitude of internal pulse generator.

During the tests it was found that also default value of the register 19 (Vbfb), controlling the feedback resistance in the pre-amplifier stage, must be adjusted to assure proper operation at high beam rates.

Additional two control registers 32 and 33 allow to configure various working parameters of the chip: input polarity, test modes (described below), clock selection, internal pulser configuration, calibration groups. For normal operation this registers usually do not be modified (beside the polarity bit selection), when performing tests they must be reconfigured.

Operating modes

The n-XYTER can be operated in four modes, depending on the settings of the two logic bits: *Test Pulse mode* and *Test Trigger mode*.

When the first bit is set, the rising edge on the External Test Pulse (ETP) input triggers an internal pulse generator coupled to the channel input via a capacitor. The pulser

[6]Digital to Analogue Converter. Digital value of the register is converted into analogue amplitude.

settings allow to inject a charge in a range of $0\,\mathrm{fC}$ to $11.1\,\mathrm{fC}$ ($1\,\mathrm{MIP} \equiv 4\,\mathrm{fC}$ for $300\,\mu\mathrm{m}$ thick silicon detectors). This mode can be used to inject the charge into the channel and verify proper working of the front-end stages.

When the second bit is set, the channel discriminator is bypassed and forces the channel to trigger on the ETP rising edge. Additionally, the status of the discriminator output is stored in the mirror register[7]. In this mode the self-triggering mode of the chip is switched off and the chip works as a triggered device.

All four combinations of testing modes are allowed. When both bits are off, the n-XYTER is working in the normal operation mode.

[7]This read-only register is available as a mask register. When the Test Trigger mode is on, reading out the mask register will give in fact the status of mirror register.

2
Beam Detector Development

Block diagram showing major components used for construction and operation of the single pion tracker detection station is shown in Fig. 2.1. A detailed description of each part is given in following sections.

Each of two stations works standalone, independently from the other one. The system is not limited to two stations and can be extended to any number. This means that each station must have its own, standalone readout system, requiring minimum input from the user. Basically the readout request trigger signal (fast, digital logical signal) and the transfer channel for data acquisition (DAQ) system (fast Ethernet gigabit or optical connection). Though communication is based on the HADES TrbNet protocol, the FPGA logic used in the readout devices allows for reprogramming of the communication protocol for any acquisition system supposed to work with the system.

Each silicon sensor is enclosed in a vacuum chamber, equipped with slots allowing to mount the detector station directly on the beam pipe. All detector channels are routed outside the chamber via a feed-through PCB and wired over connectors to the HV adapters and finally to the front-end electronics (fee). The sensor located inside the vacuum chamber is cooled down by two cooling systems: the first one is designed to remove thermal heat from the detector whereas the second one is designed to shield against heat radiation coming from the beam pipe.

In the development process, all components of the vacuum chamber: the cooling infrastructure for the silicon sensors, the vacuum chamber halves, the feed-through PCB and the biasing circuit for the sensors were designed exclusively for the system.

Front-end modules, digital readout, power supply devices for all parts of the system, mini chiller for the cooling system, were available on the market and reused for the

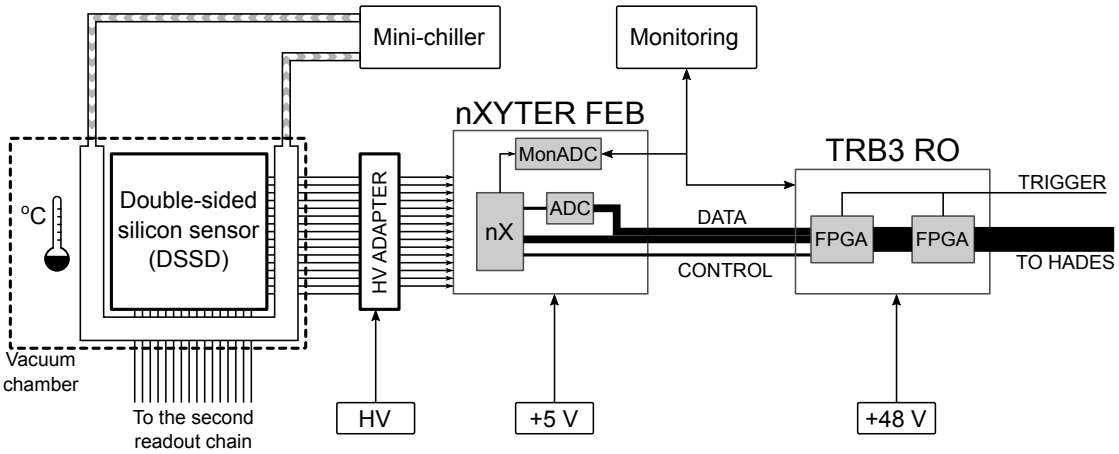

Figure 2.1: Block diagram of single chamber architecture.

system.

During development, several components like light tight shielding boxes, testing PCB boards, prototyping cooling systems were built.

Complementary to the hardware development, several software for detector HV control and monitoring, cooling system, detector calibrations, data unpacking and analysis were developed, and further used in the experiment.

2.1 Silicon Sensors

Silicon sensors (Fig. 2.2) utilized for CERBEROS are p-type double-sided silicon strip sensors produced by Micron Semiconductor Ltd. [Mic] as TTT-3 model and designed primarily as n-type sensors for the MUSETT silicon array for heavy elements spectroscopy [The+14]. The change in the production process from n-type to p-type results

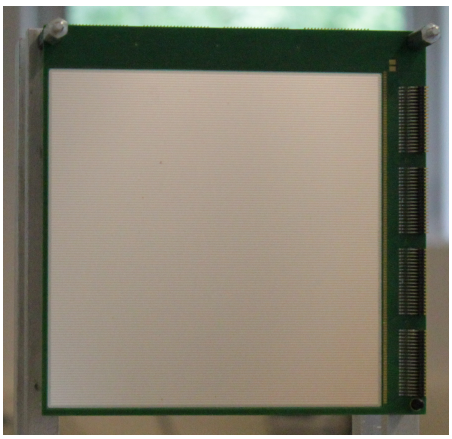

Figure 2.2: Photo of the silicon sensor. Output connectors are seen on the left side and on the top on the other PCB side.

from the required radiation hardness which was especially requested for the development of this detector.

In total, three silicon sensors were used in the prototyping and commissioning of the pion beam measurements. A single sensor has a thickness of $300 \pm 10\,\mu\mathrm{m}$ and active detection area of $10\,\mathrm{cm} \times 10\,\mathrm{cm}$. Both sides are segmented into 128 parallel strips, perpendicular to each other. The width of a single strip is $700\,\mu\mathrm{m}$ with pitch Δ of $760\,\mu\mathrm{m}$ allowing for a position measurement resolution of at least $\Delta/\sqrt{12} = 219\,\mu\mathrm{m}$ with binary readout. A single strip has length of $97.22\,\mathrm{mm}$. Strips are DC-coupled with biasing voltage on level of $60\,\mathrm{V}$ to $70\,\mathrm{V}$.

Sensors are delivered attached to $2.4\,\mathrm{mm}$ thick FR4 printed circuit board (PCB). Strips of the silicon sensor are bonded to copper pads on the PCB. Pads are routed to the Samtec [Sam] connectors (TSM-120-02-L-DH-K) located on the edges of the PCB. Guard rings in this design are not connected and therefore floating.

Although the energy measurement does not play any role in the momentum reconstruction process, its measurement is crucial for the hits reconstruction, especially in high-multiplicity events,where several hits may occur in a single detector. The energy deposited by a single pion follows a Landau distribution [Lan44], and hence is different for each registered hit, but the measurement for a single hit on both sides of the detector should be equal [1]. By matching these values pairwise on both sides of the single detector, one can identify real pairs and reject false coincidences.

2.1.1 Energy resolution

A reference measurement of energy resolution of the detector was performed [Sie13][2]. The Mesytec MPR16 amplifiers [Mesb], designed for the readout of silicon sensors and built out of discrete components, providing a high precision energy measurement were employed in this tests. These measurements constitute a reference for further measurements with final n-XYTER electronics readout.

The readout system allowed for simultaneous measurement of 128 channels only, and 256 channels were available on both sides of the detector. Each two neighboring channels were connected to the single input of the amplifiers to allows for full readout of all the channels.

A ^{207}Bi source was used for the calibration. It emits four discrete electron conversion lines at values of $482\,\mathrm{keV}$, $554\,\mathrm{keV}$, $976\,\mathrm{keV}$ and $1045\,\mathrm{keV}$. Full absorption of the electron results in a monoenergetic peak in the measured energy spectrum, as seen is single channel measurement on Fig. 2.3. Electrons which escaped the detector and therefor were not absorbed, deposited a signal according to the nature of the Landau

[1] Here we assume the energy of the whole reconstructed hit cluster, not the single fired strip of the detector.

[2] Chapter 5.2.

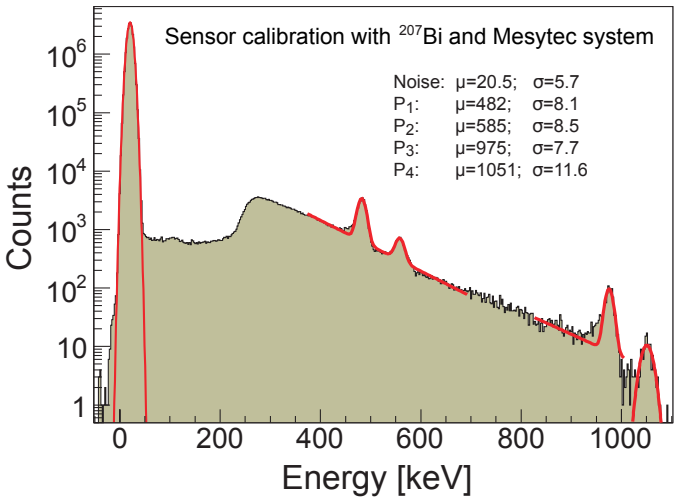

Figure 2.3: Energy spectrum of channel 121 measured with a ^{207}Bi source. The red lines show fits of exponential plus Gaussian functions. The legend indicates the fit results. From [Sie13].

distribution.

The maximum of the charge deposition distribution visible as a small bump on the left from peak P_1 is located at energy of $\approx 300\,\mathrm{keV}$. Since the energy of these electrons are sub-minimal-ionizing ($\beta\gamma < 1.7$), the most probable value of the distribution is located above the MIP value of $120\,\mathrm{keV}$ for the electrons.

The strongest peak at the very low spectrum energy value is attributed to the noise. Each processing channel in the testing setup had the possibility to trigger on the signal input. The discriminator threshold was set above noise level, high enough to avoid triggering on the random noise. All 128 channels were readout for each trigger signal issued by an individual channels, and this is a source of a visible noise peak in the spectrum. Since this is uncorrelated noise, analysis of noise peaks in each channels allowed to determine the width of the noise spectrum for each pair of channels.

The energy resolution of the silicon sensor was estimated to $2.5\,\%$ at $482\,\mathrm{keV}$ peak position. The noise width was measured to be $1470\,\mathrm{e}^-$ to $2350\,\mathrm{e}^-$.

2.1.2 Detector Efficiency

The detector efficiency was measured using ^{90}Sr β-emitter, which was placed with a distance of a few centimetres in front of the silicon sensor. In this measurement, the triggering was realized on external scintillator placed behind the sensor. The area of the trigger detector covered whole area of the sensor. Figure 2.4 shows spot of the β-particles on the detector surface. The deformation from a circle shape results from small tilting of the source in respect to normal vector of sensor surface. The noise (background pattern) of the detector was suppressed by applying the thresholds obtained from the energy resolution measurements.

The efficiency was obtained by comparing the number of hits associated to an energy

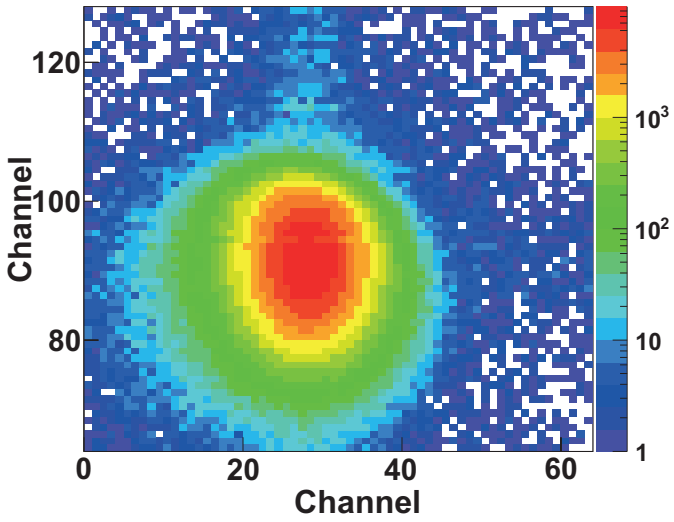

Figure 2.4: Hit pattern in the 2615-7 silicon detector. From [Sie13].

above the threshold to total number of trigger events. The results for all three detectors are presented in Table 2.1. The low efficiency for the third sensor results from one inactive strip in the sensor.

Table 2.1: Efficiency of the three different silicon detectors.

Detector	Efficiency
2615-7	97 %
2814-24	96 %
2814-25	92 %

2.2 Power supply for silicon sensors

The silicon sensor is supplied with voltage by Mesytec MHV-4 [Mesa] power modules. The design of this power device was optimised for the silicon sensors application. It has four independent HV outputs, each can generate a stabilized voltage in two ranges: 0 V to 100 V and 0 V to 400 V, each of them with negative or positive polarity. The maximal output current is 20 µA. For each channel an individual current limit can be set, which after being crossed shuts down the output voltage. The voltage can be adjusted in step of 0.1 V. It has a remote control access using various serial data transmission interfaces.

The HV is connected to the silicon sensors via HV adapter. The sensor is biased with a high potential on cathode, whereas anode is kept at the ground level.

2.3 Front-end electronics and HV adapter board

The front-end electronics is responsible for the conversion of the electric signal]from the sensor into digital form understandable by higher-level stages of digital readout electronics and computers. Since the electric signals from the sensor are usually very small (the typical signal from $300\,\mu\mathrm{m}$ silicon sensors for minimum ionizing particles is about 25×10^3 electrons), the signal must be first amplified, and in a latter stage shaped.

The experiment requirements and conditions determined the selection of the front end electronics for the pion tracker. The first detection station is exposed to secondary beam rates of order of 10^6 to 10^7 particles per second. The trigger decision is received with a delay of the order of $800\,\mathrm{ns}$ with respect to the hit detection in the pion tracker station. There is a certain probability of pile up for the beam particles and good solution for such a problem is a front end electronics architecture with a free running system. This works independently from the main detector acquisition system (DAQ) and allows for tagging single particle events with time stamp, later used for correlating recorded hits with events in HADES. To properly match the multiple hits registered on both sides of single double sided silicon sensor, the measurement of the energy deposition is the most important factor. The time resolution of signals from the silicon detector on level of several ns is not sufficient for the hit reconstruction and fake coincidences rejection.

This functionality is integrated in the single n-XYTER ASIC chip, which is described in Section 1.3.2. Together with additional infrastructures (ADC converters, power supplies and filters, logical communication) it is assembled on a single electronic module called *n-XYTER Front-End Board*.

The readout modules for the n-XYTER – FEB (Front-End Board) rev D is shown on Fig. 2.5. It is a development module designed for the future STS (Silicon Tracking System) for the CBM experiment. It contains all required parts to fully operate the n-XYTER, including the ADC to digitize the analogue signals from the n-XYTER.

The FEB module has a built in power stabilizer for $3.3\,\mathrm{V}$ (n-XYTER) and $1.8\,\mathrm{V}$ (ADC) and requires an external voltage of $5\,\mathrm{V}$. Since the FEB stabilizers are low voltage drop (LDO) devices which require around $0.5\,\mathrm{V}$ of voltage difference between input and output, it was possible to run the module at $4\,\mathrm{V}$ supply. By taking into account the voltage drop on the supply cables, it was found that $4.3\,\mathrm{V}$ of the supply voltage in the external power regulator is sufficient to run the device. The current consumption of the FEB board is around $1.5\,\mathrm{A}$. Reducing supply voltage to $4.3\,\mathrm{V}$ allows to reduce the heating of the module by roughly $1\,\mathrm{W}$, which otherwise must be dissipated by the power stabilizer as heat. Part of the heat will go through the PCB to the n-XYTER chip, other part through the wired connection and this would heat up the silicon sensor sitting in the vacuum. Since the n-XYTER chip must dissipate roughly $3\,\mathrm{W}$ of power, its working temperature rises to $20\,^{\circ}\mathrm{C}$ above the room temperatures. A cooling block attached to the FEB on the bottom side helps to remove generated heat. Additionally, drilled canals inside the cooling block allow to attach a fluid cooling and stabilize temperature.

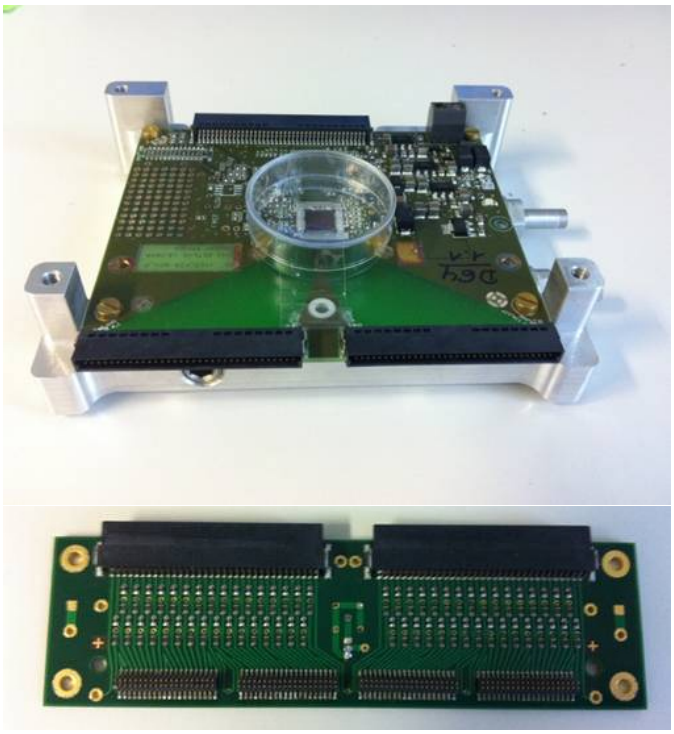

Figure 2.5: The n-XYTER readout module (FEB) together with aluminum water cooling block (upper figure) and the high voltage and decoupling adapter (lower figure).

The n-XYTER gives an access to voltages at several points in the analogue part of the signal processing. Two most important points, VbiasS and VbiasF1, are buffered and connected to the separated monitoring ADC[3] converter, accessible by the I2C interface. The ADC has four inputs and beside the two registers gives access to the temperature sensor located close to the n-XYTER, and to the supply current monitor.

Since the n-XYTER FEB itself is designed as a general purpose module, it does not provide any biasing system required for DC-coupled silicon sensors. For a sensors used in the pion tracker Design, appropriate adapters were designed for biasing the sensors with a high voltage and decoupling it from the ASIC inputs.

Figure 2.5 shows picture of the HV adapter module that is used for detector biasing and signal decoupling. One adapter is used for one side of the detector. The adapter is mounted outside the chamber, between the Detector PCB and the FEB module.

The adapter as well as the FEB modules should be shielded against environmental noise. This is achieved with the help of a copper box placed around the electronics.

The author of this work, during his work in the GSI Detector Lab in years 2007-2008, was involved in the development of the first FEB modules. He designed the first three

[3]The other ADC converter than used to sample the n-XYTER output.

front-end electronics (fee) modules used in the CBM-STS, CBM-MUCH and CBM-RICH test experiments in years 2008-2009. Results of his work are presented in his master thesis [Lal09]. The FEB modules used later for the development of the HADES beam detector, as well for FOPI beam monitor and various CBM detector subsystems are further evaluations of the first prototype versions.

2.4 TRB3 readout and DAQ integration

The front-end electronics is integrated in the data acquisition system by the TRB3 modules (blue blocks in Fig. 2.6). The TRB3 [Trb] is an universal board of general purpose based on a programable FPGA ASICs. A custom readout logic cooperating with lower-level FEE can be implement in each of four FPGA modules (black chips in the corners of the TRB3 modules as seen on Fig. 2.7, left), connected to the outer world by 128 digital I/O lines. The central FPGA plays role of bridge between all FPGAs and provides communication to higher-level logic of the DAQ system.

In this project, the role of the TRB3 is to buffer data send out continuously by the n-XYTER modules, group and sort according to the event time-stamp. Upon the trigger request from the DAQ, TRB3 scans all buffered events, and selects only those which time-stamps fits to preset time window selection. All earlier events are then discarded, all later events wait until next trigger comes. There is defined preset time, after which it

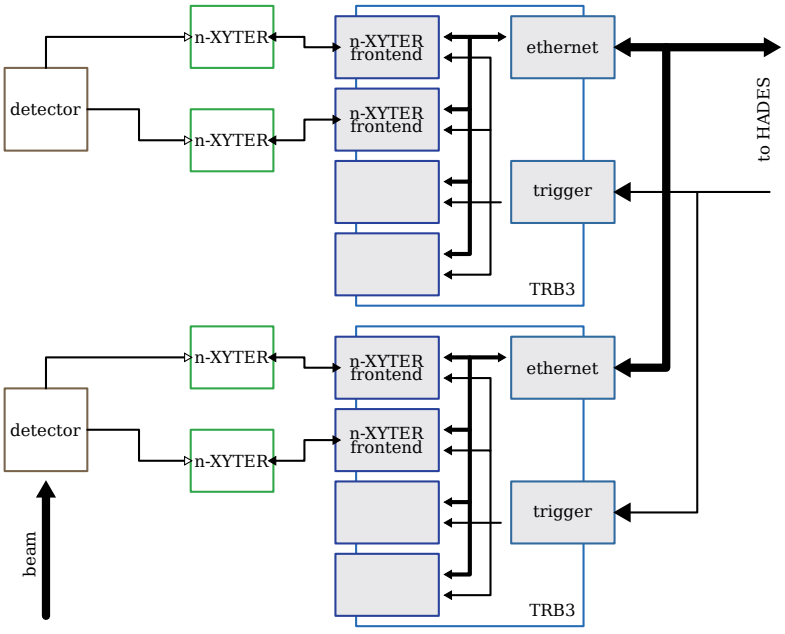

Figure 2.6: Architecture of the pion tracker readout system.

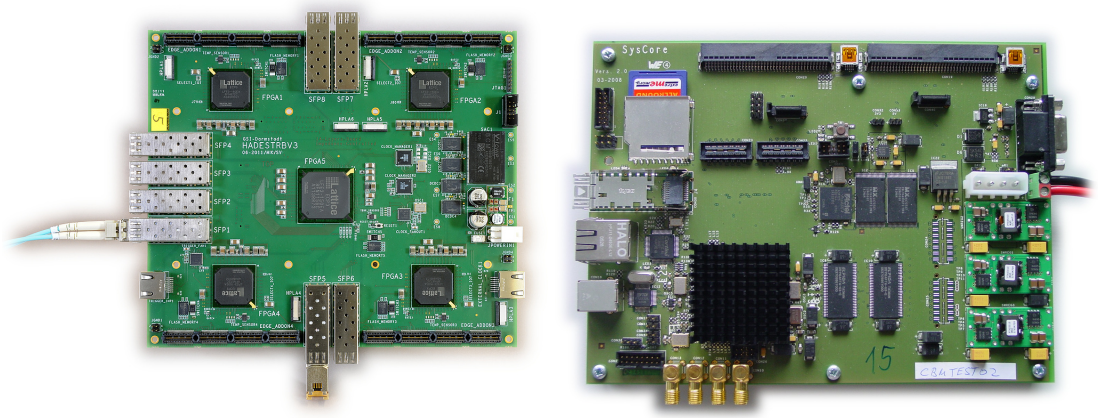

Figure 2.7: Picture of the TRB3 (left) and the SysCore (right) readout modules.

is assumed that events can be safely discarded, and therefore TRB3 removes older events from the buffer continuously.

The whole TRB3 and n-XYTER system is designed to work in stand-alone mode, with minimal amount of necessary input, which in this case is a trigger request signal provided by the Central trigger System (CTS) of HADES. Communication and configuration is realized over HADES TrbNet protocol, common for all detector systems in the HADES DAQ network.

2.4.1 SysCore readout

In the early stages of the development, n-XYTER readout was running with the SysCore [Sysb; Sysa] readout module (Fig. 2.7, right). SysCore utilizes one FPGA module, and can operate with two FEBs. It is a native readout module designed exclusively for the n-XYTER and designed to operate in the CbmNet network of the CBM experiment. This readout is then not compatible with the HADES TrbNet, but was sufficient to run all laboratory and first beam tests with the front-end electronics and silicon sensors.

The aim of the CbmNet is to provide a communication layer in a trigger-less DAQ system, where all detector hits are correlated by a global time stamp and sorted on the fly. The SysCore captures all the raw data from the n-XYTER, encapsulates them with all additional information required by the CbmNet system, and sends further to a upstream systems. The SysCore provides also an external trigger input which on demand, inject a special Trigger data frame into the stream of data. In the upstream system, which during the tests was single PC, the Trigger frame can be decoded and used to correlate events and perform classical, trigger based analysis of the data.

2.5 Mechanical construction

The mechanical components are crucial parts of the tracking station design. Both detector stations must be mounted in the part belonging to the accelerator infrastructure. The vacuum chamber must assure high vacuum on the level of $1.5 \times 10^{-7}\,\mathrm{mbar}$. The number of inlets to the chamber has to be on a minimal level to reduce the risks of vacuum leaks. An unsealing of the beam line would lead to an accelerator shutdown conencted with performing of many measures, like full inspection of the beam line for any obstacles inside the beam pipes before the pressure in the whole accelerator facility is re-established.

At the same time the chamber has to allow for routing out of 256 silicon channels to the electronics located outside the vacuum. Additionally, the sensor cooling requires that

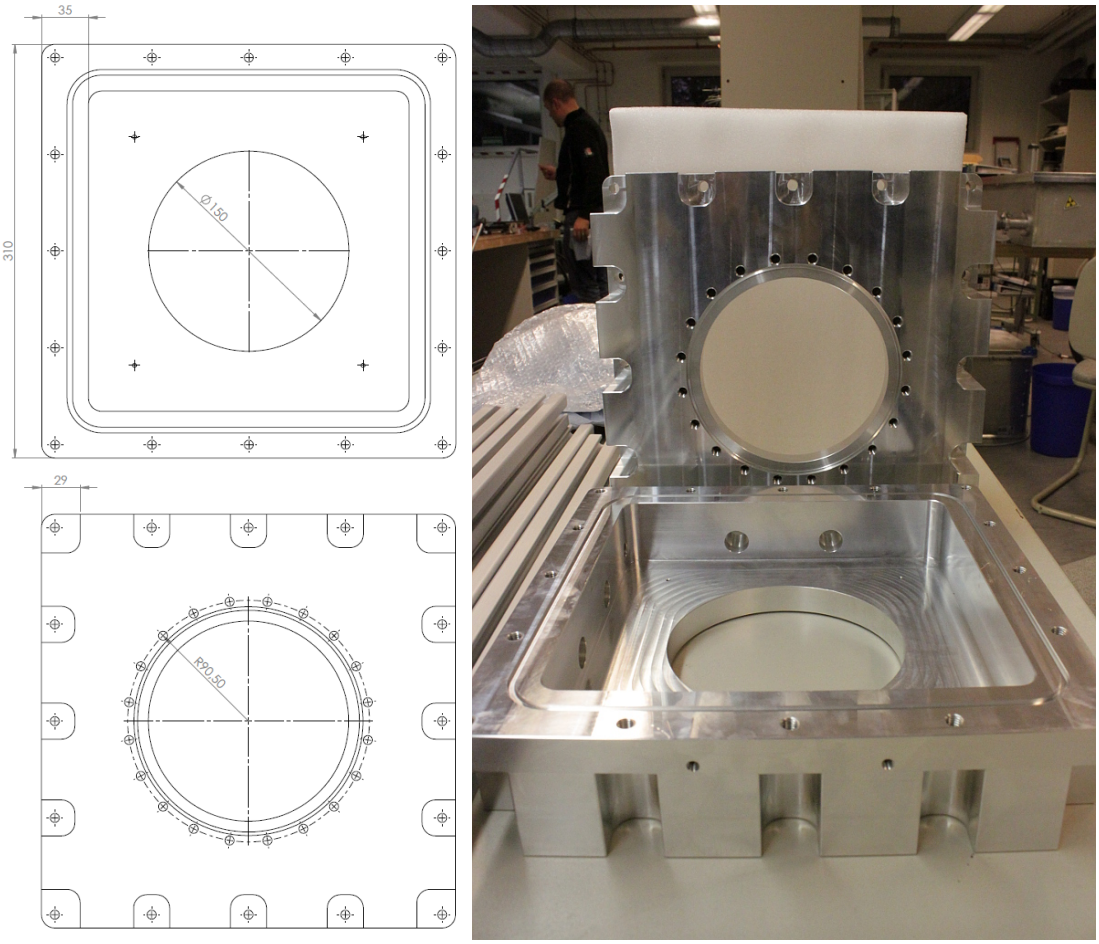

(a) CAD drawing. **(b)** Two halves of the vacuum chamber.

Figure 2.8: The CAD drawing and the picture of the vacuum chamber halves.

the two pipes transporting the cooling fluid must go out through the chamber walls. Since the cooling parts located inside the chamber have to be detachable, a tight connection preventing leaking of the coolant to the vacuum has to be assured.

2.5.1 Vacuum chambers

Figure 2.8 presents the bare elements of one vacuum chamber. Each chamber is built of two symmetric, rectangular, aluminium halves. On the one side of each halve, there is a rectangular frame with threads used to screw the two frames together. The other side is flat and contains a circular cut-off with the mounting structure, which is compatible with the CF160 standard and allows to attach the chamber directly to the beam pipe. Both halves of the chamber are separated by a single PCB board, which provides the routing of the silicon sensors channel to the outer world.

The route-through board is a four layers PCB. The signal wires are routed in the two inner layers (Fig. 2.9a). The top and bottom surfaces are covered by a gold layer using immersion gold technology, providing very flat surfaces of the PCB to assure the vacuum tightness of the chamber. The signal wires are wired out on two sides of the PCB, the location connectors are seen on the left and on the top in the figure. The right side connection provides 16 pairs of differential lines, allowing to add additional devices inside the chamber, e.g. temperature sensors. These sensors were not used in the final design.

On the inner edge of the PCB, there is set of Samtec TSM pin headers, compatible with those on the silicon sensor PCB, which allow for one-to-one connection between

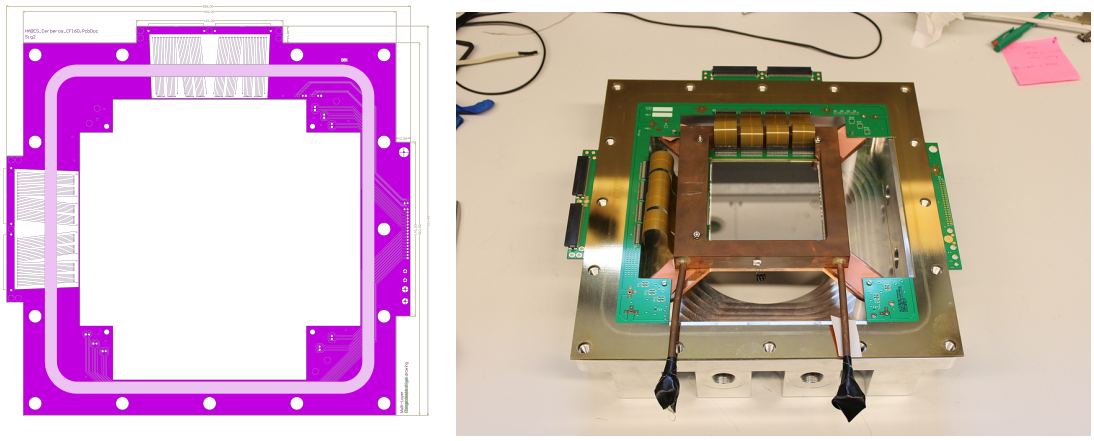

(a) Design of single inner layer. **(b)** PCB as an element of sandwich stack.

Figure 2.9: Picture of the PCB placed in its dedicated place on the chamber halve and CAD drawing of single inner PCB layer.

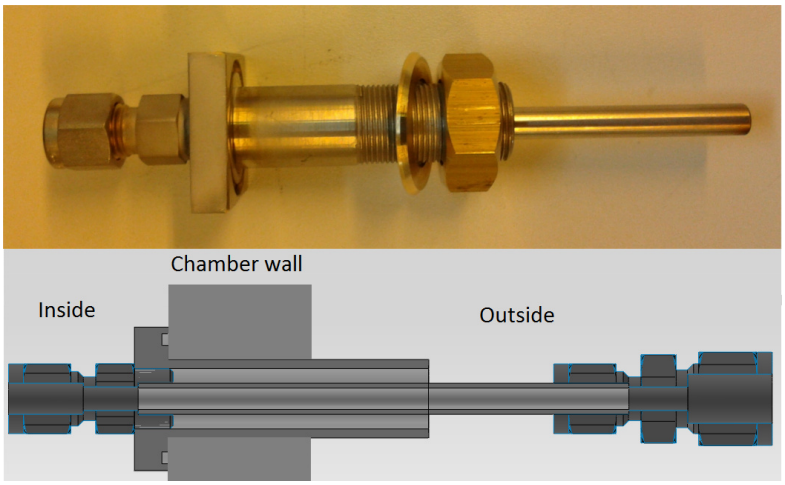

Figure 2.10: Metal feed-trough sockets for the cooling transportation and drawing of the mounting to the chamber wall.

parts using kapton tapes, as shown in Fig. 2.9b. The big copper structure in the middle of the chamber is a cooling block of the first cooling prototype. The reflective layer seen inside the cooling block is the silicon sensor.

The tightness between the PCB and the aluminium halves is realized with rubber o-rings. Each halve has a groove keeping the o-ring inside. When under pressure by screwing the halves together, the o-ring is compressed and fills whole volume of the groove. The tightness depends then on the roughness of the PCB surface and the groove of the halves. The chamber has been manufactured in the TUM Physics Department Workshop. During the assembling of the stations, a small amount of vaseline was used to glue o-rings in the groove and avoid falling of it during mounting process.

The coolant for the detector cooling device circulates in a copper tube through the wall of a single halve. Therefore one of the halves has two additional drills in the wall. This halve is always the base of the chamber, all components like the sensor, the cooling device and the route-through PCB are always aligned to it, the other halve is mounted on top of the base.

The coolant is transported through custom sockets (feed-through), designed and built in the way that the shrinking of the material will not result in tightness losses. The picture and the CAD drawing of the design is shown in Fig. 2.10. The left side of the design is located inside the chamber and the pipe on the right side is connected to the cooling device. The vacuum tightness is achieved with an o-ring palced in the groove of the flat squared element, and a nut attached from the outer side of the chamber.

At the end of the feed-through coolant pipe Swagelog fittings were welded. Those are special sockets allowing for a tight removable connections suitable for vacuum applications.

2.5.2 Detector cooling

The cooling system for the silicon sensor was designed to reduce the temperature of the sensor to $-5\,^{\circ}\mathrm{C}$. Keeping the sensor at low temperature allows to reduce the leakage current of the sensor, and therefore the intrinsic noise. Moreover, a lower temperature decreases the radiation damage effects occurring in the silicon lattice during irradiation with beam particles. This is crucial for the first of the detection stations, that is located close to the pion production target, and thus has to cope with high neutrons flux.

The main heat sources are due to environment radiation from the beam pipes, and through copper wires on the kapton tapes.

Figure 2.11 presents the concept of the cooling device. The PCB with the silicon sensor is attached to a copper block with drilled tunnels inside for fluid transportation. The coolant is transported from the feed-through to the copper body via especially manufactured tubes. The copper block is in thermal contact with the PCB of the sensor. To guarantee good heat transfer connection, a thermal pad is placed in between. In sucha way the sensor gets cooled indirectly by the cooling body. To shield the sensor from heat radiation the latter is surrounded by a so called *fridge*. On the surfaces crossed by the beam, the fridge employes two very thin Mylar foils introducing a negligible material budget. Sides of the fridge, playing also role of support for the Mylar foils, are made of aluminium. The cooling system mounted on the chamber is shown in Fig. 2.12 at left.

Cooling is controlled by Huber Mini Chiller device. It allows to cool down the coolant to the temperature of $-20\,^{\circ}\mathrm{C}$. To avoid mechanical stress in the sensor and ine the sensor's PCB, the cooling procedure was working in a stepped mode, where every $3\,\mathrm{min}$ the target temperature of the chiller was reduced by $0.5\,^{\circ}\mathrm{C}$. Therefore the full cooling cycle at room temperature takes around $3\,\mathrm{h}$.

The coolant used in the system is a mixture of polypropylen-glicol and water, with

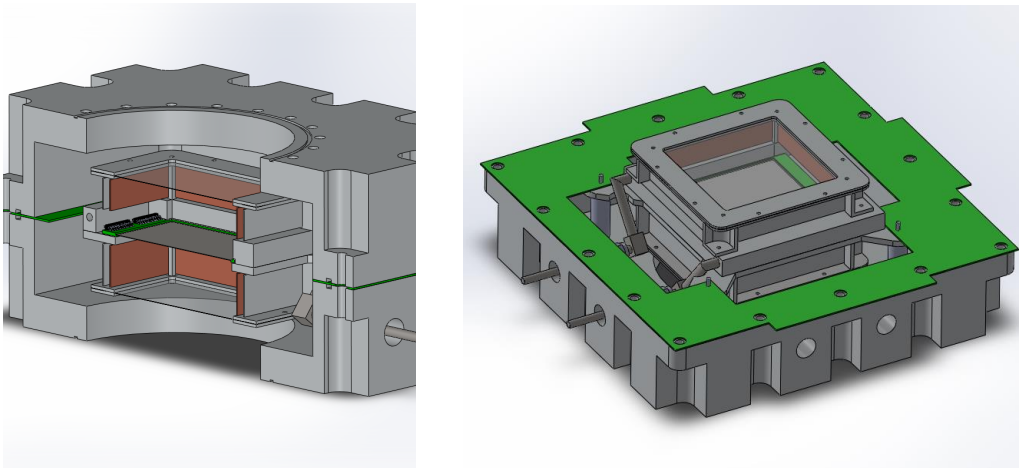

Figure 2.11: Technical drawing of the cooling system inside the chamber.

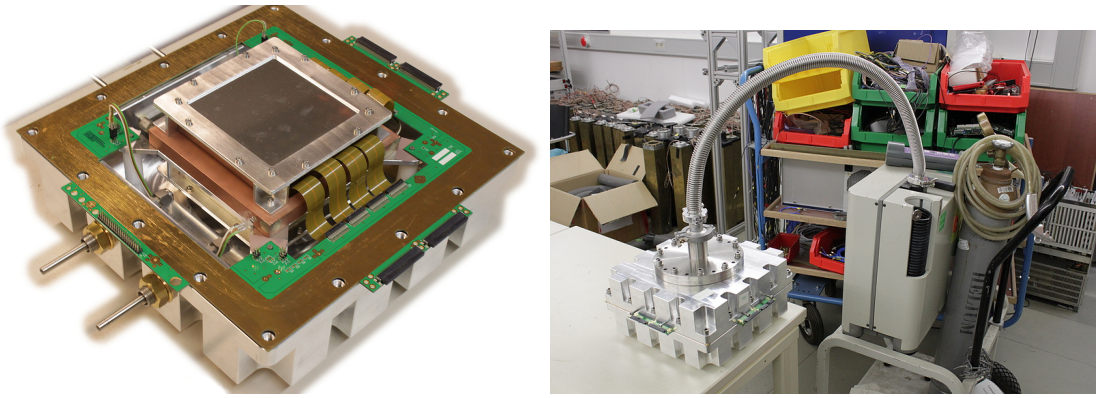

Figure 2.12: Left: View of the chamber with mounted and connected cooling system. Right: Chamber during leak tests.

proportions of 2:3. Polypropylen-glicol reduces the freezing point of the coolant to $-20\,^{\circ}\mathrm{C}$ whereas the water is responsible for the heat transfer.

A measurement of the leakage current shown that at coolant temperatures of $-20\,^{\circ}\mathrm{C}$, the leakage current was reduced by roughly a factor four. The leakage current change during the cooling cycle is shown if Fig. 2.13. The temperature of the sensor was measured before with the help of a mechanical sample – the silicon sensor which did not pass QA checks in the manufacturing process and was used for some tests as dummy in place of the real sensor. The dummy sensor reached a value of $-5\,^{\circ}\mathrm{C}$.

Detailed description of the cooling feasibility and heat transport to and from the silicon sensors studies can be found in [Lou13]. The development and testing of the cooling system and of the mechanical components can be found in [Wir13].

The detector chamber together with the cooling system was tested for leaks using

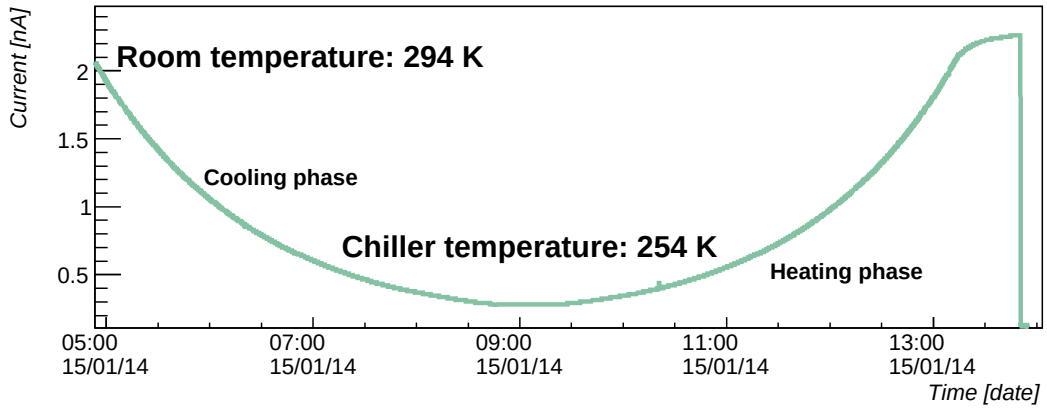

Figure 2.13: Leakage current of the detector during the cooling cycle.

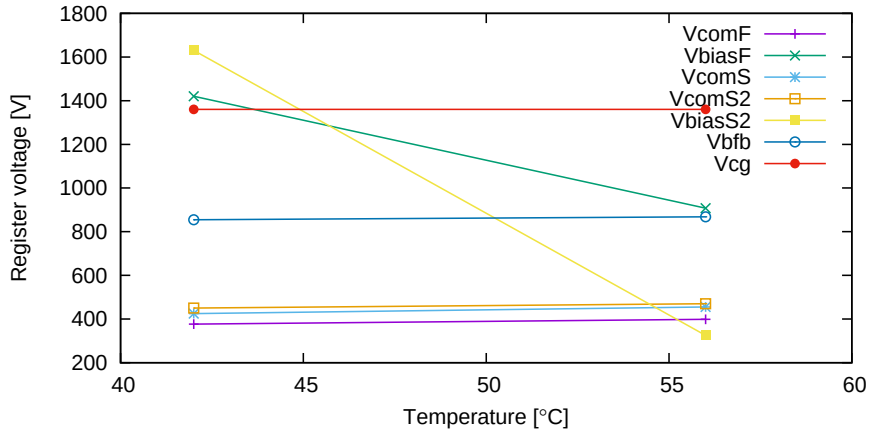

Figure 2.14: Temperature coefficients for different DAC registers.

helium probe Balzers HLT160. The measurements did not reveale any leaks in the system, and no helium was detected with the leak rate probe of $10^{-9}\,\mathrm{mbar\,L\,s^{-1}}$ sensitivity. Figure 2.12 shows the full chamber during leakage rate tests.

2.6 Calibrations

To preapre the pion tracker detector for operation and data taking, the following steps had to be undertaken: *(i)* calibration of the working point (DAC registers) of the n-XYTER, *(ii)* calibration of the analogue output base line, *(iii)* configuration of the dead time, *(iv)* calibration of the energy spectrum.

Since all the data processing stages are integrated inside a single chip in the n-XYTER, the chip requires a minimum amount of preparation. The default values in most cases guarantee an optimal operation. Depending on the chosen input polarity, only an adjustment of the base line levels of the shaper outputs is required. To be able to properly interpret the analog output, base line calibration is required.

2.6.1 Bias DAC registers calibration

All the DAC registers were designed to have the same positive temperature coefficients. It guarantees that temperature variation will not have influence on the working point of the chip. Unfortunately at this stage of the n-XYTER design, registers 20 to 22 were by mistake designed in a different way, register VbiasF and VbiaS2 have both negative temperature coefficient of different slopes [Sol08], and it has a major impact on the signal discriminating. The measurement of the coefficients is shown in Fig. 2.14.

The register VbiasF controls the voltage level on one of the discriminator inputs.

The second input is controlled by the register Vth having an absolute voltage level independent from the VbiasF settings. If the temperature varies significantly, the voltage difference between both inputs changes, what leads to a change of relative (between both discriminator inputs) discrimination level. A variation of the temperature on the slow shaper output will change the reference values of the analogue output leading to a systematic error in the amplitude determination. Since the second stage of the slow shaper in the positive input polarity configuration inverts the signal, the variation of the analogue output changes in the opposite directions for the different polarities. This issue must be resolved by the user, by either applying an efficient cooling or applying a proper calibration method to the data.

Using an additional monitoring ADC implemented on the FEB, one can measure the characteristics of the biasing registers. The results are shown in Fig. 2.15a. The calibration of the monitoring ADC is shown in Fig. 2.15b. Figure 2.16 shows the results of the bias registers measurement within two days of the beam taking. Two upper plots show the fast and the slow shaper outputs base line, plot in the bottom shows the temperature variation. NE5 and HAD denote both locations of the tracking stations, the NE5 area and the HADES cave respectively. Glitches observed in some of the plots are related to bit flips in the data transmission. The temperature was measured by TMP37 [Dev] sensors assembled close to the n-XYTER chip on the FEB board. A measured temperature of roughly $40\,^{\circ}\mathrm{C}$ results from the heating up of the chip during the operation. Whereas in the HADES cave the temperature was kept constant via air conditioning, the NE5 area is sensitive to the day-night variations. The local temperature variations were however low enough to keep all registers of the n-XYTER at proper biasing levels and no further cooling was required.

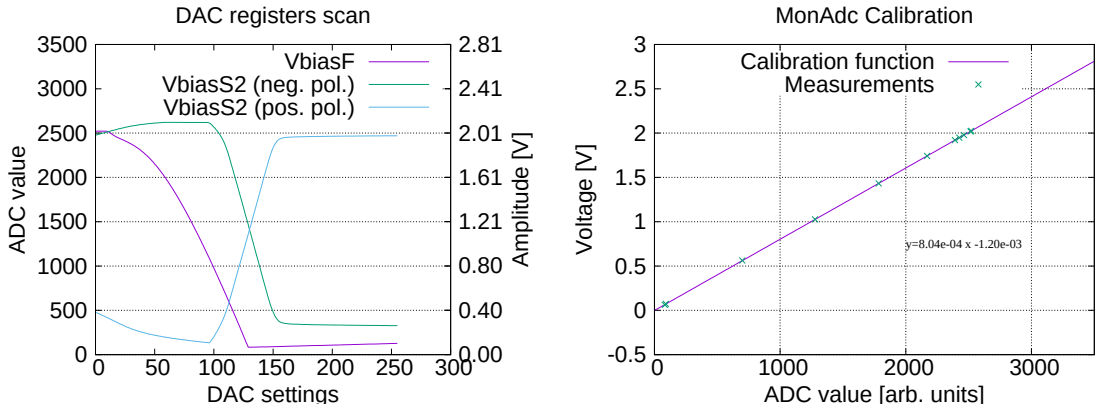

(a) DAC registers scan.

(b) Monitoring ADC calibration.

Figure 2.15: Characteristics of the VbiasF register, and VbiasS2 registers for both polarities and calibration of the monitoring ADC.

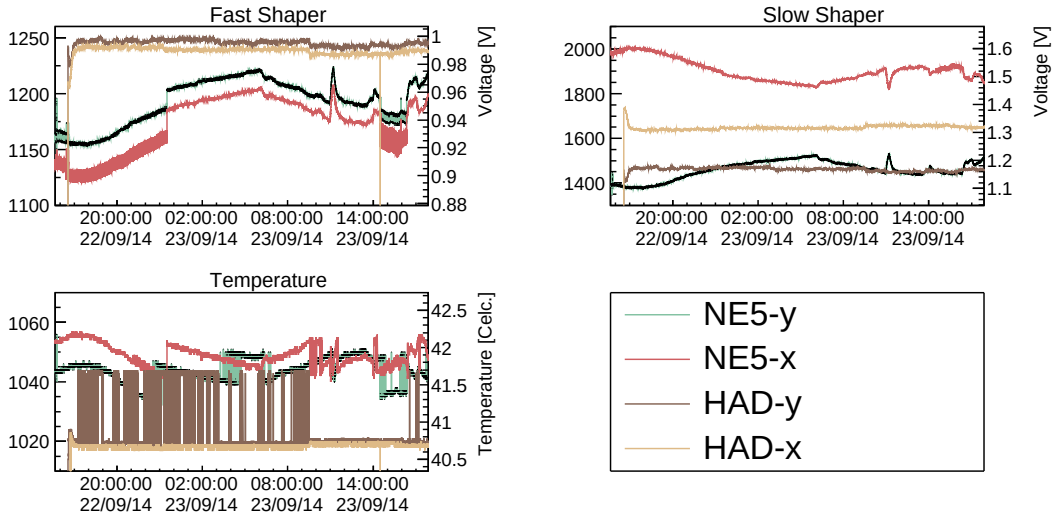

Figure 2.16: Variation of the registers settings under temperature change.

2.6.2 Base line calibration

The analogue output of the n-XYTER gives an energy value as a differential signal, where the amplitude is equal to voltages difference between both output lines. Such differential transmission assures higher tolerance for the external noise. The common level is set on approximately 1.1 V. The output signal is negative with respect to the common level. Additionally, every single channel has also a different reference level, which is seen as a default voltage difference in output in case of a zero signal input, for example in test trigger mode. This is visible in test data as shown in Fig. 2.17. The upper line shows the pedestals whereas the lower line corresponds to a pulser signal of 4 fC. The difference in noise width in both panels comes from the difference of the noise performance for opposite polarity settings.

The analogue output of the n-XYTER chip needs to be calibrated in order to obtain

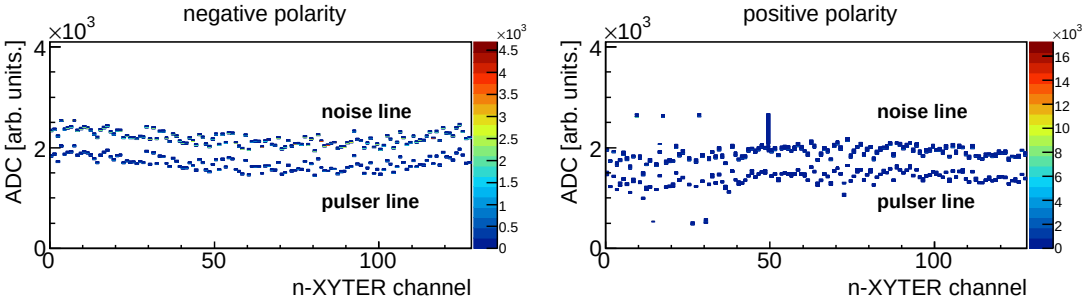

Figure 2.17: Pedestals distributions measured with pulser in test trigger mode.

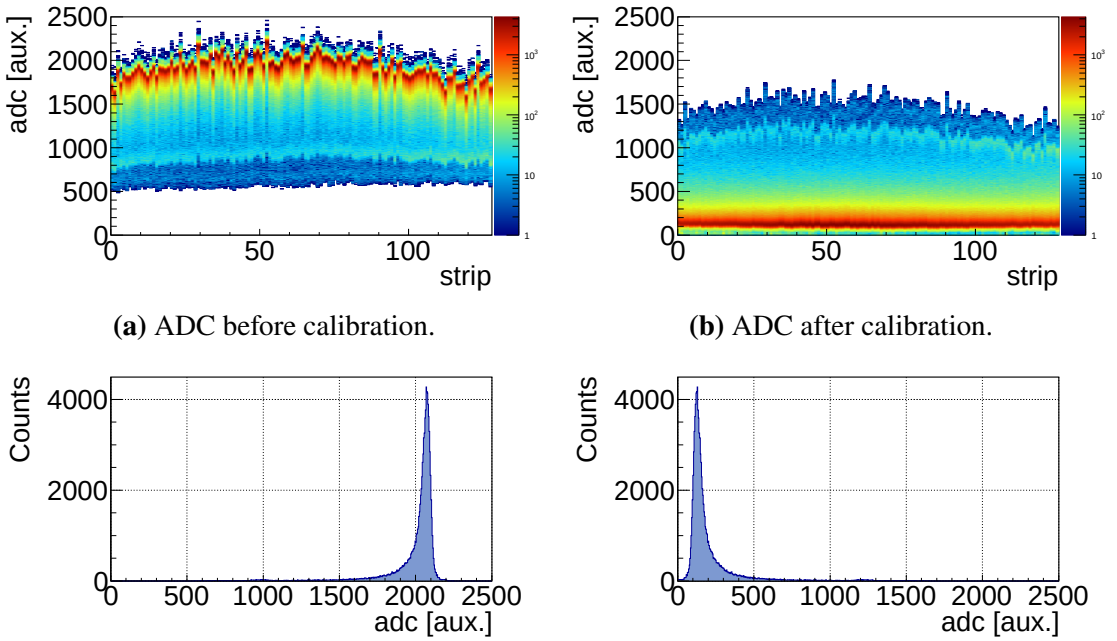

(a) ADC before calibration.

(b) ADC after calibration.

(c) Single channel before calibration.

(d) Single channel after calibration.

Figure 2.18: Result of base line calibration for single n-XYTER chip. In the upper row X-axis represents detector channel, y-axis is the ADC value in arbitrary units. Lower row shows ADC distribution for single channel.

reasonable and comparable values in all channels. The calibration requires the measured output voltage must be inverted and corrected by the offset, that must be individually determined for each channel.

It is also shown in Figs. 2.18a and 2.18c, presenting data from the $\pi + X$ beam run at HADES. In the left upper panel, figure shows distributions of energies deposited in the silicon by pions over all the n-XYTER channels. In the lower left panel the uncalibrated ADC distribution of a single channel.

There are two basic methods to calibrate the ADC signal. In the first method, the base line levels are measured as shown in Fig. 2.17 (but without pulser signals). For this purpose, the n-XYTER must be switched into the Test Trigger mode, and a certain number of random pulses are sent to the internal trigger generator. The signal measured on the output will deliver Gaussian like distribution, which after fitting will provide the mean value μ_{bl} of the base pedestal line for given channel. In the next step, each ADC value y_{raw} must be calibrated using following transformation:

$$y_{\mathrm{cal}} = -(y_{\mathrm{raw}} - \mu_{\mathrm{bl}}). \tag{2.1}$$

The disadvantage of this method is that the base line must be remeasured each time, when the temperature of the chip changes. This method is then unpractical under continuous

beam conditions, since a switch to Test Trigger requires a reconfiguration of the chip.

In the second method, base line is measured only once as a the reference. This measurement should be done before beam run to assure equal temperature conditions. The calibration parameters are calculated like before, and this calibration is called reference calibration. For each new captured data file[4] the calibration is done using the default reference base line. In the next step, maximum of the charge distribution is compared with the reference file and difference is stored in database as a additional offset. Then each file must be recalibrated, using the reference base line calibration together with an additional offset to correct for the temperature offsets. This method was used in the pion beam run. In each of the pion beam campaign, a new reference calibration was measured before restarting of the beam, and the new calibration was used for next files.

2.6.3 Threshold calibration

Free running readout systems, like n-XYTER based FEB, is sensitive for each kind of signals appearing on the input.To distinct between useful signals generated by e.g. MIPs from the noise, a threshold has to be introduced. Following procedure was used to define threshold values and measure threshold trim corrections for the each individual channel. Each channel has additional Trim DAC register which adds small offset to the threshold value.

The n-XYTER was run in Test Pulse mode, which allows to inject small charge amount using the build-in capacitors and pulse generators. The amplitude of the generator was adjusted to emulate the average MIP signal in the silicon sensor. It corresponds to a threshold value of 100 in the Fig. 2.19a. The trim registers were set to 0 for all the channels and for each threshold settings, a series of 1000 pulses were sent to trigger the internal pulser. Figure 2.19a represent the s-curve of each channel before and after calibration, respectively. The s-curve is obtained by varying the threshold in very small steps and recording the corresponding hit rate. For very low threshold values, the noise events can generate a signal and this case corresponds in Fig. 2.19a to the red band with intensity of 10^5 counts. If the threshold is set above the noise level, the number of registered counts drops down to 10^3 counts (broad yellow band). When the threshold level reaches the signal amplitude, the number of counts is gradually decreased until 0. The working threshold value was defined as a position of the half yield on the s-curve, in this case the value of threshold with count yield closests to 500.

To obtain the characteristics of the Trim DAC registers, this measurement was repeated three times for three different settings of the trim register: lowest (0), middle (15), and highest (31). For each channel, a linear regression correlating the measured threshold level and the trim register value was performed, and the appropriate coefficients were calculated (Fig. 2.19b). Since the trim registers moves up the threshold value, the high-

[4] In HADES during the pion beam new file was recorded in periods of a few minutes

est measured value was taken as a reference and for all the other channels an appropriate trim correction equalizing all s-curves was calculated using the difference in the threshold value and the calculated coefficient. The results are presented in the lower graph of Fig. 2.19a.

Afterwards it was observed that the spread of the thresholds is much lower than the

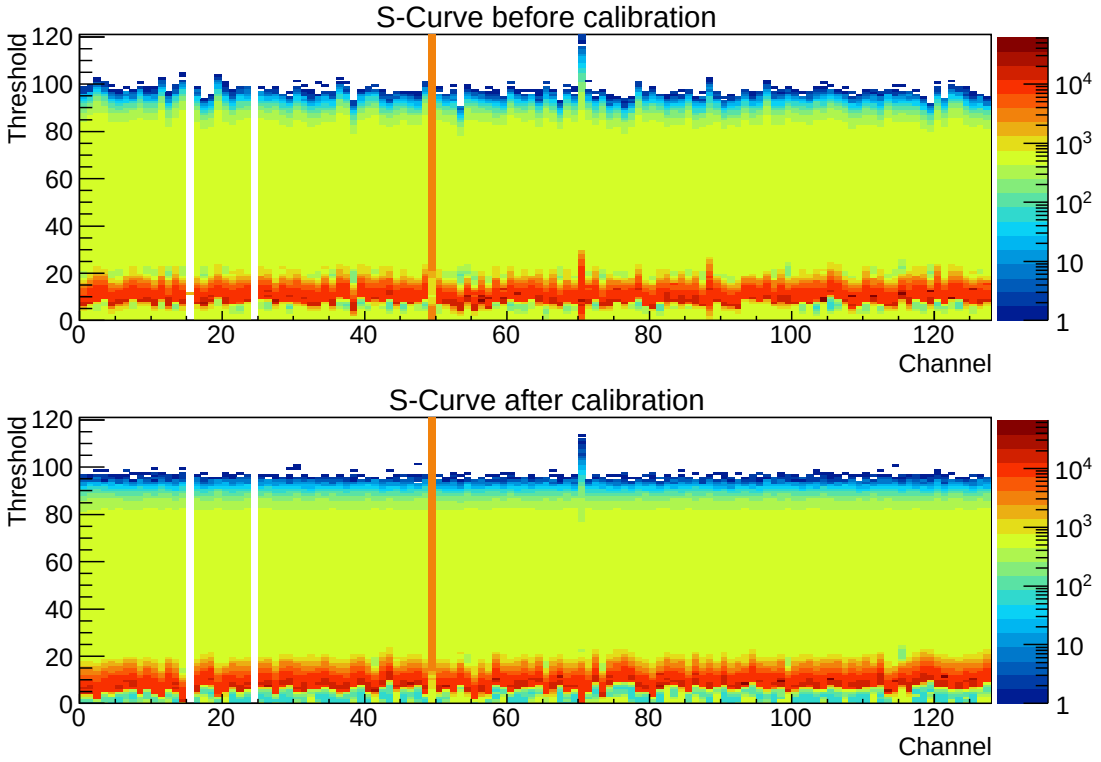

(a)

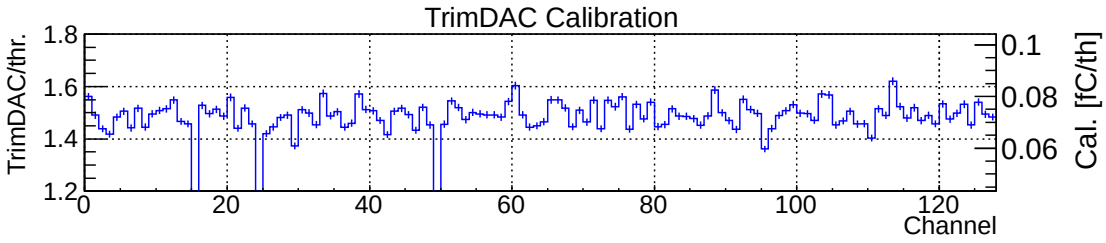

(b)

Figure 2.19: (a) The s-curve characteristics of the n-XYTER channels before and after the calibration. Two white and the orange bands are broken channels. Broader transition of the s-curve on the channel 70 is related to additional capacitance load in its input. (b) Calibration coefficients of the different Trim DAC registers.

effective separation between the MIP signal and the noise level. Since loading the trim correction to the n-XYTER in the first version of the prototype with the SysCore reasout was causing problems and frequently lead to a freezing of the system, the calibration procedure was decided as a optional and never used in future tests and measurements.

Aside the three broken channels visible in figure, channel no. 70 shown in the figure was additionaly connected to a single silicon PIN diode, and therefore additional input capacitance changed the s-curve spectrum of this channel.

2.6.4 Dead Time parametrization

In order to cope with high beam rates, as expected during the experiment in the first tracking station, one has to set proper dead time for single analogue channels. A shorter dead time increases the risk of pile up events, thus a decision must be made as a compromise between maximizing the rate and minimizing the pile-up probability. The dead time is controlled by a single register iDur, common for all the channels.

The calibration procedure is the following: the n-XYTER is set in the test trigger mode, and a set of two consecutive pulses is sent to the internal pulse generator. The time separation between the pulses is then varying starting from the smaller periods and increased in every step. Initial value can be any, but in principle the fast shaper peaking time of $100\,\mathrm{ns}$ sets a reasonable lower limit to the pulse time separation. Series of such double pulses is sent to the trigger input of the n-XYTER. On the output, the number of events containing the pile-up flag are counted, leading to creation of s-curve distribution. For time periods shorter than the dead time, the number of pile-up counts should be $100\,\%$, for longer periods it drops to 0. The series is ended after the count rate of 10 consecutive measurements is equal to 0. The transition point of the s-curve determines the dead time. Measurement is repeated for various settings of the iDur register.

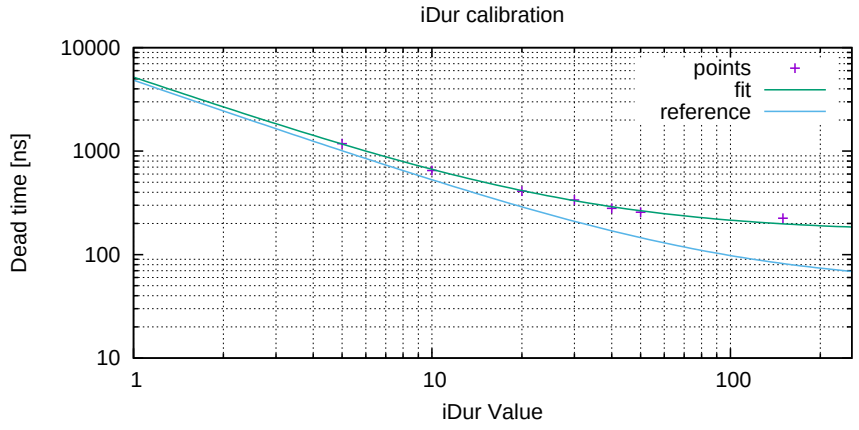

Figure 2.20: Calibration of the iDur register. Blue line is from [Bro+06].

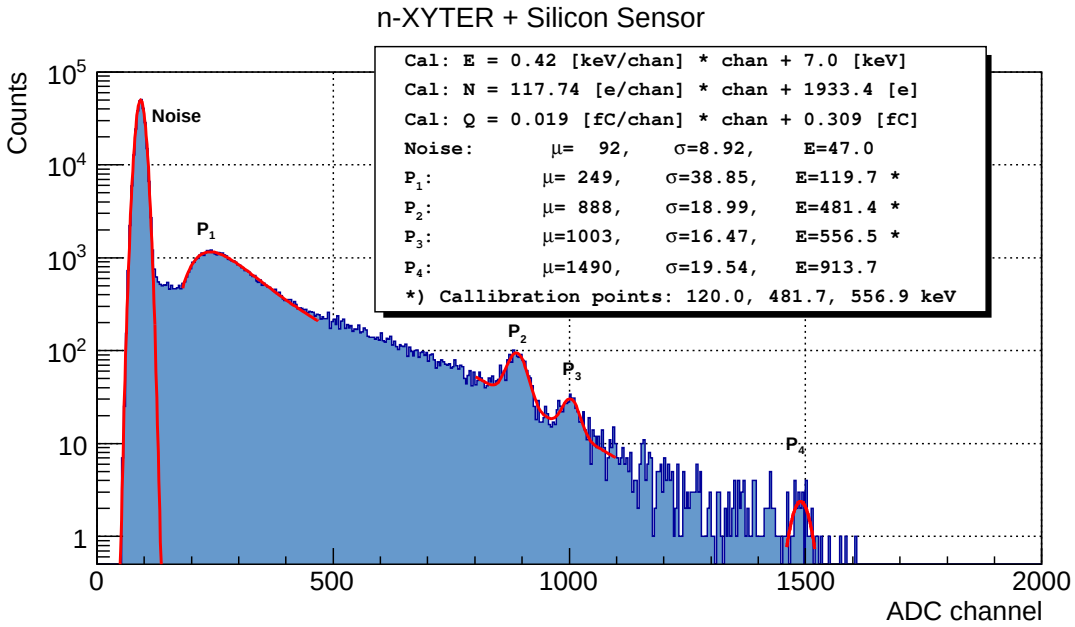

Figure 2.21: Calibration of the n-XYTER with silicon sensor and ^{207}Bi radioactive source.

The final calibration is presented in Fig. 2.20. The results of the fit are

$$T_d = (5023.01 \pm 98.91) \cdot r^{-1} + (164.856 \pm 8.742),$$

where T_d is the dead time in ns for given iDur register value r. From the [Bro+06] the reference parametrization is

$$T_d = 4790 \cdot r^{-1} + 50,$$

and was measured by direct accessing of the monostable output of the n-XYTER. Such access is not possible with the available Front-End modules.

During the experiments with pion beams the dead time was set to $480\,\mathrm{ns}$, allowing for measurement of maximal $2 \times 10^6\,\mathrm{counts/s}$ on a single input channel.

2.6.5 Energy calibration of n-XYTER

Figure 2.21 presents the results of the sensor calibration determined with a ^{207}Bi radioactive source. The silicon sensor was attached to the n-XYTER operated in normal operation mode. The radioactive source was placed on one side of the sensor at a distance of $3\,\mathrm{cm}$ from its surface. The threshold level was set low enough to capture partially noise spectrum but to do not be dominated by it. Noise peak is identified and marked on the figure.

The peak identified as a P_1 comes from energy deposition of MIP electrons flying through the sensor, and the energy associated with this peak is equivalent to $120\,\mathrm{keV}$. This peak sits on top of the linear (in a logarytmic scale) background spectrum resulting from a sub-MIP electrons. A similar structure is seen in measurements with a $300\,\mu\mathrm{m}$ thick silicon photodiodes by Böttcher in [Böt11].

The peaks P_2 and P_3 are associated with monochromatic conversion electrons emitted by the ^{207}Bi source with energies of $482\,\mathrm{keV}$ and $556\,\mathrm{keV}$. Third monochromatic line of $976\,\mathrm{keV}$ was firstly associated to P_4, but later on P_4 was identified as a saturation value of the pre-amplifier. However the energy of the third line exceeds $6\,\mathrm{MIPS}$ linear range it is possible to register higher energies in non-linear range as a saturation peak. For the same reason fourth monoenergetic line of $1049\,\mathrm{keV}$ also cannot be observed.

Finally, only points P_1 to P_3 were used to calibrate the n-XYTER. The results of energy calibration E, number of electrons N and of total charge Q are the following:

$$\begin{aligned} E\,[\mathrm{keV}] &= 1.24\times10^{-4}x^2 + 4.24\times10^{-1}x + 6.96, \\ N\,[\mathrm{el}] &= 3.45\times10^{-2}x^2 + 1.18\times10^{-2}x + 1933, \\ Q\,[\mathrm{fC}] &= 5.54\times10^{-6}x^2 + 18.8\times10^{-3}x + 0.31, \end{aligned} \tag{2.2}$$

where x is the ADC channel number. These values are consistent with the precise measurements performed by GSI DetLab group in [Sor+13].

From the obtained results, signal to nosie ratio defined as a ratio of the signal mean value and the width of the noise is 13.4.

The measurements of the n-XYTER calibration are complementary to the sensors resolution measurements in Section 2.1.1.

2.7 Tests with accelerated beams

Beam tests are crucial to verify the performance of the system, expecially to test the detector response to high rate triggered MIP beams.

2.7.1 Test at SIS18 with secondary particles

First tests employing beams and the full front-end detector readout beam were performed at SIS18 at GSI with a deuteron beam of $1.9\,\mathrm{GeV/u}$ on Al target. The tests were performed inside Cave B. Beam particles were collided on the nuclear target located inside the FOPI detector at the usual target position. Hence, particles stemming from the beam reaction within the target were only measured. The beam monitoring was provided by the FOPI instrumentation. All tested detectors, beside the pion tracker also various CBM detector prototypes, were located behind the FOPI spectrometer, and except the pion tracker, along the beam line. To avoid eventual direct hits from the beams, the silicon detectors were placed $50\,\mathrm{cm}$ away from the beam line axis and around $10\,\mathrm{m}$ downstream

Table 2.2: Most important properties of the SIS18 tests. From [Sch13].

property	run D	run K
# trigger events	234399	506893
# reconstructed tracks	153488	291401
track efficiency	86.4 %	71.4 %
orientation of scintillator	horizontal	vertical
beam particle	d	d
beam energy	1.9 GeV	1.9 GeV
target	1 mm Al	1 mm Al
beam intensity	377 kHz	2.29 MHz to 9.56 MHz
average trigger intensity	170 Hz	48 Hz to 600 Hz
maximal trigger intensity	410 Hz	600 Hz

the beam. This way, the detectors were recording mainly the signals from particles produced during the beam-target reaction.

Figure Fig. 2.22 shows a sketch an alignment of the experimental set up used for this test. In this part, evaluation of two beam runs with deuteron beams will be presented. Table 2.2 shows summary of the evaluated runs.

Figure 2.23 shows the configuration of the setup during the test. A full readout system with two silicon detectors, four n-XYTERs and two SysCore modules has been employed. The two big brown squares denote the silicon sensors. The two rectangles on both sides are the scintillators, aligned in a telescope configuration. Each sensor side

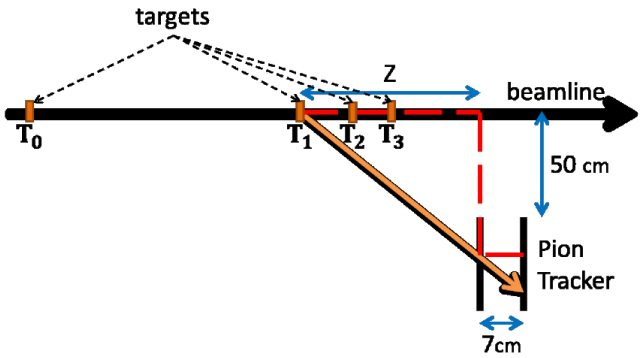

Figure 2.22: Schematic view of the experimental setup of the SIS18 experiment, view from the top. T_0 is the primary beam target, T_1 to T_3 are other detectors in the beam axis, recognized here as scattering centers. pion tracker is located on the side of the beam axis.

is read out by one n-XYTER module plugged to two SysCore modules, each operating a two FEB modules. The scintillators, after amplification and discrimination, are connected to coincidence logic unit. One of the SysCores plays the role of the master device. The data is collected by a single PC station working as DAQ.

In these tests, the silicon sensors were enclosed in aluminum chambers, providing shielding against light, with the whole system running in air. <the experimental goals for this beam time were:

- determination of the tracking capability for two two stations setup under realistic beam condition, by calculating tracking efficiency of each silicon sensor,
- verification of the possibility of triggering on single MIP particles for each n-XYTER,
- evaluation of the detector response at various beam rates,
- analysis of various settings to determine the optimal configuration.

Two scintillators, the first ($2\,\mathrm{cm} \times 6\,\mathrm{cm}$, smaller than the sensor area) in the front and the second ($15\,\mathrm{cm} \times 40\,\mathrm{cm}$, bigger than the sensor area) on the back of the setup provided triggering. As a physical trigger, either the front, the back or coincidence of both scintillators could be used. During these tests, only particle rates between $0.3\,\mathrm{kHz}$ to $1\,\mathrm{kHz}$ were measured. Higher rates could not be registered due to hardware limitations and saturation of the Ethernet bandwidth.

Some attention must be put here to DAQ system based on SysCore modules. In such a configuration, where more than one SysCore modules are working together, they are connected using a master-slaves architecture. One SysCore is working in the superior mode (master). It uses its trigger input to inject special trigger frames into data stream. This trigger frame contains a global time-stamp tag obtained from an internal clock, which is redistributed by fast SYNC connection to all other SysCore modules (slaves). These modules use this time stamp to synchronous their internal clocks and properly tag

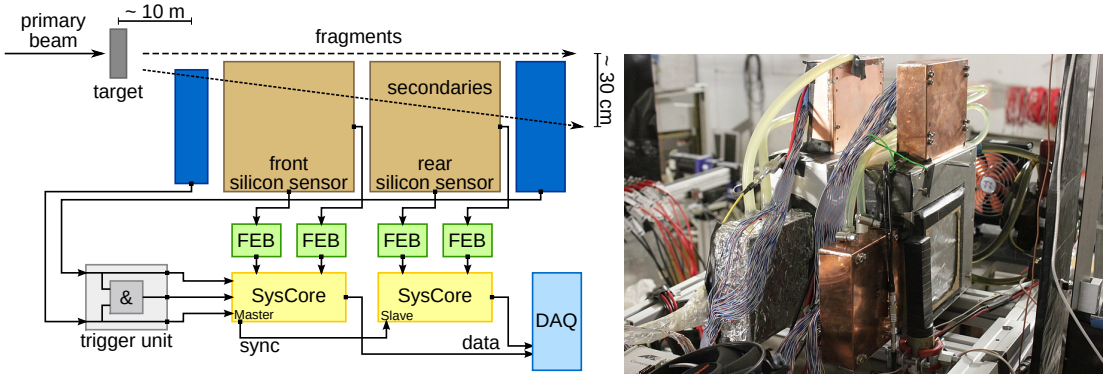

Figure 2.23: Schematic of the DAQ configuration for the beam tests at SIS18 and picture of the experimental setup view from the back. Secondary particles from the sources fly from left to right.

with a time stamp their data. Since the data from all the SysCore modules inherit the same clock reference, it is later possible to correlate data from various SysCore modules together at the software level.

The event selection was based on the time correlation between time-stamps of the trigger signal and the one of the hits. The time difference between both signals is mostly determined by the latency of the SysCore module, since the time of flight of the particle is negligible. The RMS value of this distribution varies within a range of $8\,10$neutron star for different runs. The selection of the events was done within a $200\,\mathrm{ns}$ window asymmetric around correlation peak as shown in Fig. 2.24. The recorded noise level was so low that the lower tail of the deposited charge distribution could be recorded as well. Therefore no uncorrelated background is visible in the time correlation plot.

The analysis performed on the collected data showed that by determining the position correlation of hits in the first and the second sensor, four different groups of hits associated to four particle sources could be identified in the cave and marked in Fig. 2.22. Ik this figure, T_0 denotes the beam target at which particles initiated from primary reactions are directly measured by the pion tracker, the other three sources are from most forward particles emitted into other detector and rescattered in all directions. In figure 2.25c the Δx-Δy correlation of the hits on the front and the rear sensor is shown. All four particle emission sources are visible. Group 0 stems from the primary target while groups 1 to 3 steam from three other detectors. The pattern presented in the figure comes from the fact that different sources emit particles at different angles, and therefore at different relative distances along x-axis. The gradual decrease in the y-direction results from detectors positioned below beam axis.

Since particles emitted at various θ angles traverse sensors area at a different effective depth of $d/\cos\theta$, where d is nominal sensor thickness, it will be reflected in the average energy deposition also following this scaling. Indeed this relation is shown in Fig. 2.26.

The average detection efficiency of single sensor side with respect to the reference coincidence signal of both scintillators was evaluated for two runs with different positions for the front scintillator which was rotated by $90°$ in the x-y plane between these

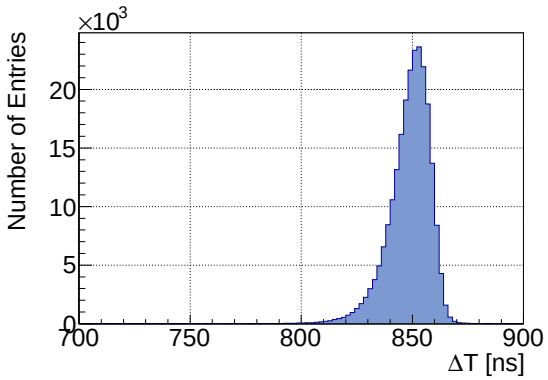

Figure 2.24: Example of the time correlation peaks for single experimental run.

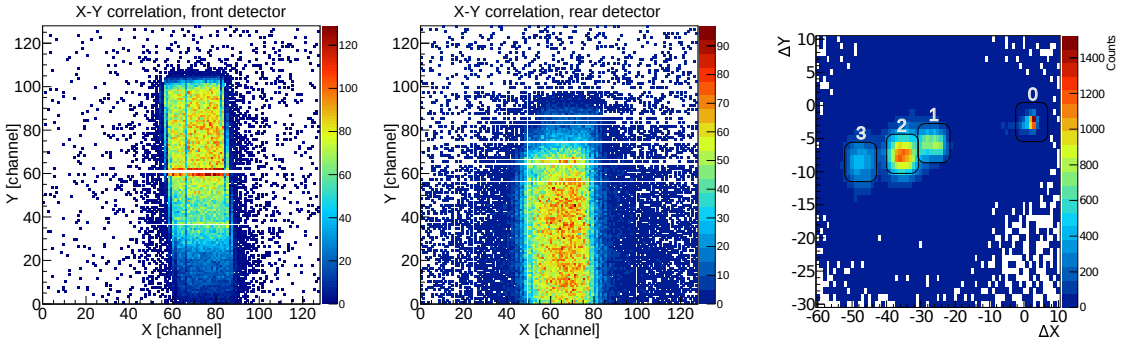

(a) Front sensor. **(b)** Rear sensor. **(c)** Position correlation.

Figure 2.25: Position correlation of the front and the back side of single silicon sensor in the Run K, respectively for the first and second tracking station, and relative position correlation of both sensors hit for all reconstructed tracks.

two runs. The results are summarized in Table 2.3. In both cases number is limited by the missing channels on both sensors and overlap of the scintillator shadow on the sensors surface. This is particulary visible in the second sensor, where the shadow projected by the particles went significantly beyond the outline of the detector sensor as shown in Figs. 2.25a and 2.25b.

Efficiency of full hit (x-y side pair) reconstruction in a single sensor can be calculated using the other detector as a reference. Though the coincidence of both scintillators could be natural choice as a reference, the missing full geometrical overlap of the first scintillator with both silicon sensors would bias the results. For the same reasone, the first detector cannot be use for measuring the efficiency of the second detector, but it is possible for the first detector using the hits from the second, by calculating the following relation:

$$\eta_1 = \frac{n_{1\&2}}{n_2}, \tag{2.3}$$

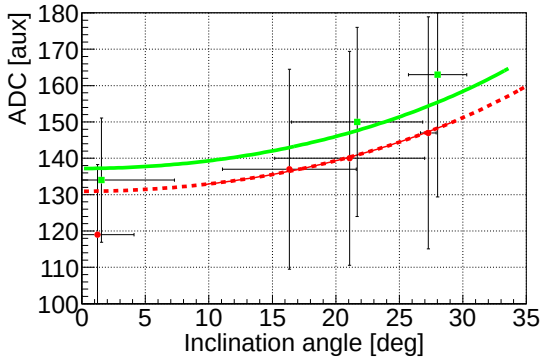

Figure 2.26: Angle dependency of energy deposited in the sensor.

Table 2.3: Fraction of events for the (F)ront and (R)ear n-XYTERS, in which at least one hit was registered.

n-XYTER	run D	run K
F-x	93.45 %	92.74 %
F-y	94.44 %	94.39 %
R-x	83.44 %	85.48 %
R-y	85.09 %	84.89 %

where $n_{1\&2}$ is number of events with hits reconstructed in the first and the second detector in the same event, and n_2 is number of events with reconstructed hits in the second detector. The track reconstruction efficiency η was extracted by comparing the number of coincidence events $n_{s1\&s2}$ from both scintilators, with the number of reconstructed hits in both silicons:

$$\eta = \frac{n_{s1\&s2}}{n_{1\&2}} \tag{2.4}$$

All the results are summarized in Table 2.4. Numbers given for both efficiencies must be understood as a lower limits for the results. Decrease of the efficiency has two major sources: (*i)* overlap of the front scintillator on the sensors area, (*ii)* broken channels in the detector, as can be seen in Fig. 2.25c.

Around 90 % of the events for each sensors side/n-XYTER chip are single hits events (Fig. 2.27a). The cluster size is defined as a number of neighbouring strips fired in the single event. All hits inside a single time window were considered. For cluster sizes higher than one, a clustering algorithm sums all signal amplitudes in the neighbouring strips to the total cluster amplitude.

The energy distributions for hits in the ADC units is shown in Fig. 2.27b. The distribution is fitted with convoluted Gaussian and Landau functions. The Landau function represents here the typical statistics of the charge carriers generated during the ionization process, and Gaussian represents the energy resolution of the detector. Since the noise level was cut off by the threshold settings, the noise peak presented in the figure was measured separately using the TT mode and pulser generator. It is known that during the PT working mode, the reference level of the n-XYTER output voltage signal is

Table 2.4: The front detector and the track reconstruction efficiency.

property	run D	run K
Front detector efficiency	92.0 %	95.9 %
Track reconstruction efficiency	86.4 %	71.4 %

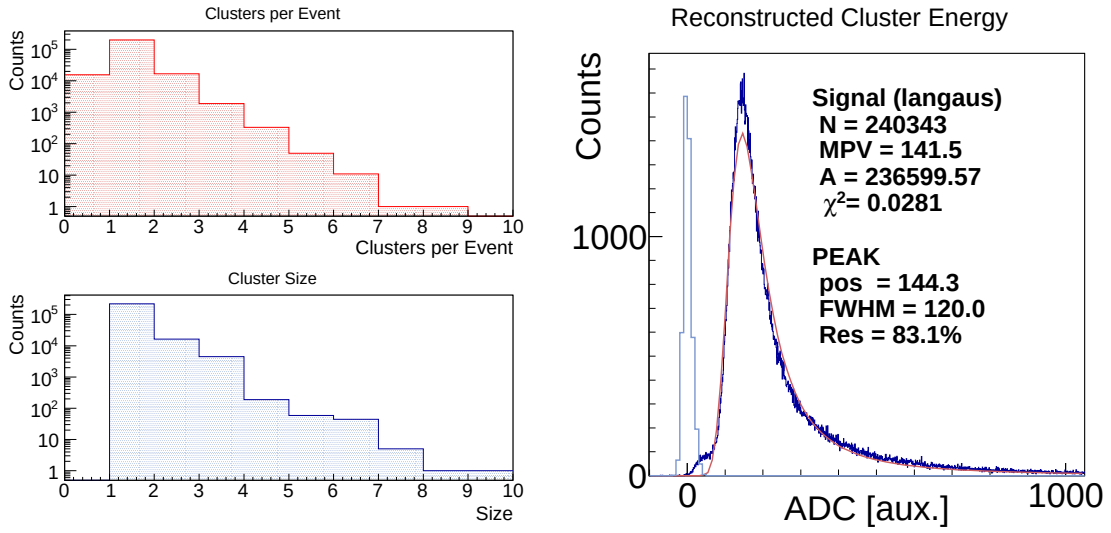

(a) **(b)**

Figure 2.27: (a) Multiplicity and size of the hit clusters for one side of the rear silicon sensors. Other three distributions are comparable. (b) Distribution of clusters amplitudes for the same sensor side. Bright blue peak on the left side is a noise peak recorded in separate measurements.

shifted by small value, introducing a systematic and constant offset into measurement of the noise level and generating base line corrections. Therefore the noise peak is shifted in the direction of signal peak, and the signal spectrum, aligned to the zero level is shifted into low energy range.

The measured noise has a standard width of $\sigma \approx 10\,\mathrm{ADC}$ units leading to a lower limit of the average Signal to Noise (SNR) ratio of 14. In fact, the real SNR value calculated from μ_S/σ_N, where μ_S is the mean value of signal distributions and σ_N is

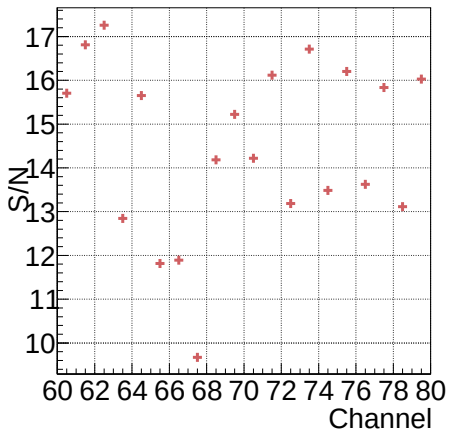

Figure 2.28: Signal to noise ration measured for single detector channels.

the width of the noise distribution, is higher due to shift fo the μ_S from the calibration procedure.

The obtained value is cross-checked and confirmed in a single channel measurements, where only events of single strip cluster are considered. It allows to omit the clustering procedure, and the energy fully deposited in single strip is used. Example for channels 60 to 80 on x-axis from Fig. 2.25a is shown in Fig. 2.28. The results from three other sides are consistent. The average SNR is almost three time higher than $5\sigma_{\mathrm{noise}}$ usually assumed value for the proper threshold settings.

In summary, the results obtained during this beam test showed a good tracking capability of the pion tracker prototype, even despite of the fact that the calculated efficiencies are lowered by the alignment and broken readout channels. The possibility to study particles crossing the detector surface at different angles opened the possibility for an experimental verification of expected $1/\cos\theta$ behavior of the energy deposition. Well shielded and grounded sensors and front-end modules ensured a very low noise level, almost not measurable with very conservative threshold setting. In the more precised analysis these uncorrelated noise events can be filtered out by applying additional time cut on the time correlation window.

Thanks to online analysis of the collected data, various bugs recognized in the acquisition system could be identified and reported. Errors in the acquisition code manifested themselves by very low stored data rates, resulting from the incorrect trigger correlation logic for the multi-SysCore and n-XYTER configuration. Since the data were correlated with the trigger signal on-fly, data affected by this error were lost, though properly registered by the front-end electronics. As a consequence, the first calculations of the detector efficiency resulted in values of order of $5\,\%$ to $10\,\%$. This errors was easily recognizable with the specific configuration of triggered system. Thanks to fast response of the code developers, a properly working version was delivered during the beam time and allowed to collect proper set of data, of which analysis was presented in this section.

2.7.2 Test at COSY synchrotron in FZJ Jülich

The experimental verification of the pion tracker at the COSY Cooler Synchrotron facility was planned as the final test before installation in the GSI accelerator infrastructure. COSY is a synchrotron operating in Forschungzentrum Jülich. It delivered a proton beam with a momentum of $2.2\,\mathrm{GeV/c}$ and allows therefore, unlike previous tests at SIS18, to test the detector directly in the beam. The tests were performed in cooperation with the CBM collaboration. All detectors were aligned along the beam axis. Just behind a scintillator monitoring the beam size and rate, two prototypes of the CBM Silicon Tracking Stations were placed. Further in the line two CBM GEM stations were located, followed by a single station with the FPGA module for radiation hardness tests. As last, the HADES tracking detectors setup were positioned. Behind all detectors, an additional multichannel scintillator hodoscope playing the role of main trigger was placed. While

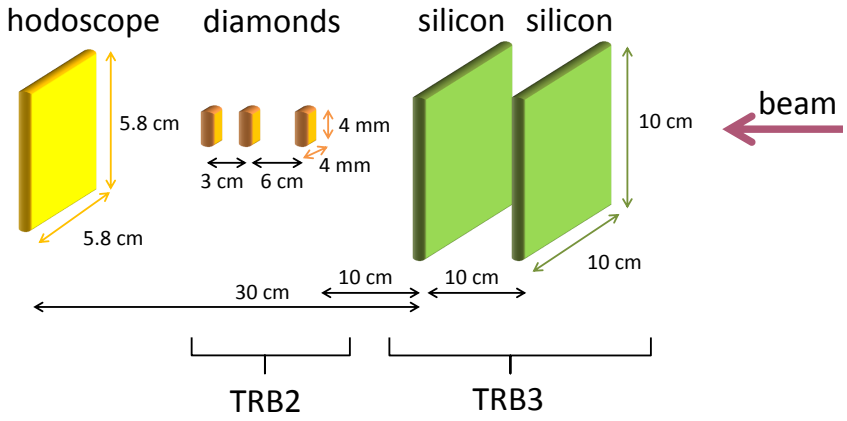

Figure 2.29: Schematic of the detectors configuration during the COSY tests.

this scintillator was considered as proper trigger since it assured that the beam particle traveled through all detectors, the first scintillator was used to monitor beam size and rate.

The HADES tracking detectors setup consisted of two pion tracker detectors and three $4\,\mathrm{mm} \times 4\,\mathrm{mm}$ diamond detectors for the HADES Start detectors [Pie+10]. The pion tracker was employing during this tests the native HADES DAQ with TRB3 for the first time. The start used the TRB2 (previous generation of the TRB boards) for the read out. Both detector systems were therefore integrated into a single acquisition system, where three diamond detectors played the role of reference detectors but also as additional tracking stations. In total, the system consisted of five detectors: two double sided silicon sensors and three diamond sensors. The trigger signal was provided by the CBM hodoscope placed behind the setup. The whole setup is shown in Fig. 2.29 and Fig. 2.30. All HADES detectors were located on a movable platform, allowing to move the silicons and diamonds up, down, and to side of the beam axis.

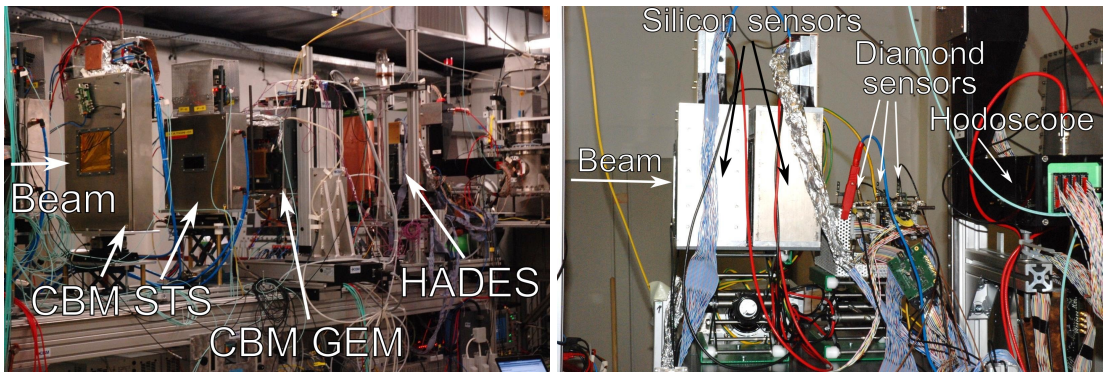

Figure 2.30: Picture of the whole test setup (left) and HADES related part (right).

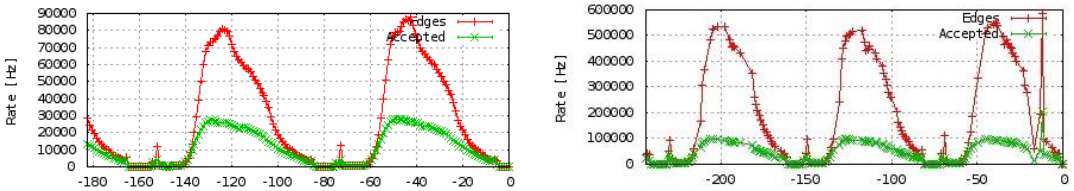

(a) Medium rate of 1×10^5 cts /s.

(b) High rate of 5×10^5 cts /s.

Figure 2.31: Spill shape as seen by the trigger detector. The red crosses (edges) are pulses from the trigger detector and the green points (accepted) are the trigger requests sent to the subdetectors.

The measurements at COSY aimed to perform a precise determination of the reliability of the TRB3 read out for the pion tracker. Though the TRB3 itself was already tested in many HADES and PANDA tests and beam runs, the performance of the readout system relays in the firmware programmed into the FPGA logic and therefore TRB3 together with the firmware had to be tested again in the beam test.

To reproduce the configuration expected in the final setup at the pion beam in GSI, each silicon station was read out by a single TRB3 board. In total two TRB3 boards were employed, and single TRB2 board was used to read out the diamond detectors. All TRB boards were connected to single hub – another TRB3 working as a data collector sending data from all three TRB boards over TrbNet to the event builder running on PC station. The same TRB3 board was used to run the Central Trigger System logic, delivering the trigger signal to all other TRB boards. Either the scintillator hodoscope, one of the diamonds detectors, or a random or regular pulser was used as a trigger source.

Due to the limited space available in the cave, silicons were enclosed in small aluminum chambers, used also in tests at SIS18. Diamond sensors have a threshold energy for creation of electron-hole pairs at the level of $13\,\mathrm{eV}$, which is significantly higher than the energy of visible light spectrum of $2\,\mathrm{eV}$ and therefore do not have to be enclosed in a light-tight chamber.

COSY generates beam spills of a $30\,\mathrm{s}$ length (Fig. 2.31), with micro spill structure of $700\,\mathrm{ns}$. To assure that all particles from one single micro spill are captured but not overlapping with particles from next micro spill, the time window for the event selection was set to $400\,\mathrm{ns}$. Measurements were performed at various beam intensities, from $2\,\mathrm{kHz}$ to $550\,\mathrm{kHz}$.

Figure 2.32 depicts the beam profile obtained from the online analysis. In the left column the hit position correlation on both sides of the first and second detector is shown. The size of the spot is determined by the size of the beam profile. In the lower picture, broken channels on the right side of the correlation plots are caused by damaged kapton tape cable.

The middle column shows the correlation of amplitudes of the deposited charges

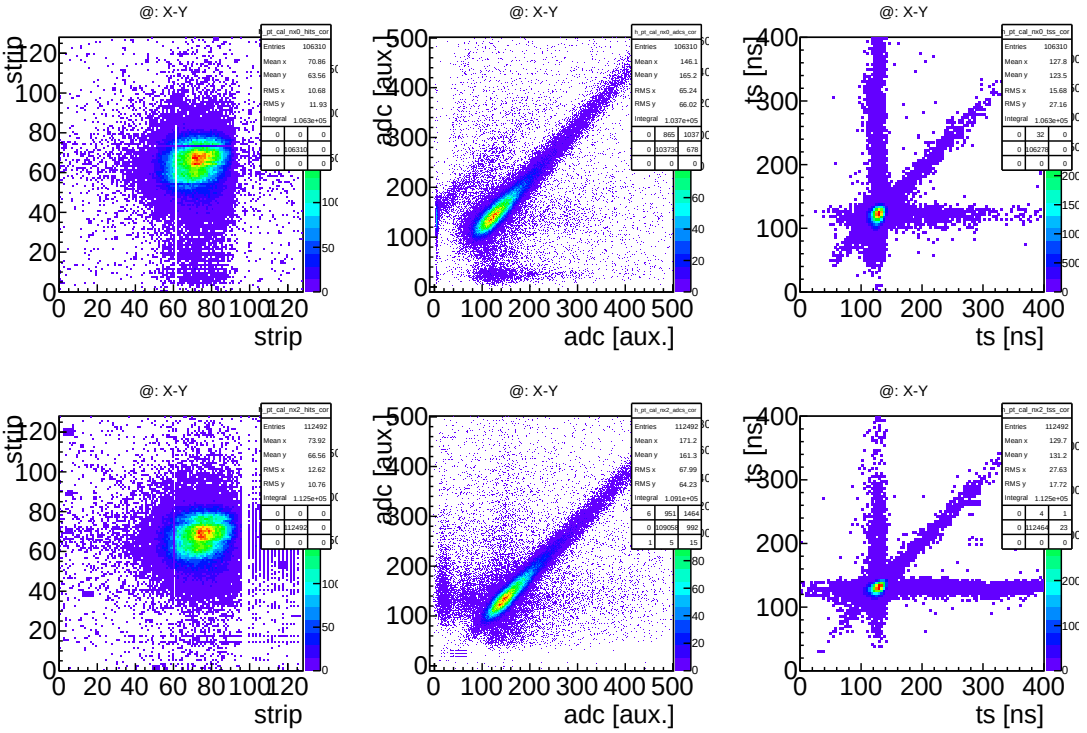

Figure 2.32: Beam profile, ADC correlation and time correlation for the first (upper row) and the second (lower row) detector station.

on both sides of single silicon sensor. The correlation is linear, though small offsets in either y or x directions are caused by systematic shifts of the base line. This effect can be corrected in the analysis by applying offset corrections. Small structures located close to the axes are related to signal on one side and a noise hit on the other side. Since the signal shows a clear separation between the noise level and the valid proton signal, this fake correlation can be removed by applying additional cuts.

The third column shows the time correlation on both sides. All signals are nicely peaked at a certain time value, chosen arbitrary by the event windows configuration.

The offline analysis of the high intensity data showed that the number of registered events with respect to the incoming rate gets lower. An example of such effect is shown in Fig. 2.33, where the x-axis represents the event number (pseudo time), and the y-axis the channel number. The analysis showed that this affects signals of negative polarity only.

This effect can be attributd [Sai] to the saturation of the pre-amplifier output which is illustrated in Fig. 2.34a. The n-XYTER pre-amplifier is a Charge Sensitive Amplifier (CSA) architecture and gain depends on the capacitor in the feedback loop of the amplifier. Since such an amplifier works as an integrator, after each input signal, the

output voltage rises to value equivalent to the integrated charge. The output of the pre-amplifier is connected to the input of a shaper circuit which differentiates this signal, and the amplitude of the signal on the output of the shaper is proportional to the step height on the output of the pre-amplifier. A continously rising level of the pre-amplifier output is not a problem for the shaper since it is sensitive to the signal change only. But after certain number of input signals, the level of the pre-amplifier output will reach the upper limit of the supply voltage and the circuit will saturate. To avoid this, the feed-back loop has an additional resistor to discharge the capacitor, leading to a slow decay of the pre-amplifier output. The decay rate is proportional to the resistor value, and for higher resistivity it is slower. If the value of resistivity is too big, the decay rate might be to slow too reduce the output base line to low values, causing the saturation of the pre-amplifier and therefore a cut-off of the amplitude after several close-by events. Such an effect will lead to a decreased amplitude on the shaper output due to cut-off of the amplitude of the pre-amplifeir output signal. If now the amplitude on the discriminator input falls below the threshold level, no events will be registered anymore until the input rate drops allowing the base line to restore its working conditions.

The value of the feedback resistance is responsible not only for the decay rate but also for the noise at the pre-amplifier stage. Therefore an optimal value was measured in the laboratory using an internal pulser. The problem of such pulser tests is, that the pulse has a rectangular shape, generating at the injecting capacitor alternatively positive and negative charge. Since the pre-amplifier can handle both polarities, the base line shift caused by the one polarity is neutralized by the other.

Therefore, to reproduce the effects from the beam tests in the lab, a special injector was constructed. It used an external waveform generator providing votlage signal shaped as a step-like function, and external injector capacitor. In this way one can reproduce the effects observed during the beam time. Figure 2.34b shows the shaper output (green curve) of one channel of n-XYTER.

The measurements were repeated in the pion tracker lab for both polarities. Here,

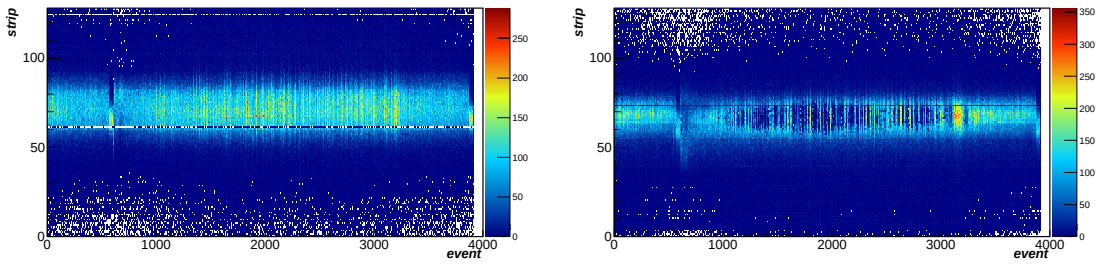

(a) Positive polarity. **(b)** Negative polarity.

Figure 2.33: Data looses during high rate tests.

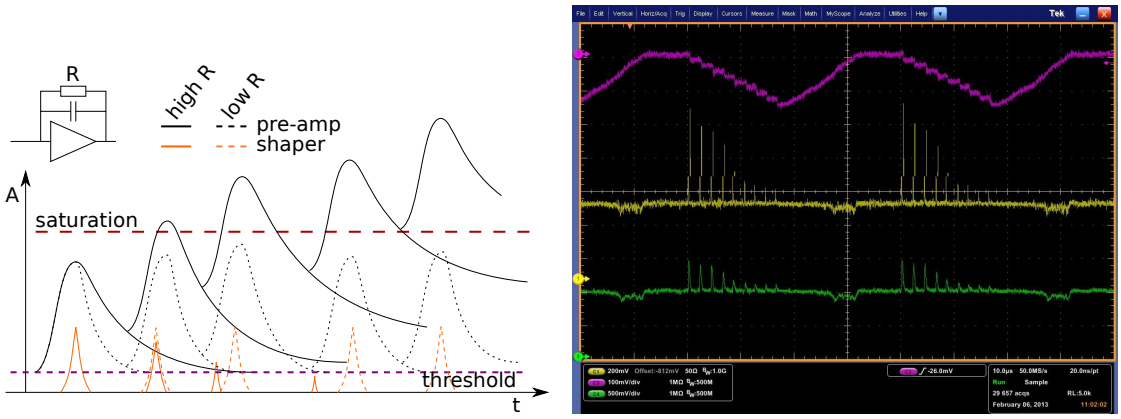

(a) Saturation of the pre-amplifier output. **(b)** Test with the dedicated pulser [Sai].

Figure 2.34: Saturation of the pre-amplifier output.

the injection pulser was calibrated to produce a charge of $4\,\mathrm{fC}$, equivalent of 1 MIP signal. The input frequency was varied in the range between $100\,\mathrm{kHz}$ to $500\,\mathrm{kHz}$ in steps of $100\,\mathrm{kHz}$. For each frequency and feed-back resistance setting, a series of 20 steps with a length determined by the frequency period was injected to the pre-amplifier input through the injection probe. Each measurement was repeated 100 times and the average number of registered counts on the output was calculated. The value of the feed-back resistance register was sweeped in the range of 35 to 130 for both polarities (arbitrary units of the DAC register). Final results are presented in figure Fig. 2.35. The count rate is presented as a function of the feedback resistance. The feed-back resistor value is represented in terms of the digital register settings, where a higher value translates into a lower resistance. Values below $100\,\%$ indicate data looses. The saturation effect is only observed for negative input polarities although the reason for the different influence of

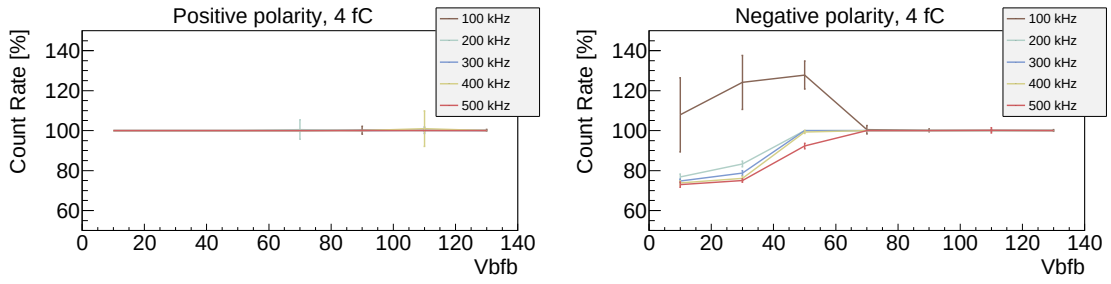

(a) Positive polarity. **(b)** Negative polarity.

Figure 2.35: Measurement of the influence of the feedback resistance on measurement rate.

positive and negative polarity is not understood. There was also no clear explanation found for the strange behavior at $100\,\mathrm{kHz}$ for negative input polarities, though this effect was reproducible in a series of measurements. One possible option is that additional noise source present during the measurement inducedd additional signals.

The default value of the discharge resistor used until this tests was 30, and after the measurement was changed to 130.

In summary, these measurements allowed to finalize preparation for the commissioning of the pion tracker before his employment with secondary pion beams at GSI. For the first time the full setup of pion tracker and the TRB3 was used with high rate beams. Problems with high rate beams were observed for the first time during this test. Those were reproduced and solved in the lab. The proper responses to trigger request, the event selection and data sending were tested. Minor bugs in the TRB3 firmware were identified and fixed. The tests resulted in the implementation of a real-time monitoring of the beam profile, by direct access to the registers inside the TRB3. This feature was very helpful in the commissioning of the pion tracker and in the pion beam.

3

Comissioning for the pion beam experiments

The assembling of the pion detector has started in January 2014. During the mounting procedure in the NE5 area, all quadrupole and dipole magnets located there were switched off by the accelerator operators for the safety reasons since the magnets are supplied with high currents and are in close distance to the tracking chamber. In the first phase only detector in the NE5 area was assembled and tested. In the second phase also detector in the HADES cave was assembled. Finally, the whole system was tested using a monoenergetic proton beam at the end of April 2014. The purpose of this procedure was to test the whole DAQ system with the integrated pion tracker and perform a momentum calibration for the pion campaign.

3.1 Assembling of the tracker chambers

Figure 3.1 shows the tracking station after being assembled in the NE5 area. The left photo shows the chamber installed in the beam pipe. The beam comes from the right side of the picture. The front-end modules and HV adapters connected to the chamber are shielded by a copper box. Next to the chamber the chiller is placed. The chiller had to be moved to the same level as the detector to avoid pumping the coolant from the ground level to the level of chamber. This also minimized the thermal losses due to longer cooling pipes. The beam pipe is around $2.5\,\mathrm{m}$ above the floor level. The TRB3 board is located below the beam pipe. All power supply modules are placed on the

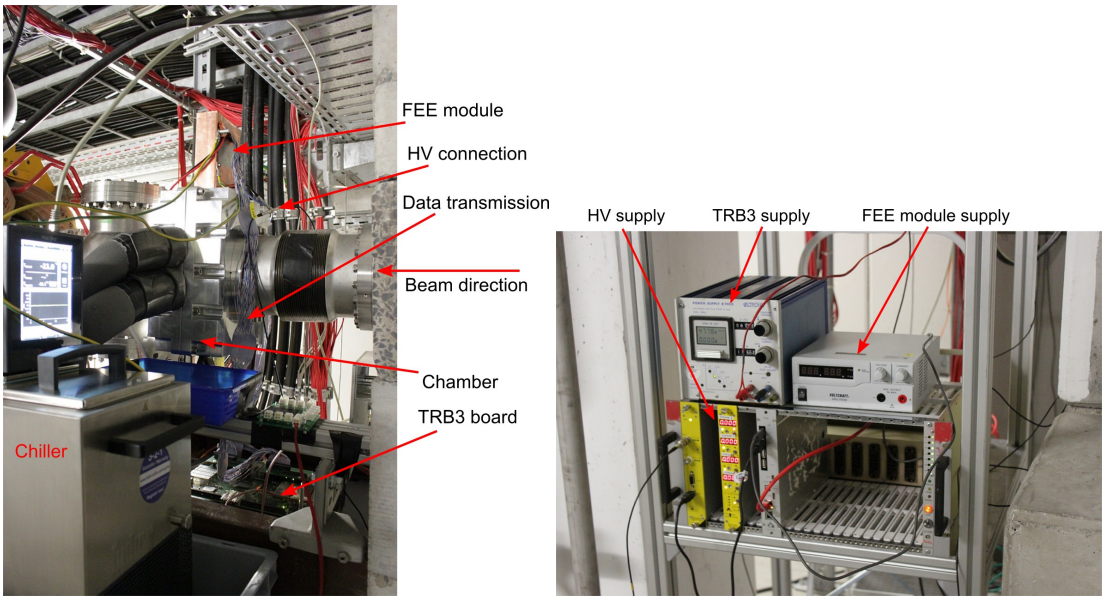

(a) Chamber assembled in the beam pipe.

(b) Power supply station.

Figure 3.1: Pictures of the first tracking station after assembling in the NE5 area. All electronic units (fee and TRB3 readout) are already connected. The cooling for the silicon sensor is connected and operating.

ground level inside the tower carrying the chiller.

The chamber is attached on both sides directly to the beam pipe. The front side of the chamber is connected to the pipe using spring element, since the mounting would have not been possible with fixed length elements. The chamber had to be lifted up to $2\,\mathrm{m}$ above ground using manual rope lifts. First of all the back side of the chamber was attached to the beam pipe and afterwards the spring element was attached to the front side. Due to weight of the chamber, the beam pipe is additionally supported to avoid deformation (supporting frame not visible in the picture).

After the mounting process, the detector bias was raised up to the nominal value of $150\,\mathrm{V}$. The leakage current of the detector was $1.9\,\mu\mathrm{A}$ as expected. Next, the front end electronics module were attached to the chamber and the noise performance of the system was tested. The detector was biased again at the nominal value and the noise spectrum was measured at a nominal threshold setting of 35. After some corrections of the grounding, the noise rate was at the level of few counts per second for all 128 channels for each of two n-XYTERs.

In the next step, the air was pumped out of the beam line and a vacuum of $1.5 \times 10^{-7}\,\mathrm{mbar}$ was achieved. At this point the cooling system was turned on and after $3\,\mathrm{h}$ of slow cooling, temperature of $-20\,^{\circ}\mathrm{C}$ was achieved. The leakage current of the sensor was reduced from $1.9\,\mu\mathrm{A}$ to $0.4\,\mu\mathrm{A}$ at $150\,\mathrm{V}$ bias.

(a) Front view. **(b)** Side view.

Figure 3.2: Pictures of the second tracking station after assembling in the HADES cave.

Afterwards, the preparation procedure of the SIS18 operation started, the NE5 area was closed and the magnets were turned on. The operating magnets introduced noise in the n-XYTER attached to the ohmic side of the silicon, even despite of the fact that the magnets are supplied with DC current not involving high frequency signals. Additional work was required to reduce the noise level to a rate of few hundred thousands up to one million counts per second for all channels of this n-XYTER. Other n-XYTER connected to this sensor experienced only a noise rate on level of 50×10^3 counts per second. Since such high noise reduces detection efficiency of one detector side due to an introduction of the dead time, different methods to eliminate this problem were considered, including the construction of a plastic separator to electrically isolate the chamber from the beam pipe. But the risk related with a dismounting and further remounting of the chamber was estimated as too high. Finally only actions related to the improvement of the grounding were taken.

Various combinations of ground connections between the different parts of the system were tested resulting in a reduction of the noise rate of the problematic n-XYTER to level of few hundred thousands counts per second. This effect of the noise is reflected in small detection efficiency drop in the first tracking station to level of around $87\,\%$ to

Table 3.1: Detection efficiency for each stations during pion beam runs, and overall tracking efficiency for both beam runs.

Station	July run	August run
NE5	$92.5\,\%$	$86.5\,\%$
HADES	$93.2\,\%$	$90.2\,\%$
Tracking efficiency	$87.5\,\%$	$78.4\,\%$

$90\,\%$ during the pion beam (shown in Table 3.1). The first two rows show results for a single detector stations, the tracking efficiency is an efficiency of reconstructing full pion track. Evaluation of the pion beam results is presented in the Master Thesis of Wirth in [Wir15].

Figure 3.2 shows the detector chamber assembled in the HADES cave. The assembling and testing procedures were the same like for the first station. In the HADES cave, detector did not experienced any side effects from operating magnets, and noise count rate was on the level of ten. Leakage current of the cooled detector was at level of $1\,\mu\mathrm{A}$.

3.2 Calibration with proton beam

For the momentum calibration a monochromatic proton beam of intensity in range of $10^6\,\mathrm{part}\,/\mathrm{s}$ to $1.4 \times 10^7\,\mathrm{part}\,/\mathrm{s}$ and central beam momentum of $2.68\,\mathrm{GeV}/\mathrm{c}$ was used. Since the bending radius of the dipole magnet depends linearly from the particle momentum, the calibration procedure was obtained by changing the central beam momentum p_0 of the magnet settings and keeping the proton momentum p fixed. This has the same effect as changing the momentum of the proton beam and keeping the magnets settings fixed. While the last procedure requires more actions in the accelerator configuration, the second requires only to change a current in the dipole magnets. In this case, fixed momentum at different dipole settings must be translated to equivalent momentum with fixed dipole, at which detector will measure the same response – bending of the beam trajectory.

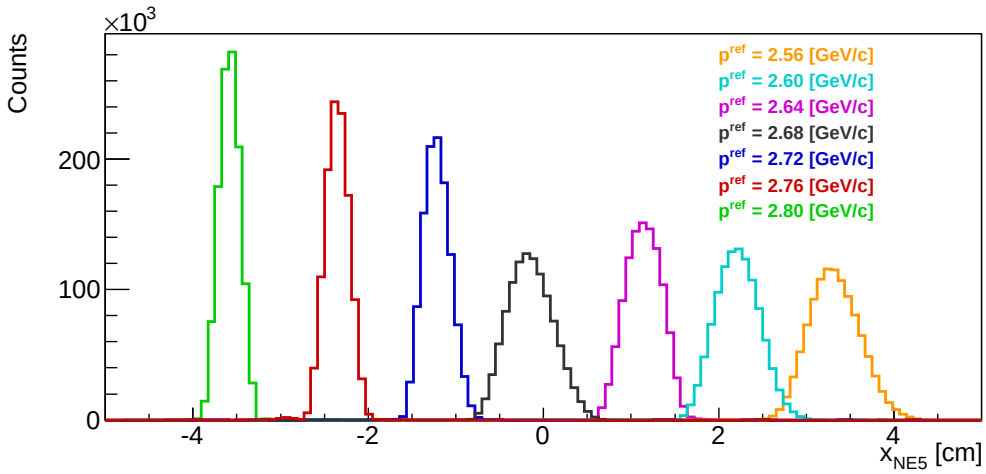

Figure 3.3: Beam spot positions for various settings of the dipole bending power.

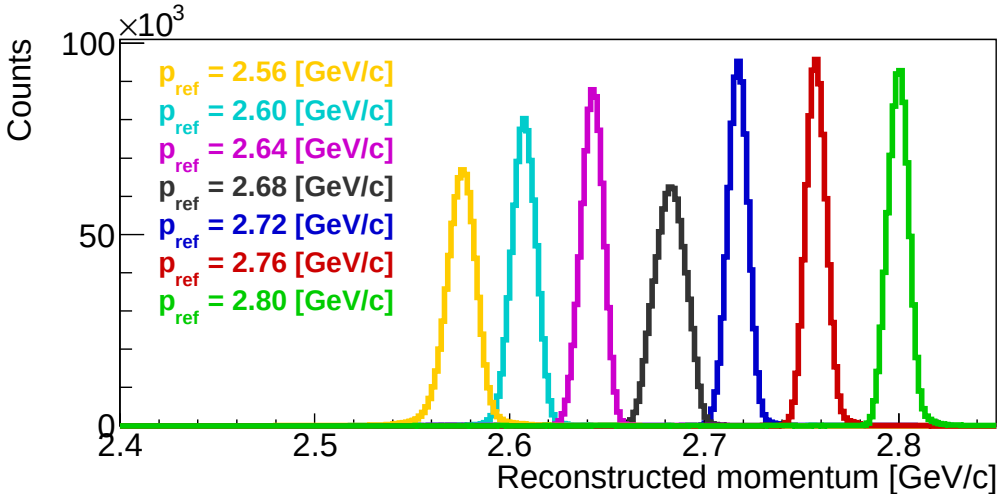

Figure 3.4: Momentum reconstruction results.

3.2.1 Momentum reconstruction

The calibration of the beam line was performed in seven steps. In each step, proper settings of the bending dipoles were recalculated to emulate changes of the proton beam momentum and the momentum of the beam was kept fixed. In each step, a beam run was performed and the data from both silicon sensors were collected. In the offline analysis of the data, for each event a pair of hits on both detectors was reconstructed and the emulated momentum of the beam was calculated on the basis of reconstructed hits position, as explained in Section 1.2.

The positions of the beam spots for different runs are shown in Fig. 3.3. For the first station, position of the hits along the x-axis are most relevant and y-coordinate can

$p_{\mathrm{ref}}\,/\,\mathrm{GeV/c}$	$p_{\mathrm{fit}}\,/\,\mathrm{GeV/c}$	$\sigma_{\mathrm{ref}}\,/\,\%$
2.56	2.58	0.29
2.60	2.61	0.24
2.64	2.64	0.21
2.68	2.68	0.27
2.72	2.72	0.19
2.76	2.76	0.18
2.80	2.80	0.19

Table 3.2: Summary of the momentum calibration. The first column shows the reference momentum values calculated from dipole settings. The second column shows fit results and the third column presents the resolution obtained from the fit.

be neglected. The momentum values listed in the legend are the calculated emulated momentum values for given dipole setting.

In the Fig. 3.4 results of the momentum reconstruction using beam transport is shown. Calculations were done event-wise with a fixed beam central (reference) momentum value. A comparison of the reference values and fitted values deduced from the reconstruction is shown in Table 3.2. Resolution of the fits given in this column is defined as the relative to the fitted momentum. All obtained resolutions are below the requested resolution of $0.5\,\%$.

3.3 Summary and conclusions

The pion tracker detector for the pion beam campaign at the HADES detector has been constructed at TUM and successfully run in two beam times in 2014. Two stations of the detection system employed various components like silicon sensors, the n-XYTER front-end electronics, the TRB3 and the SysCore readout boards. The detection system has been equipped with the cooling system for the silicon sensor.

Results of the laboratory tests allowed to characterize the components of the detector and evaluate the properties of the detector systems like the detection efficiency of the silicon sensors and the working parameters (dead time, discharge rate, threshold calibration and the base line corrections) of the n-XYTER chip. The detector was tested also in two beam tests running at the SIS18 and COSY accelerator setups. They both confirmed capability of the system to perform tracking of the particles at low and high beam rates.

The upper beam rate limit for a single station was estimated at the level of $2\,\mathrm{MHz}$ (single channel dead time) for a single channel and the maximum of $32\,\mathrm{MHz}$ for a whole tracking station (limitation from the electronics readout).

Detection efficiency for various sensors varied in the range of $92\,\%$ to $97\,\%$ in the laboratory tests and of $85\,\%$ to $95\,\%$ in the beam tests, and was in most cases dominated by the combination of the broken strips in the silicon sensor or in the read out electronics. The track reconstruction efficiency was determined to be in the range of $71\,\%$ to $95\,\%$ for the beam runs and undergo the same side effects of the missing channels.

The detector was able to perform online tracking of MIP. The low noise level of the input stages allowed for keeping the thresholds of the electronics at the levels well separated from the noise levels. However, operation with the magnets in the NE5 area revealed problems with the high noise level, which could not be fully understood and fixed in the beam preparation period. However, due to low dead time and high count rates allowed on the input, the noise occupancy on the channels did not disturbed the proper operation the tracking stations, and affected the detection efficiency only in the minimal way.

Success of the pion beam campaign in 2014 will allow for further pion experiments planned for 2017, in which the pion tracker will be again involved.

Part II

Inclusive Lambda-hyperon production in pp reactions at 3.5 GeV kinetic energy

4

From astro to particle physics

Neutron stars are massive objects created in core collapse supernova explosions. Typical radii of about $10\,\mathrm{km}$ and masses between $1.4\,\mathrm{M}_\odot$ and $2\,\mathrm{M}_\odot$ make them very dense and compact. The density inside the core of a neutron star can reach values of several normal nuclear matter densities $\rho \gg \rho_0 = 0.16\,\mathrm{fm}^{-3}$ [WCS12][1]. Besides the very first, classical model of the neutron star as a huge nucleus, there are several other hypotheses predicting configuration of such astrophysical object, e.g. (*i)* hyperonization, predicting a hyperon rich core [ST83; BB98] (*ii)* pion condensates [BW65; Mig72; Saw72; Sca72], (*iii)* Kaon condensates [LLB97; KN86; NK87], (*iv)* a phase transition to quark matter [Web99]. The three last hypotheses are known as *exotic models of dense matter*. Some of these scenarios are depicted in Fig. 4.1.

In the hyperonization scenario, a starting point is the low density nuclear matter composed of nucleons. While increasing the density, the Fermi pressure of such fermion composition increases. At the very high densities achievable in the core of a neutron star, the Fermi energy accumulated in the constituent particles could result in the creation of heavier particles. Since the core of the neutron star is composed of nuclear matter, a releasing of the Fermi pressure would lead to the appearance of favourable new degress of freedom in the system – strangeness. As a consequence, at certain densities, hyperons should start populate the core of neutron stars. First theoretical predictions about the presence of hyperons in the core of a neutron star were given by Ambartsumyan and Saakyan in [AS60].

The understanding of the Λ interactions with the matter is nowadays a key issue to

[1] $0.16\,\mathrm{fm}^{-3} = 3 \times 10^{14}\,\mathrm{g\,cm}^{-3}$

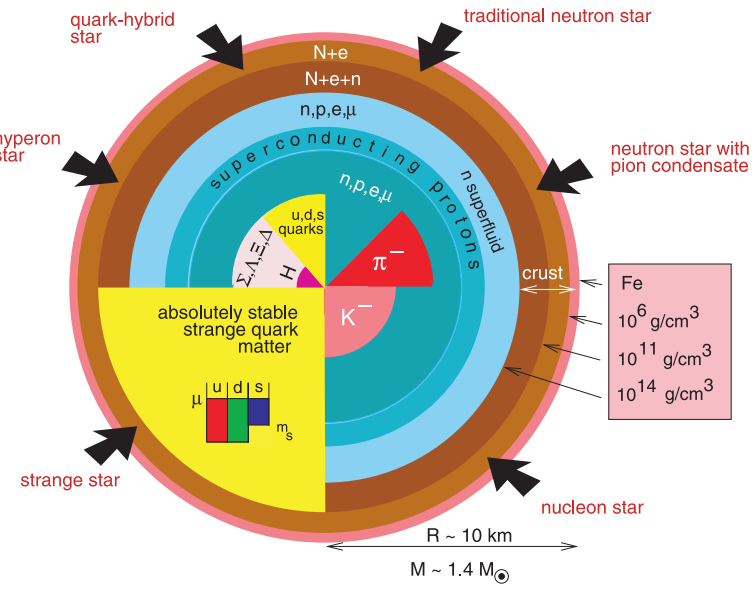

Figure 4.1: Different scenarios of the neutron star matter composition [Web01].

describe high density states of matter, e.g. neutron stars.

The Λ hyperon with the mass of $1115.683 \pm 0.006\,\mathrm{MeV/c^2}$ is the lightest strange baryon containing one strange quark, and its constitue is uds. As an isospin singlet state together with the triplet Σ baryons, composes the lightest strange multiplet in the baryon octet. With a lifetime of $c\tau = 78.9\,\mathrm{mm}$ Λ decays weakly mostly into pairs of a nucleon and a pion [Oli+14].

The thermodynamical approach to describe the nuclear matter is a hadronic equation of state (EoS). Though EoS of nuclear matter is in general understood at saturation densities, much less is known when extrapolating to higher densities like in the case of the already mentioned neutron stars. Differences in the EoS assumptions lead to different predictions for the neutron star.

Existing models of nuclear matter predict that the inclusion of hyperons softens the EoS and this leads to a reduction of maximum mass of the neutron star. Brueckner-Hartee-Fock (BHF) calculations, with the inclusion of the hyperon-nucleon interaction (YN) lead to maximum mass of $1.47\,\mathrm{M_\odot}$ [Vid+00], further inclusion of the hyperon-hyperon interactions (YY) reduces the mass to $1.34\,\mathrm{M_\odot}$ [SR11] and three body interactions (NNN) set the limit on $1.26\,\mathrm{M_\odot}$ [BBS98; BBS00].

These predictions are not in agreement with the newly discovered very massive neutron stars (J1614-2230 with a mass of $1.97 \pm 0.04\,\mathrm{M_\odot}$ [Dem+10] and of J0348+0432 with a mass of $2.01 \pm 0.04\,\mathrm{M_\odot}$ [Ant+13]) and rised the so called Hyperon Puzzle in the neutron star.

These measurements set stringent constrains on the possible EoS for neutron star matter, since as shown in Fig. 4.2, all the curves that do not cross the high mass values are ruled out.

Calculations conducted in the context of Relativistic Mean Field (RMF) models partially solve the problem. By inclusion of scalar (σ), vector (ω) and isovector (ρ) meson-interactions for baryon-baryon (NN), above mentioned results from BHF were reproduced. Additional terms with strange scalar ($\sigma*$) and vector (ϕ) mesons for the hyperon-nucleon (YN) part, yield in the upper limit for the mass to $2.4\,\mathrm{M}_\odot$ [WCS12] (softening of the EoS by $\sigma*$ was neglected). The repulsive core of the YN interaction is crucial in this calculations.

In another approach, the BHF calculations with three body forces (TBF) in combinations of NNY, NYY and YYY interaction were performed in [Vid+11; Yam+15]. By providing the additional repulsion required for the stiffening of the EoS, both authors obtained contradictory results. While Vidaña et al. claims that stiffing of the TBF is not sufficient to match the experimental constrains for the mass, Yamamoto et al. achieved the limit of $2.0\,\mathrm{M}_\odot$.

Quantum Monte Carlo calculations from [Lon+15] used parametrized ΛNN potential dependent on the onset of Λ hyperons in the core. They found that the presence of Λ particles in neutron matter is energetically disfavored at least up to $\rho = 0.56\,\mathrm{fm}^{-3}$. Thus, the results are not inconsistent with the experimental measurements, they also do not draw any conclusion about the composition of neutron stars. Lonardoni et al. underline in the paper the need of deeper study of the ΛN and ΛNN potentials.

An important aspects of all these calculations is the hyperons potential in matter. Sparse data of the hyperons (Λ, Σ and Ξ) interaction with nucleons is provided mostly

Neutron star mass–radius diagram.

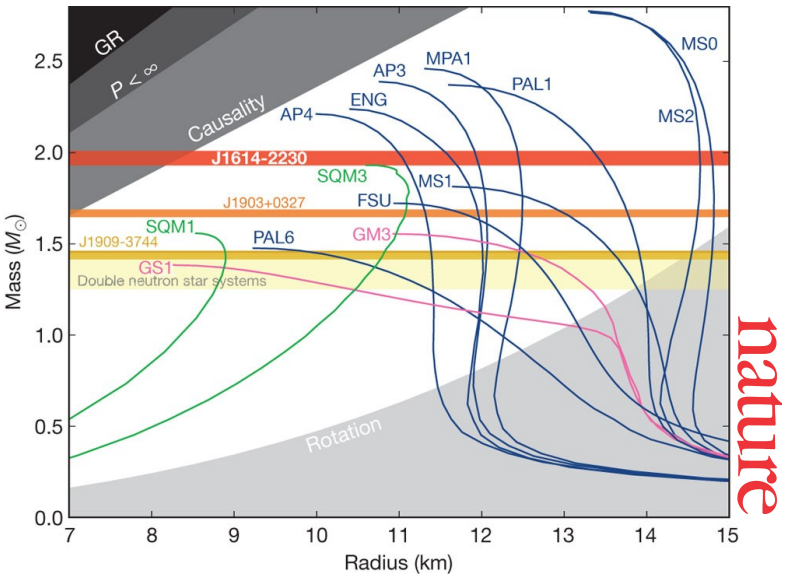

nature

PB Demorest *et al. Nature* **467**, 1081-1083 (2010) doi:10.1038/nature09466

Figure 4.2: Selected Equation of State models and the constrains from the J1614-2230 neutron star measurements.

by the hypernuclei experiments and the scattering experiments. Forming of the Λ-hypernuclei was confirmed in various experiments, starting with the atmospheric balloons measuring hypernucleus from cosmic radiation at about $26\,\mathrm{km}$ above Earth surface [DP53], through photographic emulsions and bubble chambers the measurements allowing to observe decays of hypernuclei, and ending up with the cosmic radiation and the accelerated beams (protons, K^-, pions), and an attractive potential of $-30\,\mathrm{MeV}$ was measured [MDG88; Mil07]. The Λ-hypernuclei are recognized as stable at the nuclear time scales of $10 \times 10^{-23}\,\mathrm{s}$ [BBG12]. In opposite, the Σ-hypernuclei were even not observed at such short time scales. This probably results from the strong $\Sigma\mathrm{N} \to \Lambda\mathrm{N}$ conversion reaction, though due to the isovector interaction for a core with $N < Z$ and small A it was possible to produce quasi-bound ${}^{4}_{\Sigma}\mathrm{He}$ [BBG12]. In the nuclear matter the Σ-hypernuclei is considered as unstable with repulsive potential of $10\,\mathrm{MeV}$ to $50\,\mathrm{MeV}$ [Bar+99; DR08; Koh+06] at normal matter density of $\rho_0 = 0.16\,\mathrm{fm}^{-3}$. The production at AGS of even more technically demanding Ξ-hypernuclei ($S = -2$) resulted in the cascade attractive potential of $-14\,\mathrm{MeV}$ [Fuk+98; Kha+00]. Study of the cascade is difficult due to strong $\Xi\mathrm{p} \to \Lambda\Lambda$ reaction and fast decay to the Λ pairs.

Complementary information with scarce data statistics is provided by the scattering experiments from 60s [Ale+68; Sec+68; Eis+71] and the chiral effective field theory (χEFT) theoretical calculations [Hai+13] at leading order (LO) and next-to-leading order (NLO). Though results of both are different, they confirm attractiveness of the interaction for low hyperon momenta and repulsive core of the $\Lambda\mathrm{N}$ interaction at higher Λ momenta in the NLO calculations.

In the sector of double hyper-nuclei, only a few events of $\Lambda\Lambda$-hypernuclei were recorded up to now, most recent results suggest attractive but very weak interactions [Tak+01].

The leading facilities in the hypernuclear sector are AGS, BNL, FINUDA, J-PARC, KEK, all employing either pion and Kaon beams. Future HyperNIS [VDA+14] experiment at Nuclotron in Dubna is promising in terms of statistics of produced Λ-hypernuclei with light element beams.

Information about the potential could be also available in the reactions involving heavy ions (HI) at moderate energies of $1\,\mathrm{GeV}$ to $3\,\mathrm{GeV}$ beam collisions. Such reactions were studied e.g. by ANKE at COSY and FOPI and HADES in GSI Darmstadt. By measuring the momentum spectrum of the tested particle, or evaluating from the measured data a nuclear modification factor R_{AA} of the tested particle in two different systems (e.g. in the HI collision and in the reference pp reaction), and with help of the models employing the potential in the matter, one can make assumptions on the potential strength. If the particle feels a medium potential, the momentum spectrum will be modified accordingly. This idea follows the same line as the measurement of the electron and positron momentum spectrum, where attraction and repulsion respectively modifies the spectrum due to the Coulomb interaction with the core [Rei50].

The study of hadron properties in nuclear matter can be treated using Chiral Perturbation Theory (ChPT). ChPT assumes that the hadron mass is given by the spontaneous and explicit breaking of the chiral symmetry. One can further establish a relationship between the order parameter of the spontaneous symmetry breaking, the $< q\bar{q} >$ condensate and the mass of hadrons. Models [KLW90] based on ChPT also predicts a dropping of the $< q\bar{q} >$ condensate as a function of the system density and temperature. This can be translated into a modification of the hadron massess as a function of the density and temperature of the system too. Hence the study of the hadron properties within nuclear matter, is though to provide information about the possible onset of chiral symmetry restoration.

Kaplan and Nelson in [NK87; KN86] applied this method to predict the modification of Kaon and anti-Kaon within nuclear matter. In the medium effect is opposite for Kaons and anti-Kaons, the first will experience an increase of their vacuum mass within nuclear matter, while for the latter a decrease of the mass is predicted [SMB97].

Hence Kaons produced in-medium, after leaving the dense matter region, will experience a kick in the momentum after the onshell mass restoration. Figure 4.3a presents K^0_S data from Ar+KCl reactions measured by HADES at a beam kinetic energy of $1.756\,\mathrm{GeV}$. The use of the neutral Kaons allows to be insensitive to additional Coulomb potential. Color lines present simulations of IQMD [Aic91; Har+], where the potential is parametrized with α and expressed as $U(\alpha) \simeq U_0 + U'\alpha$, with $U_0 \approx 0.8\,\mathrm{MeV}$ and $U' \approx 38\,\mathrm{MeV}$. Mass is treated within the linear Ansatz as $m^* = m_0 + U(\alpha) \times \rho/\rho_0$.

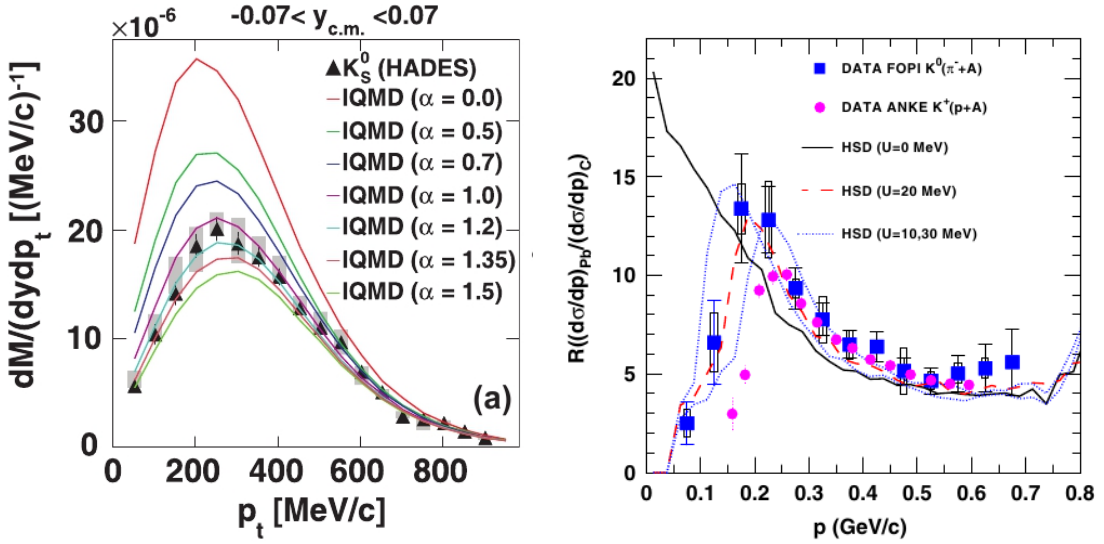

(a) KN potential with ArKCl [Aga+10]. **(b)** R_{AA} for FOPI and ANKE data [Ben+09].

Figure 4.3: KN potential measurements.

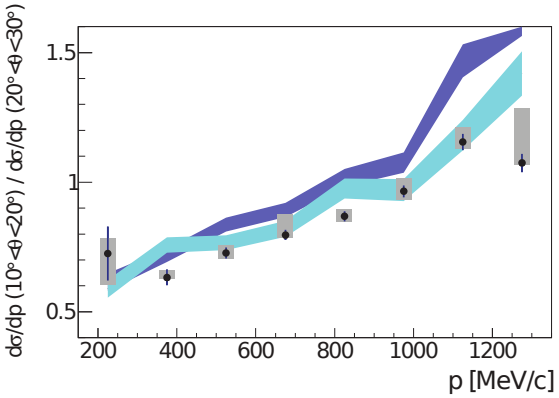

Figure 4.4: Cross-section ratio of two different angle regions of the K^0_S production in pNb data at HADES. Dark blue band is the ratio predicted by the original GiBUU model while the light blue presents results from the GiBUU where KN potential was tuned to the obtained data [Aga+14a].

The KN potential was found to be $40\,\mathrm{MeV}$ (for $\alpha \approx 1$) [Aga+10].

Figure 4.3b shows yield ratios in production of Kaons in FOPI and ANKE data measured in two different system configurations. FOPI measured K^0_S in pion induced reaction with nuclear targets of Pb and C (blue points) [Ben+09]. ANKE measured K^+ production in proton induced reactions at various nuclear targets: D, C, Cu, Ag and Au [Büs+04]. The figure represents ratio of K^+ yields for Au and C systems (pink points). The observed shift to higher momenta values is attributed to additional Coulomb interaction of charged Kaons. Lines represent HSD (Hadron String Dynamics) [EC96; GCG98; CB99] calculations, the best fit is extracted for a potential value of $20 \pm 5\,\mathrm{MeV}$ for Kaons with zero momentum at normal nuclear density. This is in contradiction to the value of $40\,\mathrm{MeV}$ extracted by HADES in Ar+KCl system [Aga+10], however these results are obtained with different models and therefore are strongly model dependent.

The K^0_S potential was also probed in the analysis of pp and pNb reaction at $3.5\,\mathrm{GeV}$ kinetic beam energy [Aga+14a]. The cross-section production in two different angular regions (Fig. 4.4) was compared with the GiBUU model (dark blue band), which was tuned for the K^0_S production (light blue band) and value of $40 \pm 5\,\mathrm{MeV}$ was also obtained, which is in consistency with the previous HADES data. This analysis of the Kaons properties in p^+A reactions, contrary to the previous carried out, employed a transport model (GiBUU) for the interpretation of the experiemntal data, for which the p^+p and p^+n processes were calibrated accurately with the experimental data from elementary reactions measured by HADES. The potential effect is added on the top of a controlled systems where seplica of single nucleon-nucleon reactions are added up incoherently to build the reference system and hence is much more controlled than previous studies where elementary cross-sections were not estimated carefully.

A similar analysis can be performed for Lambda hyperons case. HADES published results for an inclusive Λ production in pNb reaction [Aga+14a]. Results from this work will therefore allow to compare ratios of distributions with the available models and make assumptions on the Λ potential in medium.

4.1 The HADES experiment

The High Acceptance Dielectron Spectrometer (HADES), shown in Fig. 4.5 is a magnetic spectrometer operating since 2002 at the SIS18 synchrotron in GSI Helmholtz Institute for Heavy Ion Research in Darmstadt, Germany. It is a universal tool allowing to measure various charge hadrons (protons, pions, Kaons, light elements) and leptons (electrons and positrons) resulting from particle productions with pion, proton and heavy ion-induced reactions at various nuclear targets in the beam energy range of $1\,\mathrm{GeV}$ to $3.5\,\mathrm{GeV}$. With his versatility, it is an excellent tool to study hadron properties in vacuum or cold and hot nuclear matter. It probes the low energetic part of the matter phase diagram, and research performed at HADES is complementary to the ones in other leading institutions and experiments like Na61, Na49/SHINE, CERES at SPS (CERN), STAR and PHENIX at RHIC (Brookhaven) and LHC (ATLAS, ALICE and CMS experiments), probing other regions of the phase diagram. HADES probes region, where confined nuclear matter is dominated by baryons, for example nucleons and hyperons, and its excited states – resonances.

Its six-folded geometry covers full azimuthal angle in $85\,\%$, and the polar angles in range of $15°$ to $85°$. In the interesting range of vector mesons it provides excellent mass determination resolution of $\Delta M/M \approx 2.5\,\%$.

The liquid hydrogen (LH_2) target used in pp experiments has geometry of a L-shaped pipe, of which the upper arm is connected to refrigerator located above the experimental target, and the vertical arm is retracted into the beam pipe. Construction of this part of the target is shown on Fig. 4.6.

Though liquid hydrogen occupies major volume of the vertical arm, the actual target is located at the end of the arm. To provide undisturbed transport of the beam particles,

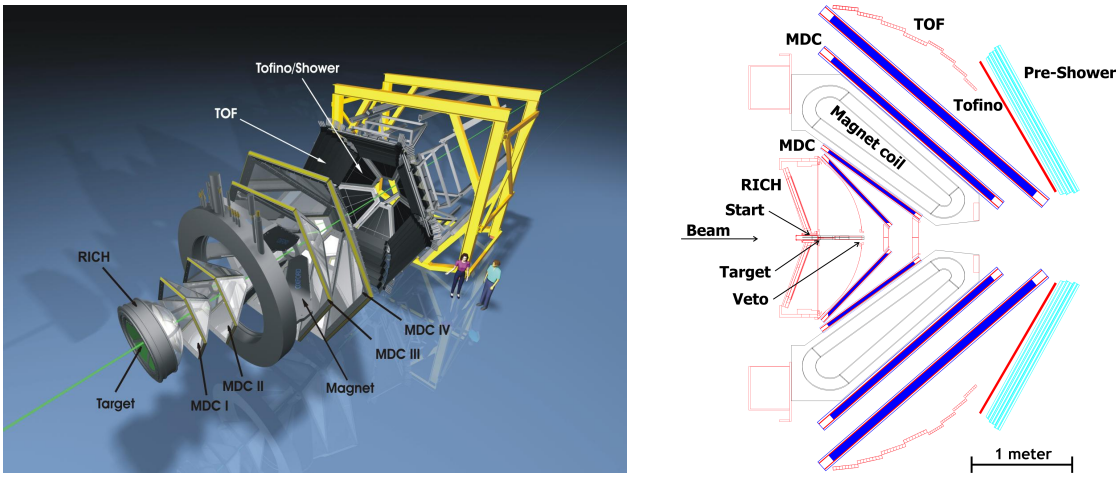

Figure 4.5: Exploded view and cross-section of the HADES spectrometer.

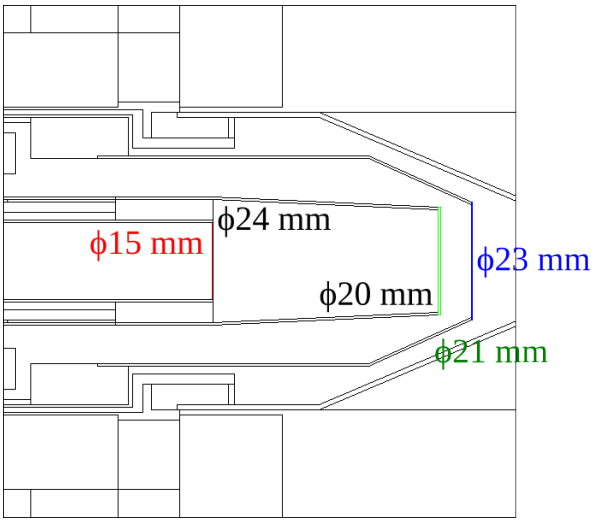

Figure 4.6: Drawing of the liquid hydrogen LH_2 target. Only the vertical arm with the target vessel is shown.

beam flies towards the target inside cylindrical cutoff in the vertical arm. Liquid target is placed in the space between inner cutoff and outer pipe. Target volume on both sides is isolated from the beam vacuum (on the entrance) and atmosphere (on the exit) with kapton windows. Target container has cone-like shape with entrance diameter of $24\,\mathrm{mm}$ (diameter of the inner tube) and $21\,\mathrm{mm}$ on the exit. The inner tube has diameter of $15\,\mathrm{mm}$ and this is also size of the entrance kapton window. Each kapton window has thickness of $100\,\mu\mathrm{m}$. Total length of the active target area is $44\,\mathrm{mm}$.

Hydrogen is cooled down to $20\,\mathrm{K}$ at which, in the atmospheric pressure it has density of $70\,\mathrm{kg\,m^{-3}}$ and interaction probability of $0.7\,\%$. Interaction of the proton in all kapton windows is estimated to $0.012\,\%$.

The target is centered at the beam axis and surrounded by the Ring Imaging Cerenkov (RICH) detector used for electron identification, and employing the Cerenkov effect for the lepton detections. Target is preceded by the fast Start detector, which is a polycrystalline diamond beam detector. The Start detector is used to determine reaction time as a reference for the time of flight detectors, however has not been used in the experiments in 2007. It can be also used as an additional trigger source.

The RICH is further followed by the tracking detector made of four layers of gaseous Multiwire Drift Chambers (MDC) detector. Between the two forward and the two backward MDC stations there is a toroidal superconducting magnet ILSE. The magnetic field bends negatively charged particles in the lower polar angles direction whereas positive particles are bent opposite. Strength of the magnetic field inside the magnet varies between $0.9\,\mathrm{T}$ and $3.6\,\mathrm{T}$. Outside the magnet, in the MDC chamber, the field strength is around $0.8\,\mathrm{T}$.

Momentum of the particle is calculated using approximation of straight particles tracks reconstructed inside MDC layers (with low effective magnetic field), and extrapolation of the curvature of the tracks in well known magnetic field region in the magnet.

For the particle identification, information of reconstructed momentum and the energy deposited in the MDC chambers are used in the analysis. This will be described in the next chapter.

Behind the MDC there are two time of flight (tof) scintillator detectors, TOF and Tofino, covering different polar angle ranges. Together with Start they allow for the precise measurement of the particle's time of flight. However, due to missing the Start detector, this possibility was not used in the analysis. Additionally, the TOF detectors allow also for the position and the energy deposition measurements, and this values optionally can be also used for the tracking and the particle identification using β and momentum observables.

Behind the TOFino detector, there is Pre-Shower detector, built as a chamber containing three layers of led and filled with the gas. Electromagnetic interaction of electrons results in production of electrons showers. The same time, hadrons leave different signature in the detector and can be distinguished from the leptons.

All tree detectors (TOF, TOFino and Pre-Shower) are employed for the event triggering in so called Multiplicity and Electron Trigger Area (META) system, where the trigger decision is made upon charged particles multiplicity measured in all tof detectors.

HADES has two levels of the trigger decision. In the LVL1 trigger, the physical trigger (e.g. multiplicity of particles on the META system) is used. The LVL2 trigger uses additionally RICH information to determine dilepton events. To avoid bias from the LVL2 trigger, the event downscalling (DS), where every third LVL1 event is accepted regardless the LVL2 decision, is used. The final trigger decision is a logical disjunction between the LVL2 and the DS events.

Full description of the spectrometer is presented in [Aga+09].

5 Experimental data

In this work the inclusive production of the Λ hyperon is studied, therefore any reaction $\mathrm{pp} \to \Lambda(\mathrm{p}\pi^-) + X$ is considered. This chapter describes the analysis procedures performed to obtain collection the of reconstructed Λ candidates produced in proton-proton reactions at $\sqrt{s} = 3.17\,\mathrm{GeV}$. The model for hyperon production in the same reaction is presented in Chapter 6. A detailed analysis of the experimental data, simultaneously carried in two independent sets of variables describing the phase-spaces, comparison to production model and final results is presented in Chapter 7. All proton-proton reactions data analyzed in this work were collected in 2007 by the HADES collaboration over 20 days of beam taking. The very last day of beam taking was dedicated to empty target run, used for determining off-target reactions.

5.1 The Lambda reconstruction

The neutral Λ hyperon decays weakly mostly into a pair of a nucleon and a pion (Fig. 5.1). In HADES, it can be reconstructed only by its charged mode of the proton and the negative pion. Both particles must be measured in HADES, and using an invariant mass technique applied to the sum of both daugther particle four-vectors, the mother particle candidate's four-vector is reconstructed. This procedure is performed for each combination of a proton and a pion tracks in the event. Figure 5.2 shows the pre-analysis procedure performed to extract a Λ-hyperon signal, and applicable for both, the model simulations and the experimental data. The procedures described in this section and represented in green color in the figure, are common for both, experimental and simulated

$$
\begin{aligned}
&\mathrm{p} + \mathrm{p} \rightarrow \Lambda + X \\
&\qquad\longrightarrow \mathrm{p} + \pi^- \qquad 63.9 \pm 0.5\,\% \\
&\qquad\longrightarrow \mathrm{n} + \pi^0 \qquad 35.8 \pm 0.5\,\% \\
&\qquad\longrightarrow \mathrm{n} + \gamma \qquad (1.75 \pm 0.15) \times 10^{-3} \\
&\qquad\longrightarrow \mathrm{p} + \pi^- + \gamma \qquad (8.4 \pm 1.4) \times 10^{-4} \\
&\qquad\longrightarrow \mathrm{p} + \mathrm{e}^- + \bar{\nu}_e \qquad (8.32 \pm 0.14) \times 10^{-4} \\
&\qquad\longrightarrow \mathrm{n} + \mu^- + \bar{\nu}_\mu \qquad (1.57 \pm 0.35) \times 10^{-4}
\end{aligned}
$$

Figure 5.1: Λ decay scheme. Numbers on the right are branching rations [Oli+14].

data sets. The red blocks refer only to simulations and will be described in Chapter 6.

Each track is represented by a four-vector, where the value of the momentum is extracted from the track curvature in the magnetic field, and the momentum vector components result from the tracking in the first two layers of the MDC detector, where the track is not yet deflected by the magnetic field. The energy component is obtained from the calculation of the relativistic energy $E = \sqrt{m^2 + p^2}$. The mass m is determined upon particle identification using energy deposition ($\mathrm{d}E/\mathrm{d}x$) in the MDC gas volume as shown in Fig. 5.3. In this figure, the black dashed lines show the selection areas for the particle identification. The preparation of the graphical cuts for both, the experimental data and the model simulations is described in details in [Ber15][1]. The graphical cuts defined for inclusive $\mathrm{pp} \rightarrow \mathrm{K}^0_\mathrm{S} + X$ (K^0_S production is associated with the Λ-hyperon production) analysis are well optimised for the Λ analysis and used in this work. The tracks reconstructions requests that all four hits in the MDC layers must be measured, identified and assigned to a single track. For the analysis of $\Lambda \rightarrow \mathrm{p}\pi^-$ decay, only

[1] Section 2.2.

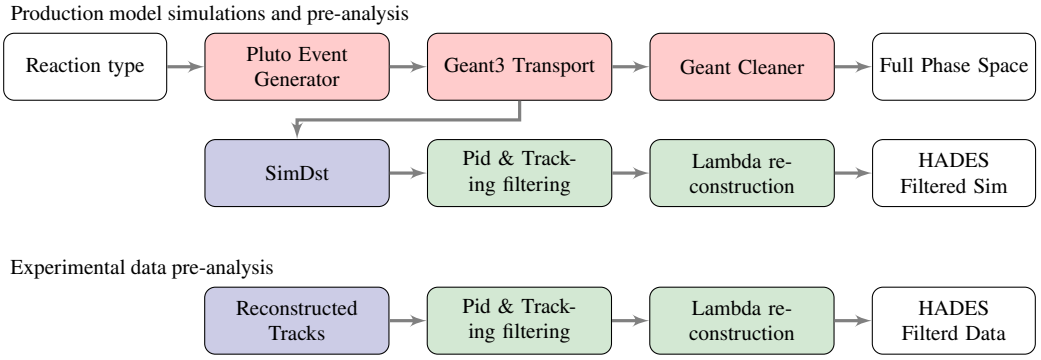

Figure 5.2: Chain of the pre-analysis procedures for single production channel of the production model (upper part) and for the experimental data (lower part).

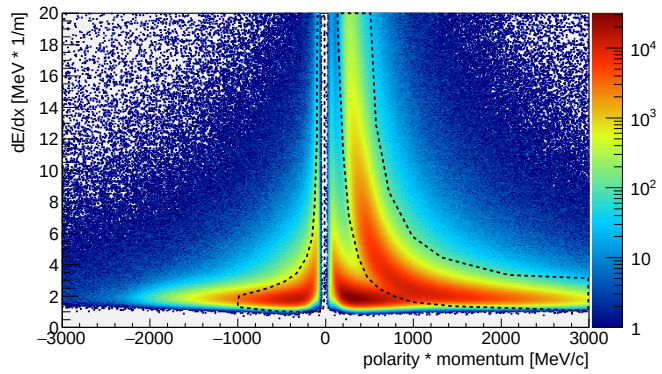

Figure 5.3: Particle identification in the MDC chambers. The red dashed outline depicts selection area.

events in which at least one proton and one pion were identified in the PID procedure are accepted. Among all collected data, 29.8×10^6 events were recognized as good, and further analysed.

The Λ decay point (called a secondary vertex, SV) is found using the point of the closest approach between both decay particles. The track associated to the reconstructed Λ candidate is then extended to the LH_2 target region and intersected with all the other tracks measured in the same event. The position of the primary vertex (PV) is calculated using the center of gravity of all intersecting tracks. Figure 5.4 shows topology of such event.

In the case of a low multiplicity event where no other tracks beside the proton and the pion are available, the primary vertex is calculated by intersecting the Λ candidate track with the beam vector, which is calculated day by day by averaging primary vertices calculated for all higher multiplicity events of that particular beam day. This procedure

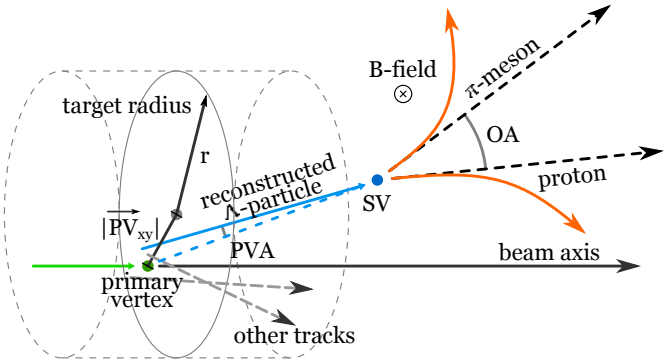

Figure 5.4: Definition of topological cuts used in the analysis. r is the target radius and PV_{xy} is displacement of the primary vertex PV from the target and beam axis in the xy plane. SV is the secondary vertex decay point. PVA is a pointing vector angle, and OA is an opening angle between both decay particles.

is introduced and described in [Ber15][2].

At a center of mass energy of $\sqrt{s} = 3.18\,\mathrm{GeV}$, due to baryon number conservation, only two barions in the final state are possible. Indeed, the energy available in the reaction is not sufficient to produce barion-antybarion pairs. For pions, the multiplicity in the final state is not limited by any quantum number conservation law. Beside the decay of Λ, pions result also from the direct production, the decay of resonances and the decay of various mesons. In the direct production, the available phase-space for a high pion multiplicity events is small, and therefore the fraction of these events in negligible. The high multiplicity of measured protons and pions in a single event leads to significant combinatorial background. Additional misidentification of a positive pion or a Kaon as a proton, and a negative Kaon as a negative pion constitues another source of background.

Since Λ has a limited life time of $c\tau = 78.9\,\mathrm{mm}$, most of the hyperons will decay outside the reaction zone. It is therefore possible to reduce the combinatorial and the misidentification background by applying topological cuts on the reaction (primary vertex) and the Λ decay vertex.

After studies of different variaton of cuts, in the end following set of three topological cuts were applied: *(i)* a z-coordinate of the decay vertex must be larger than the z-coordinate of the primary vertex. This cut allows to reduce the background by factor of two, affecting the signal yield only by around $2\,\%$, *(ii)* a minimum tracks distance (MTD) between the p and the π^- tracks should be smaller than $10\,\mathrm{mm}$, *(iii)* a pointing vector angle (PVA) determined by the spatial vector connecting the primary and the secondary vertex, and the momentum vector of Λ should be smaller than $0.1\,\mathrm{rad}$.

Additional cut on the missing mass (MM) of the $\mathrm{pp} \to \Lambda$ reaction, selecting all the events with $MM(\mathrm{pp} \to \Lambda) > 1400\,\mathrm{MeV/c^2}$ allows to reduce background burther by roughly $20\,\%$. This minimal cuts set is used in the analysis.

Figure 5.5 shows distributions of primary vertices for all the reconstructed Λ candidates after applying all the cuts described above. This picture allows that multiple primary vertices are calculated for a single event and fiiled in the histograms, if the multiple pion or proton tracks are reconstructed for that event.

Even if the target has radius of $10\,\mathrm{mm}$, most of the events are concentrated within the radius of $5\,\mathrm{mm}$. During the data taking, the beam position was moving in vicinity of the centre of the target. In the figure this is shown by several black spots in the center of the target and by the big group of primary vertices south-east from the beam axis.

In the z-direction, the target region can be identified in the range of $-65\,\mathrm{mm}$ to $-18\,\mathrm{mm}$, which corresponds to a realistic target length of $44\,\mathrm{mm}$. Only the events where the reconstructed primary vertex is located within the LH_2 target volume, defined as a tube of $-65\,\mathrm{mm} < z < -15\,\mathrm{mm}$ in the longitudinal coordinate is used for the further analysis steps.

[2] Section 2.3.2.

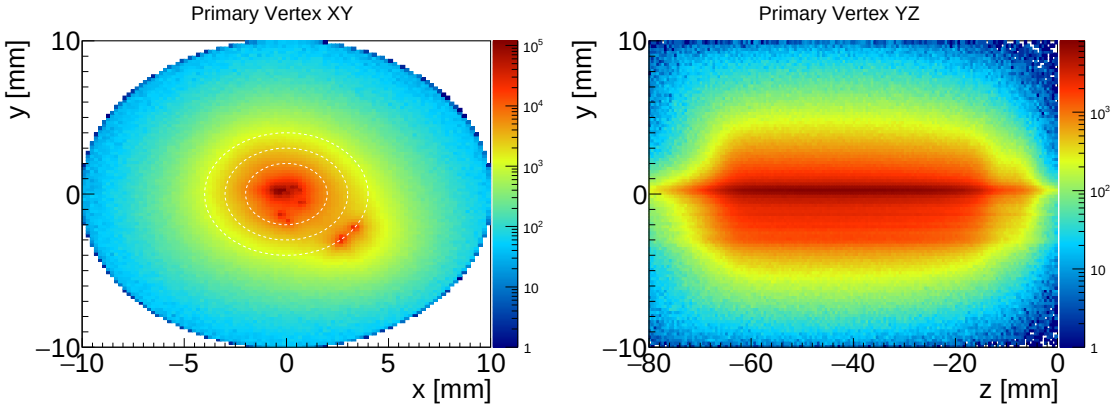

(a) Primary vertex in x-y plane. **(b)** Primary vertex in y-z plane.

Figure 5.5: The primary vertex distribution for all the reconstructed Λ candidates after minimal cut set applied to the data.

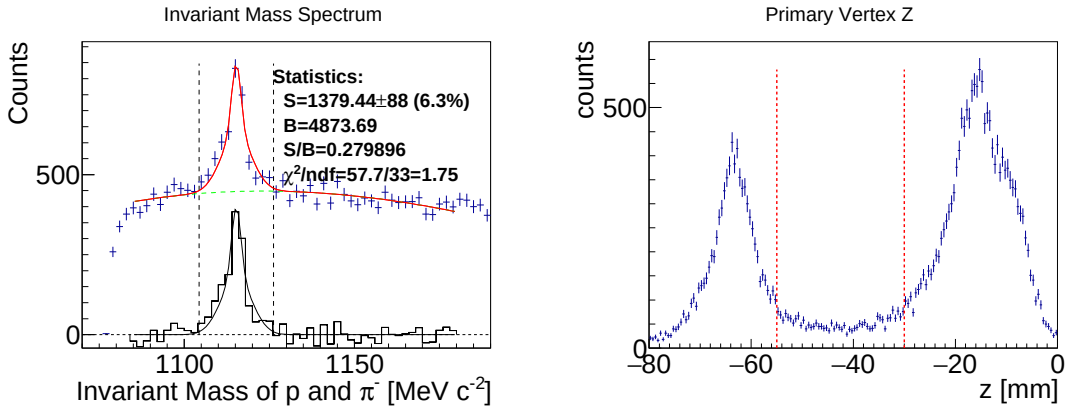

(a) $p\pi^-$ invariant mass. **(b)** Z-vertex reconstruction.

Figure 5.6: Reconstruction of the empty target data sample.

5.2 Empty target data

The analysis of all the events collected during the calibration run without the LH_2 target, the so called empty target run, gives insight into position of the primary vertex of the reactions in the target closing windows. It has reveald that there is a certain contamination stemming from the hyperons production in the Kapton windows on both ends of the LH_2 target.

The chemical composition of the Kapton polyimide is $C_{22}H_{10}N_2O_5$ and mass fractions of each element is listed in Table 5.1. The table shows that the dominating element, according to the mass fraction, is carbon. With a simple toy model assuming a cross-

Table 5.1: Chemical components and its relative mass fractions in Kapton polyimide [NIS15].

Element	Fraction by weight
$^{1}_{1}$H	0.03
$^{12}_{6}$C	0.69
$^{14}_{7}$N	0.07
$^{16}_{8}$O	0.21

section scaling like $Z^{2/3}$, this factor for carbon is ≈ 5 and therefore total strangeness production is at level of $5\,\%$ to $10\,\%$ of the total production in proton-proton reactions.

To study influence of this additional target, analysis of the empty target data was performed parallel to the main analysis, using the same selection criteria and cuts like for the main Λ analysis, except the cut on the z variable. In total, the LVL1 trigger selection recorded 9.5×10^6 events, among which 117×10^3 were recognized as good events for the analysis.

Figure 5.6b shows the reconstructed vertex of the Λ candidates. Clearly, the positions of the peaks are correlated with the Kapton windows locations (Fig. 4.6). The invariant mass spectrum (Fig. 5.6a) shows a clear peak at Λ mass position.

The low statistic of recorded the Λ events prevents performing of full analysis of the parasitic Λ production in Kapton windows. Simulations of such reaction using GiBUU and UrQMD generators show that within the HADES acceptance distributions of produced Λ peaks in the phaspace regions, which are of low statistic in the proton-proton reactions.

Therefore, an additional cut on the primary vertex z-coordinate that reduces the target length by $15\,\mathrm{mm}$ on each side to $-55\,\mathrm{mm} < z < -30\,\mathrm{mm}$ in order to minimize contribution from the off-target reactions was introduced.

5.3 Λ hyperon signal

A number of $(258.2 \pm 1.2) \times 10^3$ Λ hyperons was identified with a signal to background ratio $S/B = 0.47$. Figure 5.7 shows the reconstructed invariant mass. The signal peak was fit with a function being a sum of two normal distributions G having a common mean value μ, a relative contributions r, widths σ_1 and σ_2 and each normalized to one:

$$S = A\left[r \cdot G(x, \mu, \sigma_1) + (1 - r) \cdot G(x, \mu, \sigma_2)\right], \tag{5.1}$$

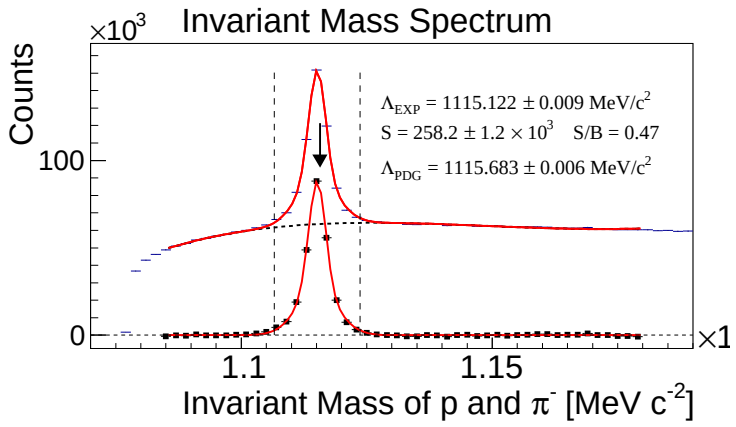

Figure 5.7: Invariant mass of reconstructed Λ signal. The arrow denotes PDG mass position, vertical lines shows integration range for S/B ratio calculation. The solid red curve is the fitted signal and the dashed black line is the fitted background.

where A is the total amplitude of the signal. The quality of the fit is $\chi^2/\mathrm{ndf} = 184.1/33 = 5.58\,(\mathrm{MeV/c^2})^2$.

The background distribution was modelled using the sum of a polynomial of fifth order and an exponential function:

$$B = c_0 + c_1 x + c_2 x^2 + c_3 x^3 + c_4 x^4 + c_5 \exp(c_6 x + c_7), \tag{5.2}$$

where $c_0 \ldots c_7$ are the fit coefficients.

The signal and the signal error come from the fit parameter A and its error. The signal to background ratio was calculated using integrals over the signal and the background fits in a $\mu \pm 3\sigma$ range (dashed lines in the figure), where $\sigma = r\sigma_1 + (1-r)\sigma_2$.

6

Λ hyperon production model

The total Λ production cross-section in proton-proton reactions is evaluated with the help of a simulated production model based on a cocktail of many exclusive reactions. The different channels that compose the cocktail have been simulated via the Pluto event generator [Fro+07].

This model is first used to determine the geometrical acceptance of the spectrometer, and together with the information on the detection efficiency obtained from the HADES analysis framework, is used to determine a correction matrix for the experimental data. In the end, the model is compared with the corrected experimental yields. The quality of comparison strongly depends on the precision with which the model reproduces all contributing channels, including their cross-sections and production anisotropies. Possible deviations of the simulated cocktail to the experimental data are due to missing channels or wrongly estimated cross-sections for the channels included in the cocktail.

The model must consider all the possible and significant Λ production channels. Hyperons can be produced directly, it is so called direct phase-space production, but a Λ hyperon can also result from the decays of a Σ^0 or heavier strange and non-strange resonances (i.g. $\Sigma(1385) \rightarrow \Lambda\pi$, $\mathrm{N}^* \rightarrow \Lambda\mathrm{K}$) . Another possible source of hyperons are the rescattering of the nucleons on strange mesons and exchange of the strange quark ($\mathrm{KN} \rightarrow \Lambda\pi$ process) and $\Sigma^0\mathrm{N} \rightarrow \Lambda\mathrm{N}$ conversion.

In general, all the contribution can be divided into five distinguishable classes, characterized due to the production mechanism:

1. three and four body direct production (e.g. $\mathrm{pK}^+\Lambda$, $\mathrm{pK}^+\Lambda\pi^0$),
2. associated resonance production (e.g. $\Lambda\Delta^{++}\mathrm{K}^0$),

Table 6.1: Reference model for the inclusive Λ production. In the second column, cross-sections obtained from the references in the notes column are listed. The third column shows the variable (in the pp center of mass system), which was used to apply the angular anisotropy. The next two columns show the Legendre polynomial coefficients (see Eq. (6.1)). Column H denotes the channels exclusively measured with HADES.

pp→ reaction	cross-section [μb]	∡ var.	∡(a_2, a_4)		H	notes
		3-body channels				
ΛpK^+	$36.26 \pm 0.43\,^{+3.55}_{-2.83}$	θ^{cms}_{Λ}	0.798	0.134	✓	[Aga+15]
$\Sigma^0 pK^+$	$16.5 \pm 20\,\%$	$\theta^{cms}_{\Sigma^0}$	0.034 ± 0.241	—		[Abd+10]+calc.
$\Lambda\Delta^{++}K^0$	$29.45 \pm 0.08\,^{+1.67}_{-1.46} \pm 2.06$	$\theta^{cms}_{\Delta^{++}}$	1.49 ± 0.3	—	✓	[Aga+14b]
$\Sigma^0\Delta^{++}K^0$	$9.26 \pm 0.05\,^{+1.41}_{-0.31} \pm 0.65$	$\theta^{cms}_{\Delta^{++}}$	0.08 ± 0.02	—	✓	[Aga+14b]
$\Lambda\Delta^{+}K^+$	$9.82 \pm 20\,\%$	$\theta^{cms}_{\Delta^{+}}$	from $\Lambda\Delta^{++}K^0$			res. mod.
$\Sigma^0\Delta^{+}K^+$	$3.27 \pm 20\,\%$	$\theta^{cms}_{\Delta^{+}}$	from $\Sigma^0\Delta^{++}K^0$			res. mod.
$\Sigma(1385)^+nK^+$	$22.42 \pm 0.99 \pm 1.57\,^{+3.04}_{-2.23}$	$\theta^{cms}_{\Sigma^{+*}}$	1.427 ± 0.3	0.407 ± 0.108	✓	[Aga+12]
$\Delta(2050)^{++}n$	33 % feeding for Σ^*nK^+	θ^{cms}_{n}	1.27	0.35	✓	[Aga+12]
$\Sigma(1385)^+pK^0$	$14.05 \pm 0.05\,^{+1.79}_{-2.14} \pm 1.00$	$\theta^{cms}_{\Sigma^{+*}}$	1.42 ± 0.3	—	✓	[Aga+14b]
$\Sigma(1385)^0pK^+$	$6.0 \pm 0.48\,^{+1.94}_{-1.06}$	$\theta^{cms}_{\Sigma^{0*}}$	from $\Sigma(1385)^+nK^+$		✓	[Aga+12]
$\Lambda(1405)pK^+$	$9.2 \pm 0.9 \pm 0.7\,^{+3.3}_{-1.0}$	—	—	—	✓	[Aga+13]
$\Lambda(1520)pK^+$	$5.6 \pm 1.1 \pm 0.4\,^{+1.1}_{-1.6}$	—	—	—	✓	[Aga+13]
$\Delta^{++}\Lambda(1405)K^0$	$5.000 \pm 20\,\%$	—	—	—		[Aga+14c]
$\Delta^{++}\Sigma(1385)^0K^0$	$3.500 \pm 20\,\%$	—	—	—		[Aga+14c]
$\Delta^{+}\Sigma(1385)^+K^0$	$2.300 \pm 20\,\%$	—	—	—		[Aga+14c]
$\Delta^{+}\Lambda(1405)K^+$	$2.300 \pm 20\,\%$	—	—	—		compl. to above
$\Delta^{+}\Sigma(1385)^0K^+$	$2.300 \pm 20\,\%$	—	—	—		compl. to above
		4-body channels				
$\Lambda p\pi^+K^0$	$2.98 \pm 0.02\,^{+0.21}_{-1.98} \pm 0.18$		—		✓	[Aga+14b]
$\Lambda n\pi^+K^+$	from $\Lambda p\pi^+K^0$		—			
$\Lambda p\pi^0K^+$	from $\Lambda p\pi^+K^0$		—			
$\Sigma^0 p\pi^+K^0$	$1.34 \pm 0.02\,^{+0.10}_{-1.35} \pm 0.09$		—		✓	[Aga+14b]
$\Sigma^0 n\pi^+K^+$	from $\Sigma^0 p\pi^+K^0$		—			
$\Sigma^0 p\pi^0K^+$	from $\Sigma^0 p\pi^+K^0$		—			

3. intermediate resonance production (e.g. $\Lambda(1405)pK^+$),
4. double resonances production (e.g. $\Delta^{++}\Lambda(1405)K^0$),
5. five or more body phase-space direct production.

For simplicity, in this classification, both lightest hyperons, Λ and Σ^0 are considered as the final particles in the decay chain, neglecting the fact that Σ^0 decays further into $\Lambda\gamma$ pair. All the classes mentioned above are described in the following subsections. The

full list of the contributions from the first four classess is presented in Table 6.1. Due to negligible contributions from the fifth class, these channels were not considered in the final model.

Each channel is characterized by a differential cross-section $\sigma(x)$, containing the total production cross-section σ_0 term and the possible angular dependencies in terms of the coefficients a_0, a_2, a_4 of Legendre polynomials sum, describing the anisotropy of the channel production. The total differential cross-section including the anisotropy is expressed in the form:

$$\sigma(x) = \sigma_0 \cdot \frac{1}{2}\Big\{a_0 P_0(x) + a_2 P_2(x) + a_4 P_4(x)\Big\}, \tag{6.1}$$

where $x \equiv \cos(\theta_{\text{cms}})$ with θ_{cms} being a polar angle of the leading particle in the pp reference frame, and P_0 to P_4 are Legendre polynomials:

$$P_0(x) = 1, \quad P_2(x) = \frac{1}{2}(3x^2 - 1), \quad P_4(x) = \frac{1}{8}(35x^4 - 30x^2 + 3). \tag{6.2}$$

The leading particle for each channel is specified in the third column of Table 6.1. In this analysis, the coefficient a_0 is always set to 1.0 as its mathematical meaning is the scaling factor for P_0, and we request that the integral of the Legendre polynomials over all angles normalizes to one:

$$\frac{1}{2}\int_{-1}^{+1} \mathrm{d}x a_0 P_0(x) + a_2 P_2(x) + a_4 P_4(x) = 1. \tag{6.3}$$

In such a case, the cross-section value is equal to the scaling factor. In the proton-proton center of mass reference frame, a symmetric particle production is assumed and therefore assymetric odd-order polynomials are ignored. Three first even terms are sufficient to describe the anisotropies.

Among all the channels, those with tics in column H in Table 6.1 denote channels measured by HADES in the same system of pp reaction as showed in this analysis. For the other channels, either assumption from the isospin relations [TST97; Tsu+99], or predictions from GiBUU transport models [Bus+12] are used.

The production model estimates Λ production with cross-section of $160.6\ ^{+7.7}_{-8.2}\ \mu\mathrm{b}$.

Direct phase space production

Partial Wave Analysis (PWA) of the $\mathrm{pp} \rightarrow \Lambda\mathrm{pK}^+$ reaction at HADES [Aga+15] revealed that beside a $20\,\%$ contribution of pure phase space, the production of $\Lambda\mathrm{pK}^+$ is dominated by the N^* resonances. The PWA technique, using the event-by-event fit of reconstructed signals allowed to determine the contribution of each transition in the final spectrum. The total cross-section was calculated using the normalization of the model

to the normalized experimental data. The angular distribution is exclusively driven by contributing partial waves, and values given in the table are the results of a Legendre polynomials fit. The simulation sample used in this analysis contains combination of PWA driven events and pure phase space events.

The reaction of $\mathrm{pp} \to \Sigma^0\mathrm{pK}^+$ was never measured at HADES due to missing possibility to detect γs from Σ^0 decays. There are no other measurements at the HADES energies, and the closests results come from COSY-TOF experiment at $\sqrt{s} \approx 2.7\,\mathrm{GeV}$ [Abd+10]. Since Σ^0 has the identical quark content like Λ, first approximation of the cross-section ratio can be based on the isospin relation only and is equal to three. However it was showed that this ratio decreases with the excess energies ϵ and saturates at 2.2 for $\epsilon > 700\,\mathrm{MeV}$ [Abd+10]. This limit was used to estimate the cross-section at the HADES energy from $\mathrm{pK}^+\Lambda$ analysis by dividing the $\mathrm{pK}^+\Lambda$ cross-section by factor 2.2. For such obtained cross-section, an uncertainty of $20\,\%$ was assumed. Due to small mass difference between Σ^0 and Λ, the latter one will follow the direction of flight of its mother particle, and anisotropy of Λ production in this channel was taken from COSY data for Σ^0. It is however possible that the anisotropy of the Σ^0 at the HADES energies differes from those in the COSY results.

Associated resonances production

Channels with the associated Δ^{++} resonance production were studied in HADES in the exclusive K^0 analysis [Aga+14b]. However, there are no published results on the Δ^+ channels. The resonance model [TST97; Tsu+99] predicts, following again the isospin relation, that the cross-section ratio is $\sigma(\mathrm{pp} \to \mathrm{Y}\Delta^{++}\mathrm{K}^0)/\sigma(\mathrm{pp} \to \mathrm{Y}\Delta^{+}\mathrm{K}^+) = 3$, and this scaling factor was used to obtain $\mathrm{Y}\Delta^{+}\mathrm{K}^+$ cross-sections from respective $\mathrm{Y}\Delta^{++}\mathrm{K}^0$ reaction. The cross-section error was assumed to be $20\,\%$. Angular coefficients were likewise assumed to be equal to those from respective Δ^{++} channels.

Intermediate resonances production

In the intermediate strange resonance sector, three independent analyses were performed. In the $\Sigma(1385)^+\mathrm{nK}^+$ production analysis [Aga+12], it was shown that beside the direct production, additional feeeding on the level of $33\,\%$ comes from $\Delta(2050)^{++}\mathrm{n}$ channel. Therefore the total cross-section of $22.42\,\mu\mathrm{b}$ was split between these two channels with relative contributions of $67\,\%$ and $33\,\%$ respectively. Both contributions are also characterized by different angular distributions.

Very similar anisotropy was found for the $\Sigma(1385)^+\mathrm{pK}^0$ production channel [Aga+14b], though only the a_2 term was calculated. Since no measurement of the anisotropy coefficients is available for the channel $\Sigma(1385)^0\mathrm{pK}^+$ [Aga+12], aniostropy measured for the $\Sigma(1385)^+\mathrm{pK}^0$ channel was used.

Channels with $\Lambda(1405)$ and $\Lambda(1520)$ [Aga+13] did not show any significant anisotropy and therefore are simulated as flat in the phase-space.

Many-resonances channels

Channels with mixed associated and intermediate resonances have not been measured at HADES at all, there are also no predictions for them in the resonance model, which does not consider strange resonances. However, analysis of the inclusive K^0 production in proton-proton and proton-Niobium reactions at HADES [Aga+14c] are clearly showing that the first three channels from this group, namely $\Delta^{++}\Lambda(1405)\mathrm{K}^0$, $\Delta^{++}\Sigma(1385)^0\mathrm{K}^0$ and $\Delta^{+}\Sigma(1385)^+\mathrm{K}^0$ are necessary to describe the K^0_S differential distributions, and this analysis also constrained cross-sections of these channels but without any further errors estimations. Therefore, an arbitrary error of $20\,\%$ was assumed for all of these three channels. The two next channels, $\Delta^{+}\Lambda(1405)\mathrm{K}^+$ and $\Delta^{+}\Sigma(1385)^0\mathrm{K}^+$ are introduced in this model as complementary to the $\Delta^{+}\Sigma(1385)^+\mathrm{K}^0$ channel, and have the same cross-section and errors. All thess five channels are considered to be produced flat in the phase-space.

Four body channels and higher order of particle multiplicity

Among all the six variations of the four-body direct phase-space production $\mathrm{YKN}\pi$ channels, only the neutral Kaon production branches were analyzed in HADES, namely $\Lambda\mathrm{p}\pi^+\mathrm{K}^0$ and $\Sigma^0\mathrm{p}\pi^+\mathrm{K}^0$ [Aga+14b]. These channels are complementary to the resonance production via $\Lambda\Delta^{++}\mathrm{K}^0$ and $\Sigma^0\Delta^{++}\mathrm{K}^0$ and represents the same final state particles like decay of the resonant channel. But in contrast to the resonant contribution, these four body channels contain no anisotropy.

When considering other four channels, we can make assumptions on their production, by considering their similarity to the first two branches. The production threshold for neutral Kaons branch is only $9\,\mathrm{MeV}$ higher than the one for the lightest sibling in charged Kaon branch. This can be explained as a swap of u and d quarks between the pion and the Kaon in the final state particles. This justifies the assumption that the phase-space distribution and production cross-sections should be approximately the same for each of the Λ or Σ^0 four body families. Therefore cross-section for the channel containing K^0_S where used for the isospin partner channels containing charged kaons.

All the other, higher body order channel have such small cross-section ($< 1\,\mu\mathrm{b}$, that they can be neglected in the analysis. There are very sparse data available for a few of these channels, but all measurements at higher energies of $8\,\mathrm{GeV}$ to $30\,\mathrm{GeV}$, and their cross-sections at the HADES energy can only be estimated from the phase-space parametrization, which is very inaccurate when extrapolating to the lower energy ranges.

6.1 Model preparation

Each channel of the production model is prepared separately, and each follow exactly the same simulations and pre-analysis procedures, both described below, and showed in Fig. 5.2 by the red blocks. All the channels at this step are produced and simulated without any embedded anisotropy, which is applied on the final step while preparing the total model as described in Chapter 7.

6.1.1 Pluto event generator

In the first step of the preparation, events for each channel are generated by using the Pluto event generator, and each channel is simulated with the statistics of 20×10^6 events.

Pluto is a Monte Carlo based event generator designed for the study of hadronic interactions in the SIS18 and FAIR energy regime. It is highly customizable tool, allowing also for defining custom particles and resonances, and characterize them by mass, width and decay branches. Resonances are calculated using relativistic mass-dependent Breit-Wigner sampling. In the heavy ions regime, Pluto incorporates the thermal model for calculation of particles yields. Beside a few particular cases, Pluto simulates the production of many body reactions isotropicaly, but allows also for defining anisotropy of the particular channels. However, this possibility is not used in this work.

On the input, the event generator is feed with the parameters describing the beam and target particles, the kinetic beam energy $T_{\mathrm{kin}} = 3.5\,\mathrm{GeV}$ and the definition of requested reaction. The output of the event generator depends on the particles involved in the reaction. Λ and Σ^0 hyperons are always preserved in the event in the final state, but all the resonances and strange resonances are always decayed to their daugther paticles accordingly to the branching ratios. Though strange resonances have also branchings which do not decay into neither Λ or Σ^0, these branchings are all available in the event generator output, though are discarded in the further analysis steps.

For the channels, where the leading particle was different than Λ or Σ^0, it mostly concerns $\Sigma(1385)$ and Δ resonances, the leading particle was reconstructed directly from the Pluto output using the decay particles, and cosinus of the azimuthal angle in the pp center of mass reference frame of the leading particle was calculated and assigned as a fake weight of the event, used later to apply channel anisotropy.

6.1.2 Geant3 transport

In the second stage, propagation, scattering and the decay of the particles is calculated using the Geant3 transport tool working inside the HADES hgeant framework. In this framework, the whole target and detector geometry are implemented. The reaction event is randomly distributed inside the active target area. Since the reaction probability is

on order of $1\,\%$, a homogeneous distribution along the z-axis direction is justified. In the radial direction, the gaussian profile was used to reproduce beam shape. From the random origin of the event in the target volume, particles are further propagated through all the defined detector volumes. All material effects like particle scattering and energy looses in the detector volumes are considered in this process.

At this step, the Σ^0 and Λ decays are also calculated. All the tracks, for both stable and unstable particles are stored in the output. It allows for full reconstruction of the reactions chain and allows to iterate over all the tracks to find all the initial Λs, determine whether they are primary (direct particles from the event) or secondary (decayed or rescattered) particles. Tracks are also tagged with the flag determining whether particles were passing through the detector volume and therefore should be included in the determination of the geometrical acceptance.

In the Geant Cleaner tool, all Λ tracks (with no consideration of the geometrical acceptance) are extracted from the collection of all tracks and written to the file containing full 4π phase-space distribution.

6.1.3 Realistic detector response and particle identification

Output of the Geant feeds the SimDst tool, in which the ideal hits of all the trackins in the detectors volumes are interpreted with simulated detectors responses. For such detector responses, assumed to be realistic, tool simualtes the detectors response to the tracks and determines, whether within the detection efficiency, track was properly registered by the detector. If the whole event fulfills the LVL1 trigger conditions, especially trigger multiplicity used in the experiment, the event is accepted and written to the output, otherwise is discarded.

The particle identification of the simulated channels works in the same way like the one for the experimental data, but cuts had to be adjusted for slightly different shapes of Bethe-Bloch distributions. Differences in the shape come from different reproduction of the detector behavior in the simulation with respect to the real device. Adjusting of the cuts means here that for given interval of the particle momentum, identification should has the same efficiency for identyfiing particles in both experimental and simulation samples. Full procedure of the preapration and adjusting of these cuts is described in [Ber15][1].

Further steps of the Λ reconstruction are exactly the same like for the experimental data. Each p-π^- pair is combined for Λ signal, and topological cuts, the same like for experimental data, are applied. This sample of simulated events in then so called a filtered data set, where *filtered* relates to the HADES acceptance and efficiency selection of the events.

[1] Section 2.2.

6.2 Model normalization and finalization

Each channel is normalized to its production cross-section using the following expression:

$$s_i = \frac{S_i \times \sigma_i}{N_i \times 10^6}, \tag{6.4}$$

where S_i is a simulated sample, N_i is a number of simulated events, σ_i is a cross-section value taken from Table 6.1 expressed in units of $\mu\mathrm{b}$ and s_i represents normalized distribution. The integral of s_i over the whole sample results in a total cross-section value.

The sum over all i samples (model channels) gives Λ production distribution in 4π phase-space predicted by the model. The same procedure is performed for the HADES filtered data, resulting with a distribution obtained under simulated efficiency and acceptances of the HADES spectrometer.

7
Data analysis

A total yield of 258.2×10^3 Λ hyperons found in the experimental data sample after applying the acceptance and efficiency corrections and the normalisation factor translates to approximately $208\,\mu\mathrm{b}$ of production cross-section. All this steps of the analysis are described in further parts of this chapter. This brief estimation is calculated using the whole Λ spectrum over all available phase-space.

This approach however does not give any insight into dynamics and kinematics of the hyperon production in various contributing channels, especially the spatial and the momentum distributions of outcoming Λs are unknown. Anisotropy in the production is mainly related to the resonance production mechanics, while the phase space production is flat.

The Λ candidates reconstructed from the experimental data have been therefore analysed using a double differential analysis approach for a pairs of two independent variables: the total momentum and the polar angle, both expressed in the center of mass frame of the pp reaction. The reaction is symmetric in the azimuthal coordinate. For completeness also a transverse momentum p_{t} as a function of rapidity y^{cms} was analysed in parallel[1]. The first analysis allows to extract cross-sections as a function of the polar angle $\sigma(\cos\theta)$, second as a function of rapidity $\sigma(y)$. Since both analyses use the same input data set, the obtained results should be consistent and comparable, and therefore this represents a self-consistency test of the analysis procedures.

First, the procedure of extracting the signal yields in the experimental differential

[1]Transverse momentum is defined as $p_t = \sqrt{p_x^2 + p_y^2}$ and rapidity as $y = {}^1\!/_2 \ln({}^{E+p_z c}\!/_{E-p_z c})$, where E, p_x, p_y and p_z are the four-vector components.

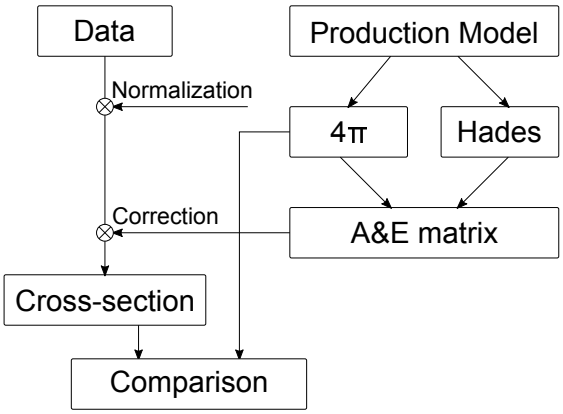

Figure 7.1: Flow of the data analysis.

distributions will be presented. In the next step, the procedure of data correction using the simulations based on the production model introduced in Chapter 6 will be described in details. The experimental differential yields after corrections and normalisation will be compared directly to this model. The flow of the analysis is presented in Fig. 7.1.

The processing the pre-analysis of the experimental data (Section 5.1) and of the production model (Section 6.1) leads to unified representation of both sets of data and they are further analysed using the same set of tools.

7.1 Differential distributions of the experimental yields

Figure 7.2 shows the double differential distributions for both analyzed distributions of the uncorrected Λ candidates. The phase-space was defined with a fine binning, representing a good approximation of a continuous distribution. In fact, the distributions includes both, the real Λ signal and the combinatorics and misidentified background. In these figures, both phase-spaces were filled with the measured yield on the corresponding invariant mass distribution selected in the range of $1102\,\mathrm{MeV/c^2}$ to $1130\,\mathrm{MeV/c^2}$ which is $14\,\mathrm{MeV/c^2}$ around the Λ nominal mass. Signal to background ratio S/B in these figures integrated over the whole phase-space is equal to 0.5 extracted from the invariant mass fit. Subtraction of the background is performed in the further step of the analysis.

The experimental distributions can be however compared to the simulated model distribution, presented in Fig. 7.3. The upper row represents the simulation sample which is filtered by the HADES acceptance and therefore should be similiar to the distributions obtained from the experimental data. The lower two figures show the initial distributions in the whole 4π phase-space. The procedure to obtain this distribution will be described in the next section.

It is not possible to distinguish the real Λ candidates from the background and determine its corresponding phase-space element on event by event base. It can be only done

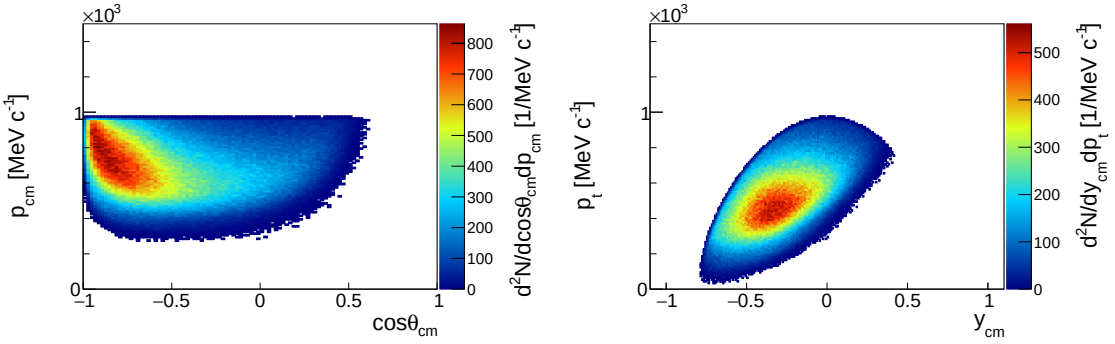

(a) p^{cms}-cos θ^{cms} distribution. **(b)** p_{t}-y^{cms} distribution.

Figure 7.2: Phase space distribution of reconstructed Λ signal for both analyses.

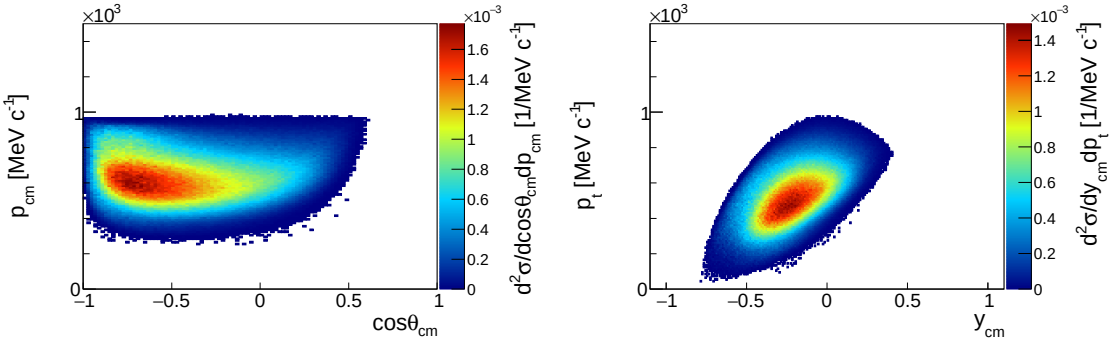

(a) p^{cms}-cos θ^{cms} in HADES acceptance. **(b)** p_{t}-y^{cms} in HADES acceptance.

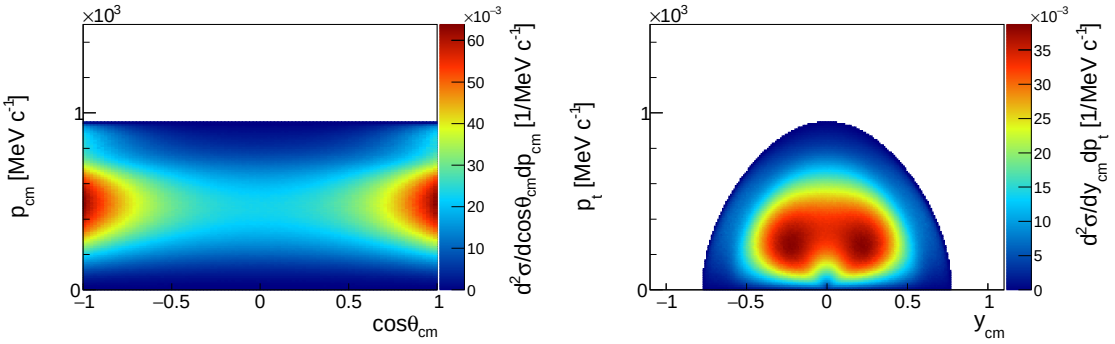

(c) p^{cms}-cos θ^{cms} in 4π. **(d)** p_{t}-y^{cms} in 4π.

Figure 7.3: Phase space distribution of the full Λ cocktail for both analyses.

by the analysis of the statistical sample in finite, discrete phase-space elements.

For each phase-space element ΔY, ΔX, where X, Y are the two independent variables, one can repeat the fitting procedure of the invariant mass peak (Eq. (5.1)). Since

such fit cannot be done in an infinitely small phase-space volumes, the limitation here is the size of the phase-space element which relates to the statistic of the signals inside it.

The phase-space was discretized with equally sized bins of $0.2 \times 100\,\mathrm{MeV/c}$ bins in p^{cms}-$\cos\theta^{\mathrm{cms}}$ and $0.2 \times 75\,\mathrm{MeV/c}$ in p_{t}-y^{cms} distributions. The discrete binning is shown in Fig. 7.4. The upper limit for the Λ momentum in a proton-proton rest frame is $942\,\mathrm{MeV/c}$. The discretised phase-space was therefore limited to $1000\,\mathrm{MeV/c}$ and -1.0 to 0.6 of $\cos\theta^{\mathrm{cms}}$ for the first analysis and to $975\,\mathrm{MeV/c}$ and -0.8 to 0.4 in rapidity for the second. The right side boundaries of the p^{cms}-$\cos\theta^{\mathrm{cms}}$ and p_{t}-y^{cms} distributions are determined by the HADES acceptance. The Λ production goes into the full 4π solid angle which translates to the rapidity range of -0.77 to 0.77 at the HADES energy.

Each discrete bin has its own invariant mass histogram, filled with the mass of the Λ candidate belonging to the phase-space discrete bin. After all the events are analysed and respective discrete bins histograms are filled, the invariant mass peak is fit for each of the invariant mass histograms. For each of the fits, signal yield and yield error normalized to bin width are extracted. The final result of the signal yield finding is shown in Fig. 7.4. These results represent Λ production filtered by detector geometrical acceptance and detection efficiency. Detailed results of all the fits are presented in Appendix A.

7.2 Differential analysis of the production model

The pre-analysed simulations described in Section 6.1 are processed in a similar way like presented in the previous section for the experimental data. Small differences in the procedures emerge from the need of applying weights of the angular distribution to the analysed simulation channels. This procedure is applied for both 4π and filtered (from now on called fss, full-scale simulation) simulation phase-space samples.

The phase-space distributions of the weighted events of all the simulation channels are shown in Fig. 7.3. For the simulations of the 4π distributions clear kinematical limits of the Λ production at $942\,\mathrm{MeV/c}$ momentum are visible. In the fss distributions these edges are smeared due to the limited spectrometer resolution in the momentum and the position determination.

Both 4π and fss simulation samples of each channel are analysed in the same differential boundaries like the experimental data. Each event is weighted with the coefficient calculated from Eq. (6.1) for the θ angle of the Λ direction, and discrete invariant mass histograms are filled with the weighted data. All discrete invariant mass histograms are normalized as described in Section 6.2 and added coherently. For the 4π spectra, since it is a simulation with a well know Λ mass and no invariant mass peak fitting is required, the number of Λ candidates is taken directly from the bin content. For the fss sample, a fit of each bin with the formula shown in Eq. (5.1) is performed and the signal is extracted from the fit in the same way like for experimental data.

Now, by dividing the total signal yield in fss analysis by the signal from the 4π

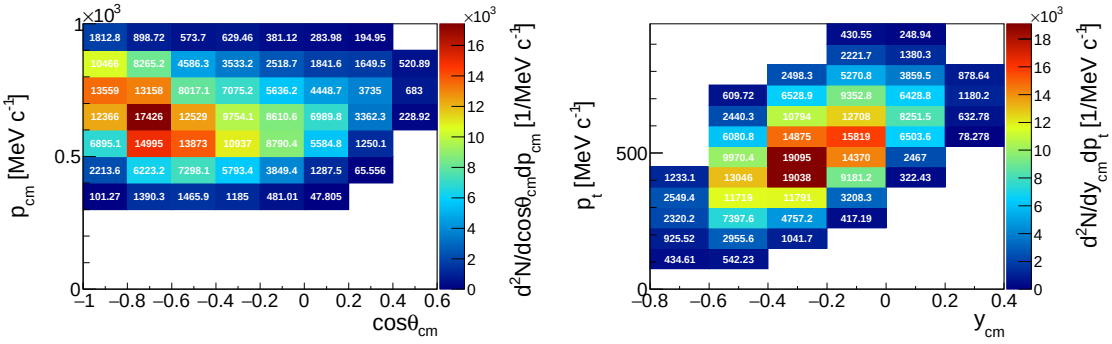

(a) p^{cms}-$\cos\theta^{\mathrm{cms}}$ distribution. **(b)** p_{t}-y^{cms} distribution.

Figure 7.4: Differential distribution of the Λ signal.

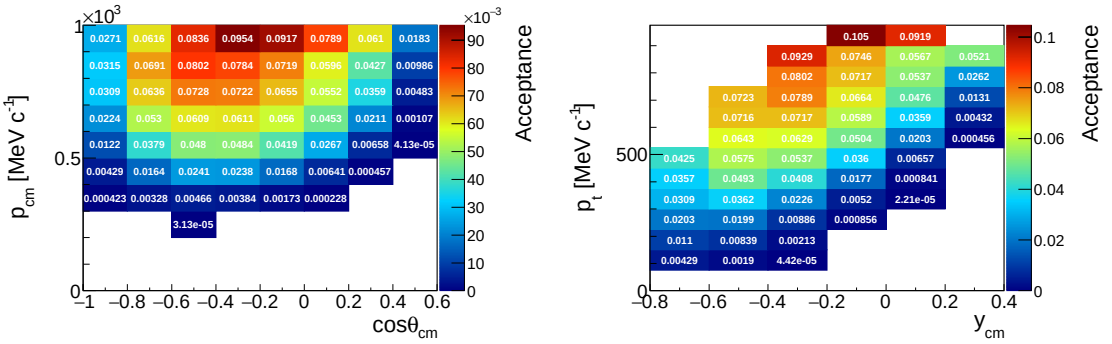

(a) p^{cms}-$\cos\theta^{\mathrm{cms}}$ distribution. **(b)** p_{t}-y^{cms} distribution.

Figure 7.5: Acceptance and efficiency correction matrices.

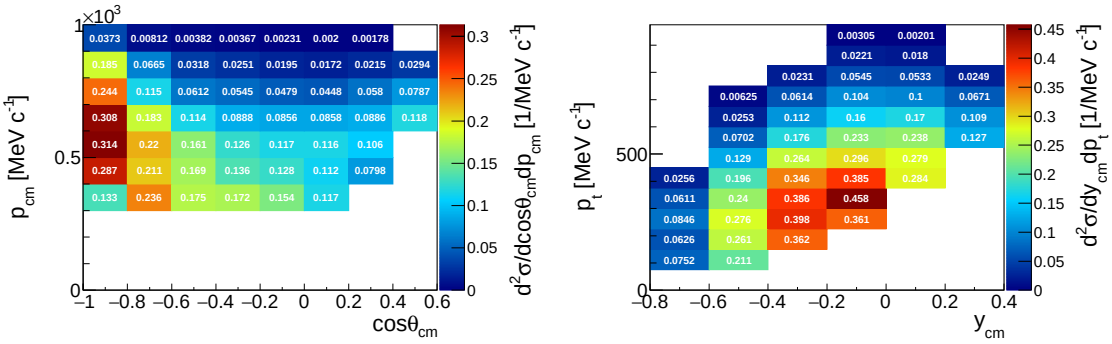

(a) p^{cms}-$\cos\theta^{\mathrm{cms}}$ distribution. **(b)** p_{t}-y^{cms} distribution.

Figure 7.6: Corrected and normalized double differential experimental yields.

analysis, one obtains acceptance and efficiency correction matrices applicable for the experimental data (Fig. 7.5). At the same time, the total signal yield of the 4π analysis

represents the total production model, which can be compared with the experimental data.

7.3 Corrections and normalisation

To transform the experimental data from double differential counts distributions domain to the cross-section domain, an absolute normalisation of the data must be applied.

The normalization factor is calculated in [RC10] by comparing the elastic cross-section $\sigma^{\mathrm{el}}_{4\pi}$ of the pp reactions in the 4π phase-spaced and the cross-section in the HADES acceptance $\sigma^{\mathrm{el}}_{\mathrm{acc}}$, to the number of recorded events of the elastic pp collisions N^{el}_{acc}:

$$\sigma^{\mathrm{el}}_{4\pi} = \sigma^{\mathrm{el}}_{\mathrm{acc}} \frac{N^{\mathrm{el}}_{4\pi}}{N^{\mathrm{el}}_{\mathrm{acc}}}. \tag{7.1}$$

The normalization adds an additional statistical error of $2\,\%$ and a systematical of $7\,\%$.

Acceptance and efficiency corrections are applied by dividing the normalized distributions of the experimental data from Fig. 7.4 by the acceptance correction matrices from Fig. 7.5. The results of this operation are shown in Fig. 7.6.

From the nature of pp reaction, for the distributions in the reaction centre of mass system, one would expect a symmetry of the distributions around the axis perpendicular to the beam axis at the point of $\cos(\theta_{\mathrm{cms}}) = 0$ or $y_{\mathrm{cms}} = 0$ respectively.

From the plots presented in Fig. 7.6, one can conclude that this symmetry is in general preserved in the obtained distributions. Divergences are observed in the bins on the edgeds of the detector acceptance. One possible explanations is that the reproduction of all effects introduced by the acceptance filtering (detectors efficiency, geometrical acceptance, alignment, tracking feasibility) might not be perfectly reproduced in the simulations. From the other side, such bins have also lower statistics of the signal and the fit results are subjected to the higher uncertanities.

7.4 Systematic and statistical uncertainties

Systematic uncertainties in the analysis are evaluated at the different stages of the analysis.

In the first step, the influence of the cuts used to purify the Λ sample is considered. Two new analysis sets, each containing initial experimental data and simulation channels were created. In each of the sets, all cuts used for Λ selection were modified by $20\,\%$ in sucha to apply more or less stringent selection cut for the Λ candidates. See cuts description on Page 76 and in Table 7.1.

Table 7.1: Summary of cuts variation for the Minimum Tracks Distance (MTD), the Pointing Vector Angle (PVA) and the Missing Mass (MM) variables.

Cut variant	MTD	PVA	MM
Regular cuts	$< 10\,\mathrm{mm}$	$< 0.10\,\mathrm{rad}$	$> 1400\,\mathrm{MeV/c^2}$
Loose cuts	$< 12\,\mathrm{mm}$	$< 0.12\,\mathrm{rad}$	$> 1260\,\mathrm{MeV/c^2}$
Strict cuts	$<\ \ 8\,\mathrm{mm}$	$< 0.08\,\mathrm{rad}$	$> 1540\,\mathrm{MeV/c^2}$

In each of these new analysis sets, all steps of the analysis described in the previous parts were executed. The reconstruction of the Λ signal and the differential analysis were performed, and new the acceptance and the correction matrices were obtained. In the end, all experimental data were corrected with these new matrices.

The corrected experimental yields were compared to the reference data set, and maximal variation in each differential bin was calculated.

Second systematic uncertainty evaluation tested sensitivity of the acceptance matrix to the model parameters. The production model was varied by sampling the cross-section and angular distribution in each contributing channel according to a Gaussian probability density with the width equal to the corresponding error. This procedure was repeated in 1000 iterations, in which each channel was sampled independently and for each iteration a new correction matrix was evaluated. In the end, each differential bin was characterized by the average correction value and RMS value of the mean value. The systematic error

Table 7.2: Summary of systematic uncertainties evaluation.

Uncertainty source	p^{cms}-$\cos\theta^{\mathrm{cms}}$ analysis	p_{t}-y^{cms} analysis
Uncorrelated errors (1)		
Topological cuts variation	$^{+6.2}_{-7.9}\ \%$	$^{+4.2}_{-4.9}\ \%$
Acceptance matrix sampling	$1.2\,\%$	$1.2\,\%$
Correlated errors (2)		
Normalisation stat.	$2\,\%$	$2\,\%$
Normalisation syst.	$7\,\%$	$7\,\%$
Total error (1)+(2)	$^{+6.3}_{-8.0}\ \% \pm 7.3\,\%$	$^{+4.4}_{-5.1}\ \% \pm 7.3\,\%$

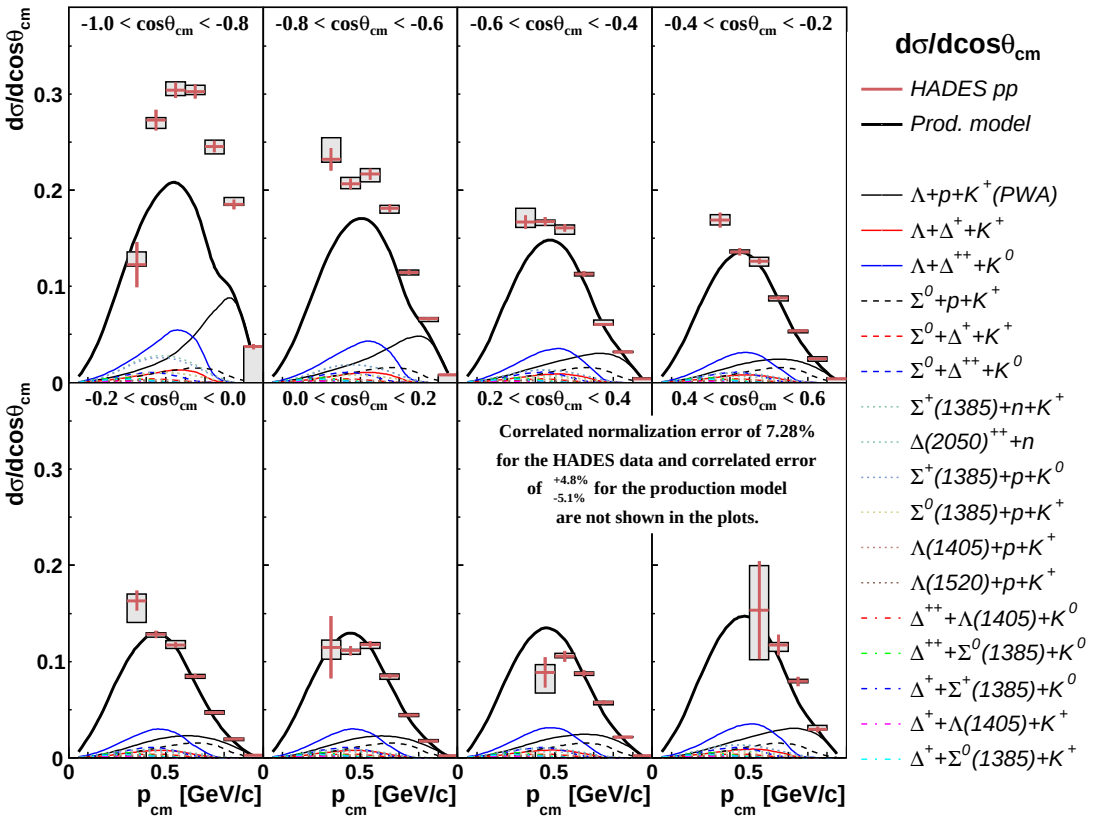

Figure 7.7: Differential comparison of corrected experimental data to the production model in the p^{cms}-$\cos\theta^{\mathrm{cms}}$ phase-space. Error bars of the HADES data do not include correlated errors of 7.3 %.

for this bin was further calculated using the following formula:

$$\delta_{i,j} = \sigma_{i,j} \cdot \frac{A^{\mathrm{RMS}}_{i,j}}{A_{i,j}}, \tag{7.2}$$

where i and j enumerate the differential bin, $\sigma_{i,j}$ is a differential cross-section for the bin, $A^{\mathrm{RMS}}_{i,j}$ is a RMS value of the iterated correction matrix and $A_{i,j}$ is the reference matrix.

A systematic uncertainty of 7 % and statistical uncertainty of 2 % from normalisation factor were considered. In the end, all uncertainties were added quadraticly for each differential bin. Result of systematic uncertainties evaluation are summarizied in Table 7.2.

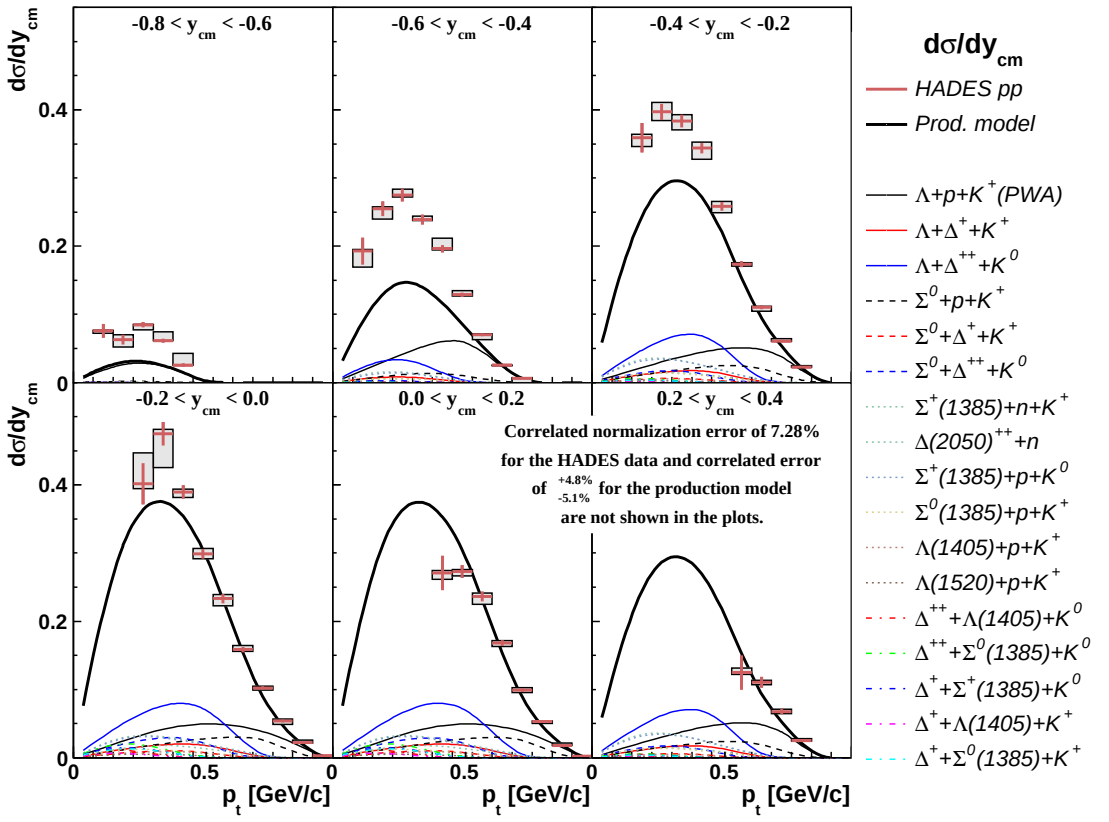

Figure 7.8: Differential comparison of corrected experimental data to the production model in the p_t-y^{cms} phase-space. Error bars of the HADES data do not include correlated errors of 7.3 %.

7.5 Comparision with the production model

Figures 7.7 and 7.8 show comparison of the corrected experimental data to the total Λ production model, as a function of *(i)* momentum p^{cms} for different polar angle $\cos\theta^{cms}$ bins, and *(ii)* transverse momentum p_t for different rapidity y^{cms} bins respectively. The red symbols depict the experimental yields, where vertical lines are the statistical errors and the grey bands are the systematic uncorrelated errors. The correlated errors of 7.28 % from the normalization uncertanites are not shown in the figure. The thick black solid curve shows the distribution resulting from the production model. The correlated error of the production model cross-section of $\sigma = 160.6\ ^{+7.7}_{-8.2}$ µb is not drawn in the plots. Colorful solid, dashed, dotted and dashed dotted lines show the contribution from the different channels. For more detailed insight into particular channels contribution, please refer to Appendix B, where the same plots in logarithmic scale are shown.

In seven of the total eight panels in Fig. 7.7 a good agreement between the model

and the experimental yields are observed for Λ momenta higher than $500\,\mathrm{MeV/c}$. In the low momentum region the model and the data diverges. In some of the pads, the trend of the experimental cross-section is rising for lower momenta wheres in the other experimental yields keep consistency with the model. In the first pad, which depicts the most backward region (with respect to the beam momentum direction) of the produced Λs, the disagreement is visible in the whole momentum range.

Similar trends are observed in the second analysed distribution from Fig. 7.8. In the mid-rapidity sector (panels on the bottom), where $p_\mathrm{t} \approx p^\mathrm{cms}$, good agreement is observed for the higher transeverse momentum range. Here however, in contrast to the $\cos\theta^\mathrm{cms}$ spectrum, the trends of the model and the data are the same over the whole transverse momentum range.

It is visible that the model underestimates the experimental yield. It therefore might be conculed that some important contributions to the total yield are either not properly described or not included at all. The other possibility is that the acceptance and efficiency calculations based on the model are not realistic.

7.6 Cross section extraction

To extract the total differential cross-section from the differential distributions of the measured Λ, a description of the phase space is required. However, HADES does not cover the full phace space region with its acceptance, what clearly can be seen in Figs. 7.2 and 7.3 when comparing the full phase space distribution to either the experimental yields or the simulation results. The best approximation of the missing area comes from the production model, though it does not agree with the experimental data in all the regions, especially in low momenta region of the p^cms-$\cos\theta^\mathrm{cms}$ distribution. However, comparison of the p_t-y^cms spectras shows that there is a converging trend for the low momenta part of the distributions. Since there is, non-trivial but still comparable correlation between the two different phase spaces at low momenta values (compare to Fig. C.5), one can safely assume that this trend will show up also in the p^cms-$\cos\theta^\mathrm{cms}$ ditribution. The same conclusion is sugested by the production model. Therefore missing bins in the experimental yields are filled with the results from the model.

To minimize the influence of the model to the total production, in the first place a assumption of the symmetric Λ production in central mass reference frame was used. Both distributions of the experimental yields were mirrored along their symmetry axes at $y = 0$ and $\cos\theta^\mathrm{cms} = 0$ respectively and merged with the original distributions. Each new bin of the new distribution was recalculated using the weighted sum of original and mirrored value:

$$\sigma = \frac{\sigma_\mathrm{o}/\delta_\mathrm{o}^2 + \sigma_\mathrm{m}/\delta_\mathrm{m}^2}{1/\delta_\mathrm{o}^2 + 1/\delta_\mathrm{m}^2}, \qquad \delta = \left(\frac{1}{\delta_\mathrm{o}^2} + \frac{1}{\delta_\mathrm{m}^2}\right)^{-1/2}, \tag{7.3}$$

Table 7.3: Summary of the cross-section extraction. All values are given in μb.

Phase-space	σ_{EXP}	σ_{SIM}	σ	δ_{stat}	δ_{syst}	δ_{model}
p^{cms}-$\cos\theta^{\mathrm{cms}}$	111.9	26.5	199.6	± 1.5	$^{+7.1}_{-8.9} \pm 8.1$	$^{+0.3}_{-0.4}$
p_{t}-y^{cms}	110.9	25.9	202.9	± 1.0	$^{+4.8}_{-5.6} \pm 8.1$	$^{+0.5}_{-0.5}$
Cross-check Analysis	194.6	—	194.6	± 4.0	$^{+7.7}_{-8.1} \pm 14.2$	—
Model	—	160.6	—	—	—	$^{+7.7}_{-8.2}$

where the subscripts o and m denote the original and mirrored bins, σ is the cross-section value in the bin and δ is the bin error.tab:diffana:cs Missing points in the spectrum were filled with information from the model. More details about this procedure is shown in Appendix C. Amount of the yield extrapoalded for each of the analyses is listed in Table 7.3.

Figure 7.9 shows the cross-section distribution for different polar angles and rapidity regions respectively. The values in the bins come from the integral of the differential phase space over all momenta within a given polar angle region, or transverse momenta within rapidity respectively, including both experimental yields and points extrapolated from the model. Values are normalized to the momentum and the transverse momentum bin size respectively.

The anisotropy coefficients $a_0 \ldots a_4$ of the Λ distribution in the p^{cms}-$\cos\theta^{\mathrm{cms}}$ variables extracted for the following parametrization ($x \equiv \cos\theta^{\mathrm{cms}}$):

$$\sigma(x) = \sigma_0 \cdot \frac{1}{2}\Big\{a_0 P_0(x) + a_2 P_2(x) + a_4 P_4(x)\Big\}, \tag{6.1}$$

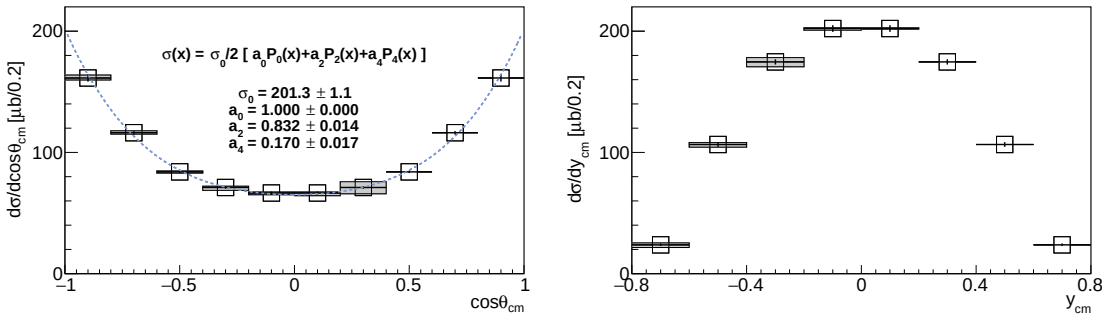

(a) $\cos\theta^{\mathrm{cms}}$ distribution. **(b)** y^{cms} distribution.

Figure 7.9: Differential cross-sections.

Table 7.4: Summary of the angular distribution extraction.

Phase-space	σ_0 [μb]	a_0	a_2	a_4
p^{cms}-$\cos\theta^{\mathrm{cms}}$	201.3 ± 1.1	1.0	0.832 ± 0.014	0.170 ± 0.017

are listed in Table 7.4.

The total cross-sections extracted for the two differential analyses are:

$$\begin{aligned} \sigma(\mathrm{pp} \to \Lambda + X) &= 199.6 \pm 1.5\, ^{+7.1}_{-8.9} \pm 8.1\, ^{+0.3}_{-0.4}\ \mu\mathrm{b}, \\ \sigma(\mathrm{pp} \to \Lambda + X) &= 202.9 \pm 1.0\, ^{+4.8}_{-5.6} \pm 8.1\, ^{+0.5}_{-0.5}\ \mu\mathrm{b}, \end{aligned} \tag{7.4}$$

for the p^{cms}-$\cos\theta^{\mathrm{cms}}$ and p_{t}-y^{cms} phase-spaces respectively. The first error specifies the statistical error of the measured experimental yields. The second and the third errors are the systematic uncertanities, described in Section 7.4. The last error is related to the total error (statistical and systematical) of the model bins, which were used to extrapolate experimental data to the full phase-space. Full list of all values and errors is given in Table 7.3. The first column specifies the phase-space. The second column shows the cross-section (c.s.) from the available experimental data, the third is the c.s. extrapolated from the model part and the fourth is the sum of both after the mirroring procedure. The fifth and the sixth column are the statistical and systematical errors from the experimental data. The last column is the error contributed from the model part.

Beside the cross-section extracted from the differential analysis, the cross-check analysis integrated over the whole phase-space was carried out simultanously. The analysis steps of the experimental data and all the steps related to the model preparation, calculating the acceptance matrix and applying the data corrections are performed exactly in the same way like presented in Fig. 7.1 and described in this thesis. The big advantage of this cross-check analysis is that no approximation of the cross-section from the model is required, though the acceptance and efficiency corrections are still model dependent. The cross-section result obtained from this data sample is equal to:

$$\sigma(\mathrm{pp} \to \Lambda + X) = 194.6 \pm 4.0\, ^{+7.7}_{-8.1} \pm 14.2\ \mu\mathrm{b}, \tag{7.5}$$

where statistical and both systematical uncertanities are obtained in the same way like in the differential analysis. Since the model is not used to extrapolate the missing phase-space after the corrections, there is no fourth error related to the model extrapolation.

The statistical errror in this data sample is four times larger than the one obtained from the differential analyses. Since the fit is performed on the whole data sample, it does not include the effects of the acceptance geometry dependency on the mass resolution.

The fit of the data oversimplifies therefore this depedency and results in the increase of the statistical and systematical errors due to worse fit converging. However, the obtained cross-section results are consistent within the errors with the values of the differential analyses. Therefore, the final cross-section was calculated by a flat averaging of the both differential analyses and has final value of:

$$\sigma(\mathrm{pp} \to \Lambda + X) = 201.3 \pm 1.3\,^{+6.0}_{-7.3} \pm 8.1\,^{+0.4}_{-0.4}\,\mu\mathrm{b}. \tag{7.6}$$

Table 7.5: Modification of the model as a result of the cross-section fitting.

pp→ reaction	cross-section [μb]	Fit results [μb]	Comments
	3-body channels		
$\Lambda \mathrm{p K}^+$	$36.26 \pm 0.43\,^{+3.55}_{-2.83}$	39.722 ± 0.030	Upper limit
$\Sigma^0 \mathrm{p K}^+$	$16.5 \pm 20\,\%$	19.80 ± 0.19	Upper limit
$\Lambda \Delta^{++} \mathrm{K}^0$	$29.45 \pm 0.08\,^{+1.67}_{-1.46} \pm 2.06$	32.10 ± 0.11	Upper limit
$\Sigma^0 \Delta^{++} \mathrm{K}^0$	$9.26 \pm 0.05\,^{+1.41}_{-0.31} \pm 0.65$	9.38 ± 1.54	
$\Lambda \Delta^{+} \mathrm{K}^+$	$9.82 \pm 20\,\%$	11.78 ± 0.16	Upper limit
$\Sigma^0 \Delta^{+} \mathrm{K}^+$	$3.27 \pm 20\,\%$	2.62 ± 1.19	Lower limit
$\Sigma(1385)^+ \mathrm{n K}^+$	$22.42 \pm 0.99 \pm 1.57\,^{+3.04}_{-2.23}$	17.905 ± 0.076	Upper limit
$\Delta(2050)^{++} \mathrm{n}$	33 % feeding for $\Sigma^* \mathrm{n K}^+$	8.82 ± 0.13	Upper limit
$\Sigma(1385)^+ \mathrm{p K}^0$	$14.05 \pm 0.05\,^{+1.79}_{-2.14} \pm 1.00$	16.101 ± 0.072	Upper limit
$\Sigma(1385)^0 \mathrm{p K}^+$	$6.0 \pm 0.48\,^{+1.94}_{-1.06}$	7.998 ± 0.069	Upper limit
$\Lambda(1405) \mathrm{p K}^+$	$9.2 \pm 0.9 \pm 0.7\,^{+3.3}_{-1.0}$	7.6 ± 5.0	Lower limit
$\Lambda(1520) \mathrm{p K}^+$	$5.6 \pm 1.1 \pm 0.4\,^{+1.1}_{-1.6}$	7.2 ± 3.4	Upper limit
$\Delta^{++} \Lambda(1405) \mathrm{K}^0$	$5.000 \pm 20\,\%$	6.0 ± 1.7	Upper limit
$\Delta^{++} \Sigma(1385)^0 \mathrm{K}^0$	$3.500 \pm 20\,\%$	4.90 ± 0.39	Upper limit
$\Delta^{+} \Sigma(1385)^+ \mathrm{K}^0$	$2.300 \pm 20\,\%$	3.22 ± 0.37	Upper limit
$\Delta^{+} \Lambda(1405) \mathrm{K}^+$	$2.300 \pm 20\,\%$	4.2 ± 1.9	Upper limit
$\Delta^{+} \Sigma(1385)^0 \mathrm{K}^+$	$2.300 \pm 20\,\%$	3.22 ± 0.39	Upper limit
	4-body channels		
$\Lambda \mathrm{p} \pi^+ \mathrm{K}^0$	$2.98 \pm 0.02\,^{+0.21}_{-1.98} \pm 0.18$	3.3 ± 1.7	Upper limit
$\Lambda \mathrm{n} \pi^+ \mathrm{K}^+$	from $\Lambda \mathrm{p} \pi^+ \mathrm{K}^0$	3.3 ± 1.7	Upper limit
$\Lambda \mathrm{p} \pi^0 \mathrm{K}^+$	from $\Lambda \mathrm{p} \pi^+ \mathrm{K}^0$	3.3 ± 1.6	Upper limit
$\Sigma^0 \mathrm{p} \pi^+ \mathrm{K}^0$	$1.34 \pm 0.02\,^{+0.10}_{-1.35} \pm 0.09$	0.12 ± 0.74	Lower limit
$\Sigma^0 \mathrm{n} \pi^+ \mathrm{K}^+$	from $\Sigma^0 \mathrm{p} \pi^+ \mathrm{K}^0$	0.0 ± 1.4	Lower limit
$\Sigma^0 \mathrm{p} \pi^0 \mathrm{K}^+$	from $\Sigma^0 \mathrm{p} \pi^+ \mathrm{K}^0$	0.0 ± 1.0	Lower limit

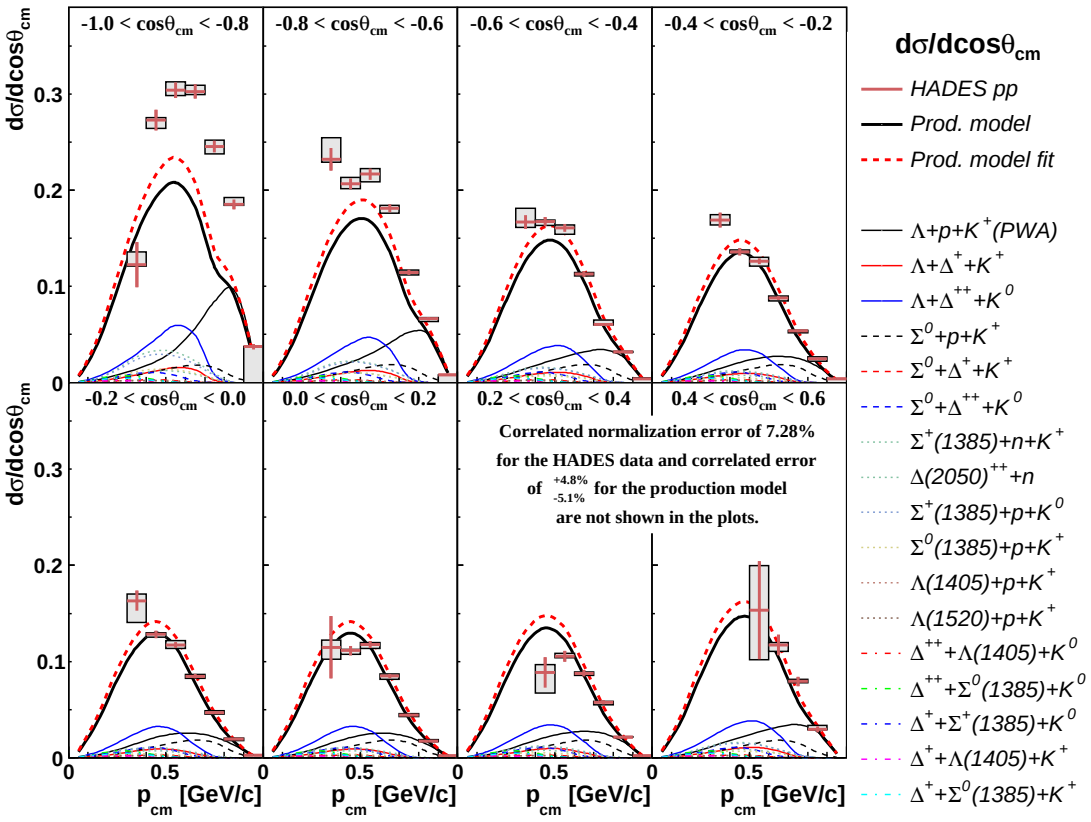

Figure 7.10: Comparision of the model and the data as described in Fig. 7.7 with additional drawing of the tunned model (dashed red curve).

7.7 Model tuning

Since there is a clear difference between the total Λ yeld predicted by the model ($160\,\mu b$) and the experimental data ($201.3\,\mu b$), all the channels contributing to the model have been varied in order to test, whether a variation of the cross-sections within the measured error allows to find better description of the experimenatl yields.

For this purpose, the angular coefficients of all channel have been fixed, and each cross-section value was varied within the total error (quadratically added statistical and systematical uncertanities) of each channel. For the four-body channels related to the Σ^0 production the limits allowed cross-section to has negative value, and for these three channels lower limit was artificially set to zero. The fit was performed simultaneously in both phase-space distributions by minimizing of the log-likelihood variable, and over all the bins where experimental data were available. Results are shown in Table 7.5. The first and the second column are the same like in Table 6.1. The third columns shows results of the fit with the fit errors, given as a new cross-section value. The fourth column

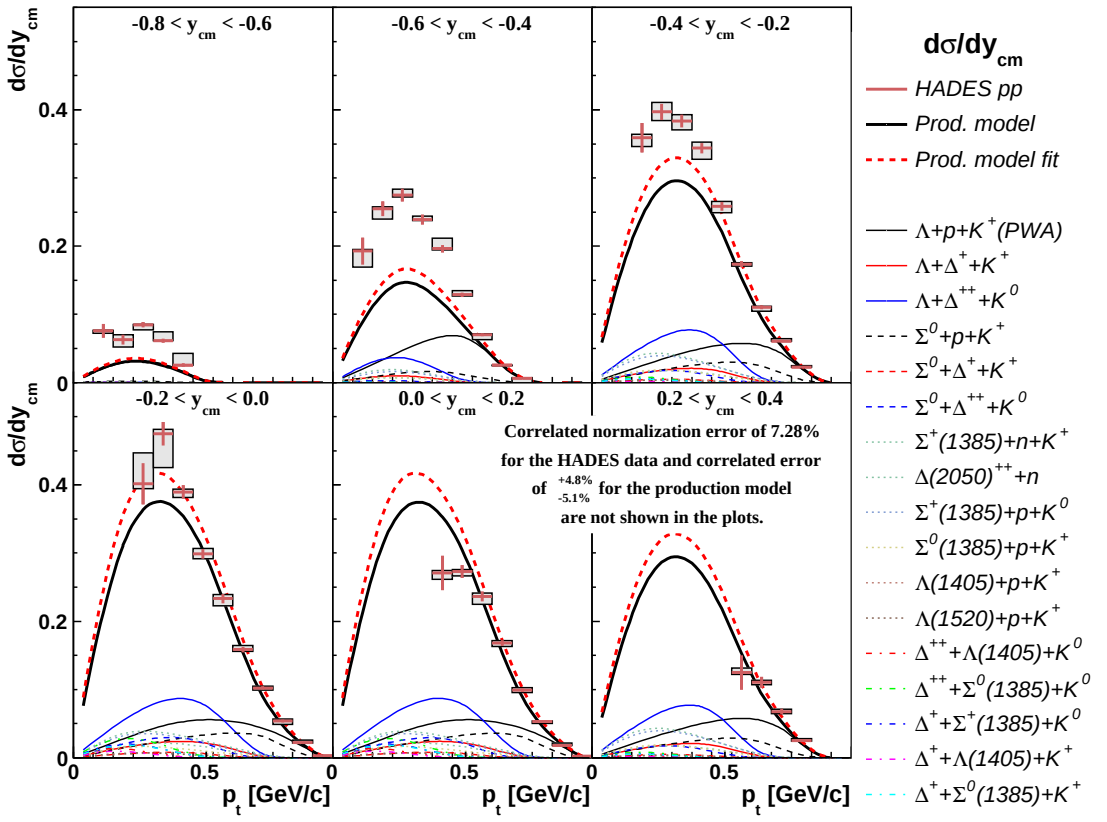

Figure 7.11: Comparision of the model and the data as described in Fig. 7.8 with additional drawing of the tunned model (dashed red curve).

gives additional comment for the fit reult, see text for details.

Due to big discrapency between the yields of the model and the data, the fits tend to push the cross-sections value to the maximum within the limits, which is visible for most of the tested channels. To compensate this rise of the cross-section in the high momentum region in all the $\cos\theta^{\mathrm{cms}}$ and y^{cms} bins, some of the channels were pushed to the lower limit. Only one channel, which is $\Sigma^0\Delta^{++}\mathrm{K}^0$ was kept inside the fitting boundaries.

The total cross-section value after the fitting was scaled by factor 1.12 and leads to the model total cross-section of $179.9\,\mu\mathrm{b}$ (errors are not evaluated) which means a rise of $19.3\,\mu\mathrm{b}$. It can be compared to the $40.7\,\mu\mathrm{b}$ difference between the model and the data and is roughly $47\,\%$ of the missing yield.

Total yields in the bins of $\cos\theta^{\mathrm{cms}}$ and y^{cms} are shown in Fig. 7.10 and Fig. 7.11 respectively.

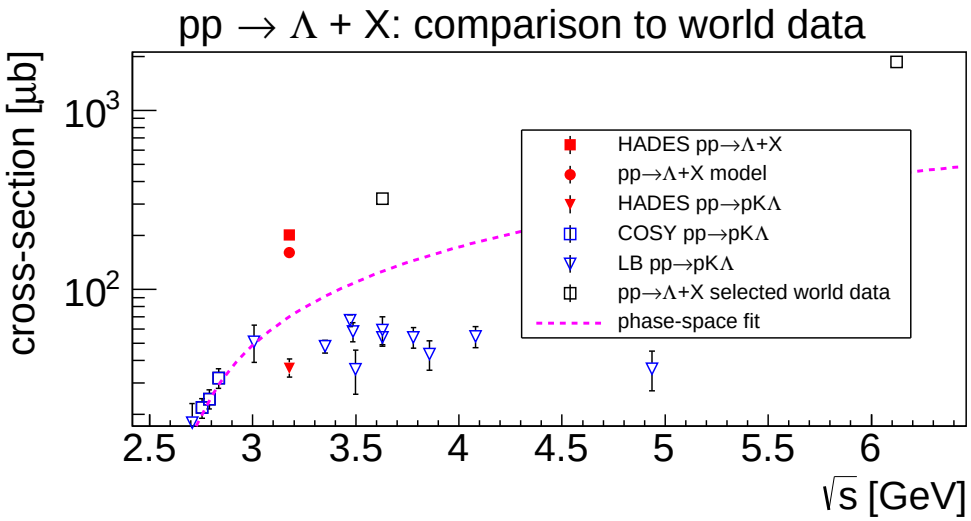

Figure 7.12: The HADES results (red square) compared to the world data. The red circle shows the cross-section extracted from the model only. The red triangle is the HADES data for $\mathrm{pK}^{+}\Lambda$ and blue triangles are data from [Bal+]. The magenta dashed curve is the phase-space parametrization of COSY-TOF data (blue open squares) [Abd+10; FW14]. Black are the other world data at low beam energies [Eis+77; Alp+76].

7.8 Summary and conclusions

The analysis of the Λ production at HADES for pp collisions with a beam kinetic energy of $3.5\,\mathrm{GeV}$ was performed. A final cross-section of $201.3 \pm 1.3\,^{+6.0}_{-7.3} \pm 8.1\,^{+0.4}_{-0.4}\,\mu\mathrm{b}$ was obtained from the total Λ production by considering the differential distribution in two different phase-space variables, and the results are presented in Table 7.3. The angular distribution of the Λ production is described by parameters listed in Eq. (6.1) and Table 7.4.

By comparing the experimental results to the production model (Figs. 7.7 and 7.8), one can conclude that the production of the Λ in the high rapidity direction is not yet well understood and described by the exclusive measurements. The first observation is that the model underestimates the experimental data. Further analysis of the missing channels could then have important influence for the model, by pinning-down the contributions of the channel where the cross-section is not known and only assumption on the isospin symmetry or complementariness to the other channel was stated. However, since yields in the mid-rapidty direction are consistent between the model and the data, further increase of the cross-sections would lead to overestimation of the yields in that regions. Therefore together with the cross-section extraction, an important factor would be the angular distribution of the missing channel. In general, we need both properties at the same time, the higher cross-section and the non-zero angular distribution of the

data.

Figure 7.12 show comparison of the results obtained in this work with the world data available for the inclusive Λ production in the pp reaction as a function of total available energy. Three red points show the experimental results of this analysis, the model and the $\mathrm{pK^+}\Lambda$ data from another HADES analysis, respectively. Empty squares are the results of $\mathrm{pp} \rightarrow \mathrm{pK^+}\Lambda$ analysis from COSY-TOF (blue) [Abd+10]. The curve presents the phase-space fit [Abd+10] to the COSY-TOF data [Abd+10; FW14] in form of

$$\sigma = C \cdot \frac{\epsilon^2}{\left(1 + \sqrt{1 + \epsilon/\alpha}\right)^2}, \tag{7.7}$$

where ϵ is the excess energy of the $\mathrm{pK^+}\Lambda$, and C and α are the fit parameters[2]. This parametrization is valid only for $\epsilon < 300\,\mathrm{MeV}$, and was shown for comparison only. In fact, at higher excess energies production of $\mathrm{pK^+}\Lambda$ saturates (see HADES and others data) and bigger phase-space opens new channel for Λ production. Experimental yields are therefore much higher above the parametrized phase-space as expected. Results from HADES are in converging trend together with the other inclusive Λ ($\mathrm{pp} \rightarrow \Lambda + X$) measurements (open black squares) from 60's and 70's, performed in the bubble chambers experiments [Eis+77; Alp+76].

[2]The fit results are $C = 2148 \pm 198\,\mu\mathrm{b}^2\,\mathrm{GeV}^{-1}$ and $\alpha = 5.034 \pm 0.810\,\mathrm{GeV}$

A
Differential fits

Here all the differential fits in the phase-space discrete bins are presented. Each single figure presents the single slice of the $\cos\theta^{\mathrm{cms}}$ or y^{cms} bins. Histograms excluded from the fit due to no signal visible in the range are denoted with the appropriate label. Each fitted histogram displays the fit parameters of Eq. (5.1) together with the errors in the following order:

1. total signal amplitude A,
2. Λ mass μ,
3. width of the first Gaussian function σ_1,
4. fourth parameters is irrelevant and always set to 0,
5. relative Gaussian fraction r,
6. width of the second Gaussian function σ_2.

Fit parameters of the background function Eq. (5.2) are not shown here. Numbers of the bottom shows the χ^2/ndf as a real value (upper line) and the integrals fraction (lower line).

A.1 Fits in p^{cms}-$\cos\theta^{\mathrm{cms}}$

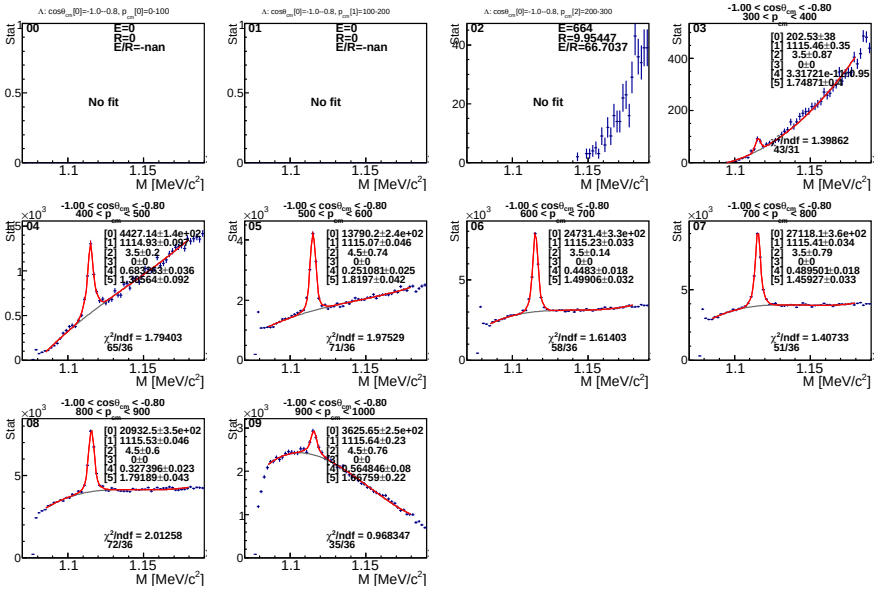

Figure A.1: p^{cms}-$\cos\theta^{\mathrm{cms}}$ distribution, $-1.0 < \cos\theta^{\mathrm{cms}} < -0.8$

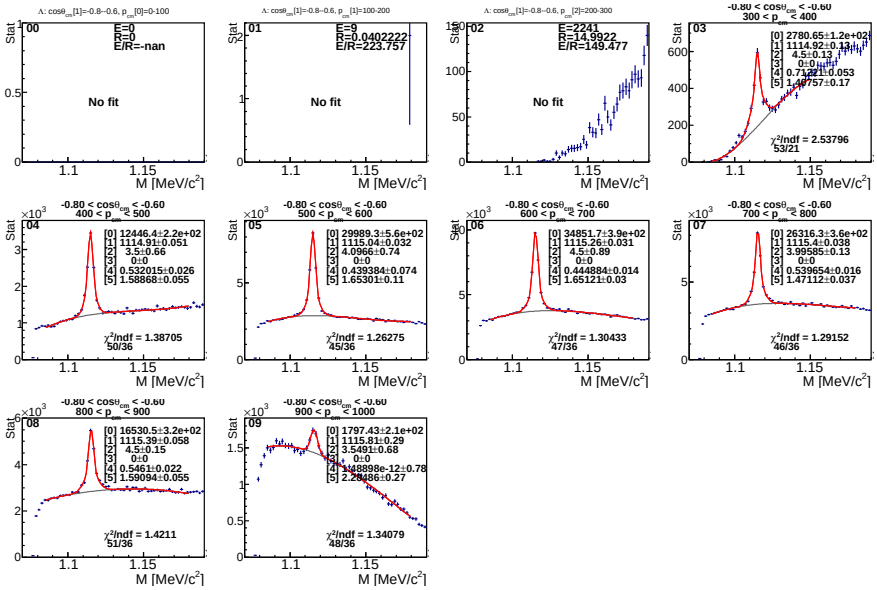

Figure A.2: p^{cms}-$\cos\theta^{\mathrm{cms}}$ distribution, $-0.8 < \cos\theta^{\mathrm{cms}} < -0.6$

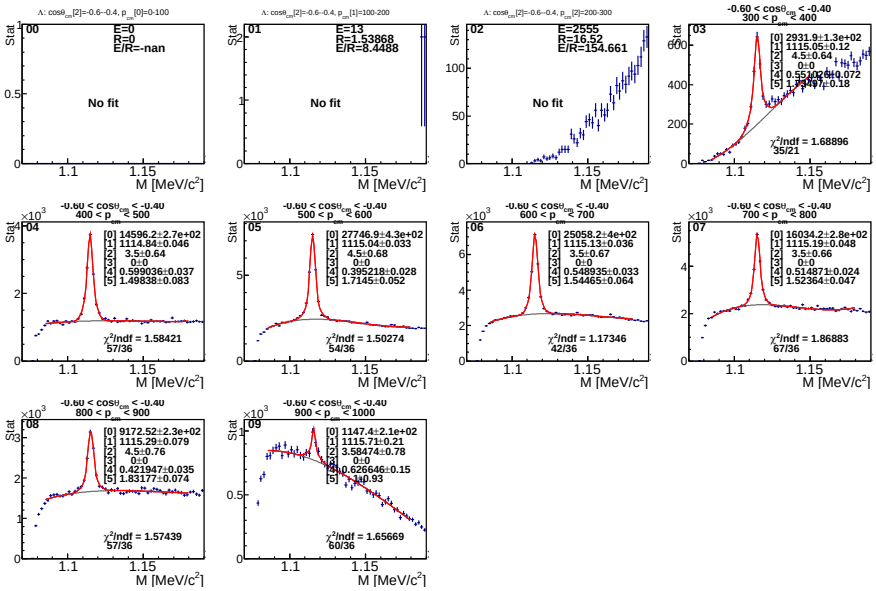

Figure A.3: p^{cms}-$\cos\theta^{\mathrm{cms}}$ distribution, $-0.6 < \cos\theta^{\mathrm{cms}} < -0.4$

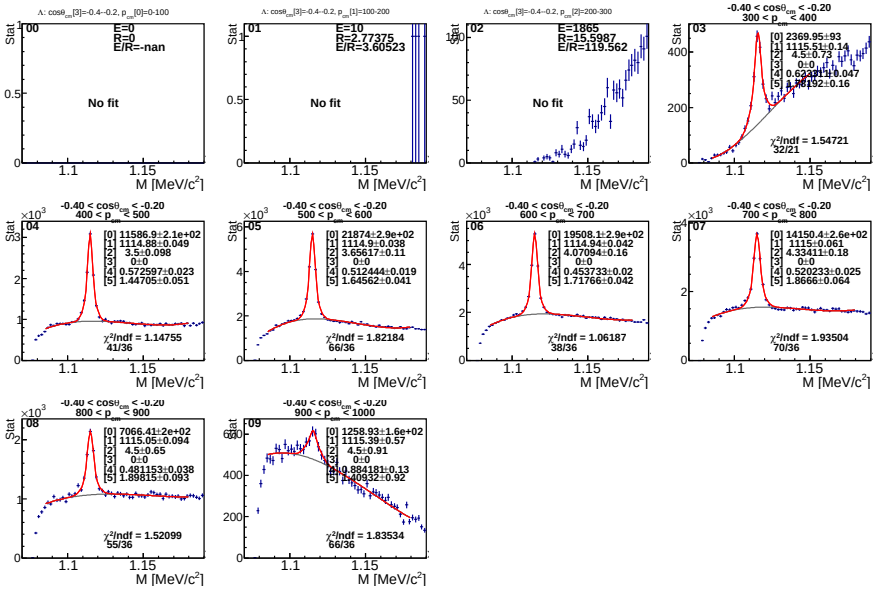

Figure A.4: p^{cms}-$\cos\theta^{\mathrm{cms}}$ distribution, $-0.4 < \cos\theta^{\mathrm{cms}} < -0.2$

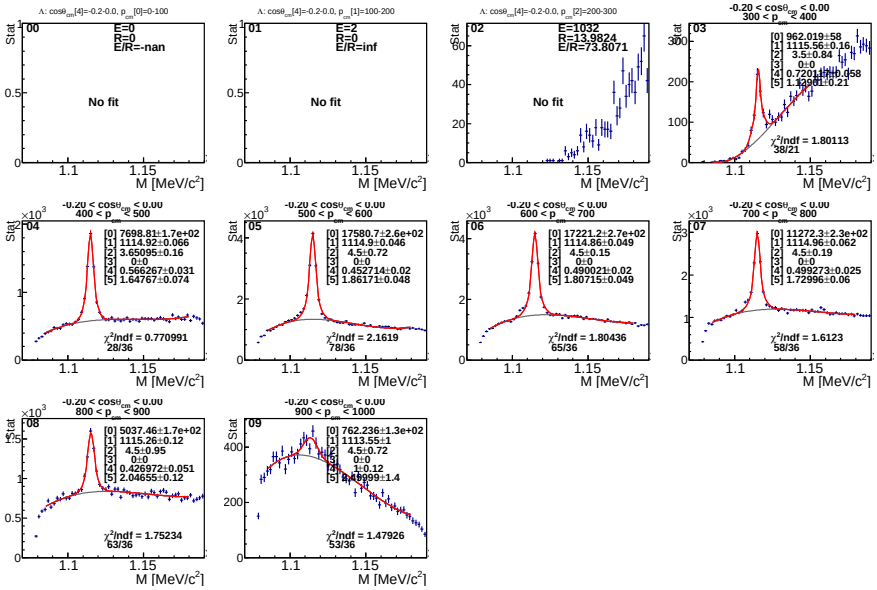

Figure A.5: p^{cms}-$\cos\theta^{\mathrm{cms}}$ distribution, $-0.2 < \cos\theta^{\mathrm{cms}} < 0.0$

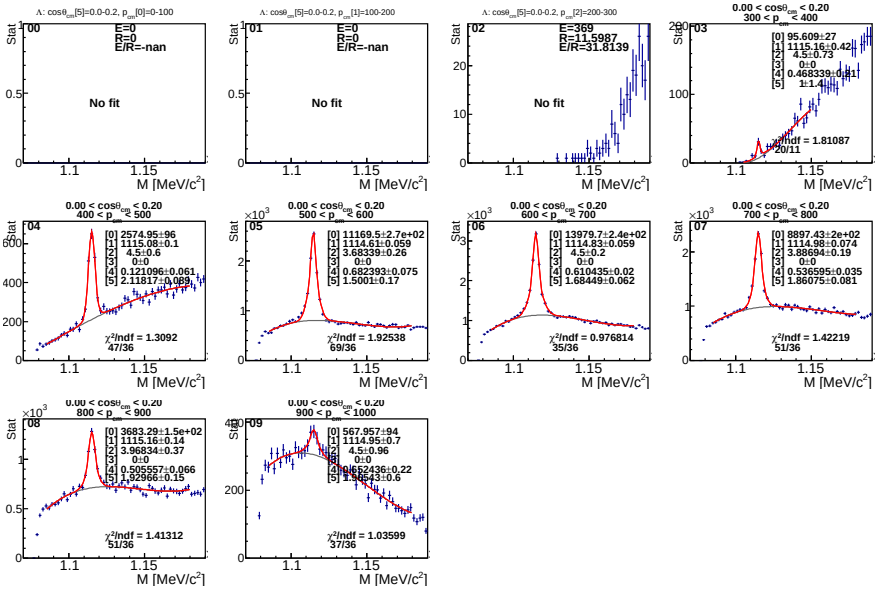

Figure A.6: p^{cms}-$\cos\theta^{\mathrm{cms}}$ distribution, $0.0 < \cos\theta^{\mathrm{cms}} < 0.2$

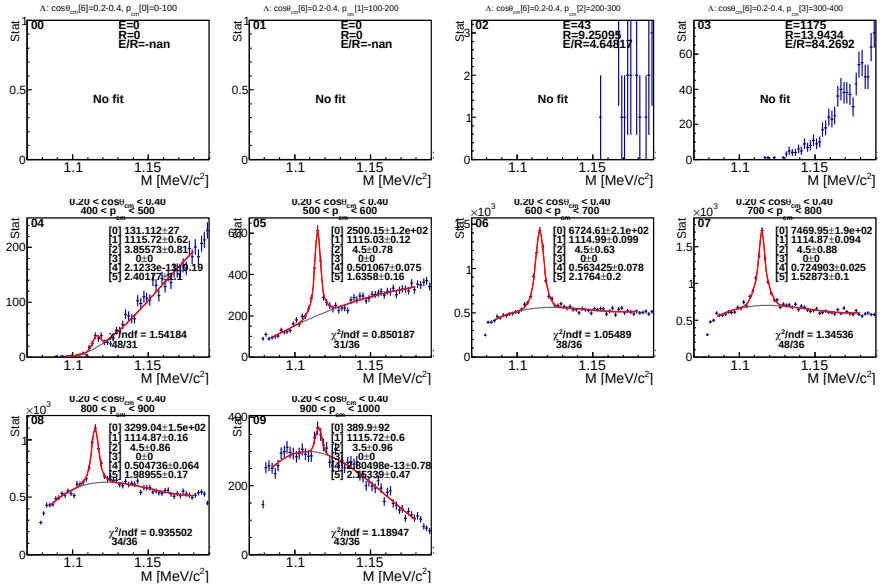

Figure A.7: p^{cms}-$\cos\theta^{\mathrm{cms}}$ distribution, $0.2 < \cos\theta^{\mathrm{cms}} < 0.4$

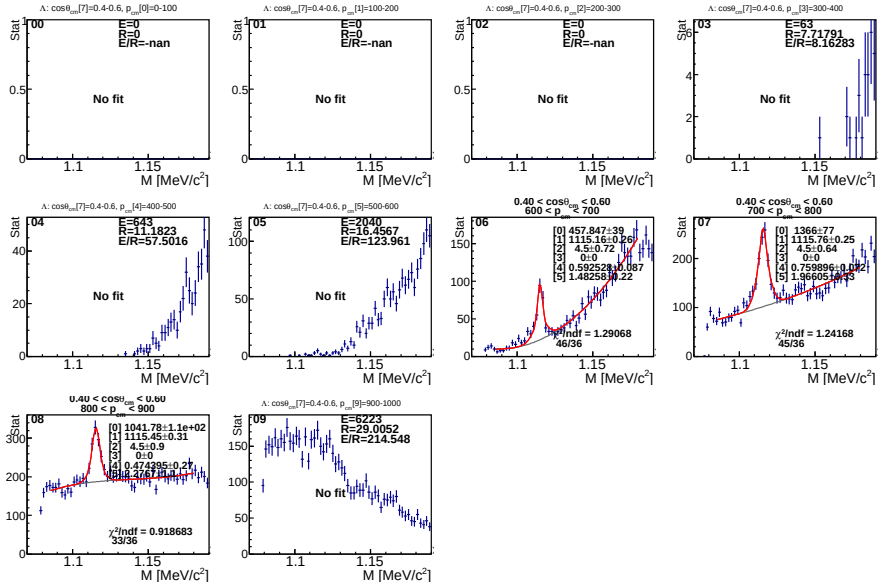

Figure A.8: p^{cms}-$\cos\theta^{\mathrm{cms}}$ distribution, $0.4 < \cos\theta^{\mathrm{cms}} < 0.6$

A.2 Fits in p_{t}-y^{cms}

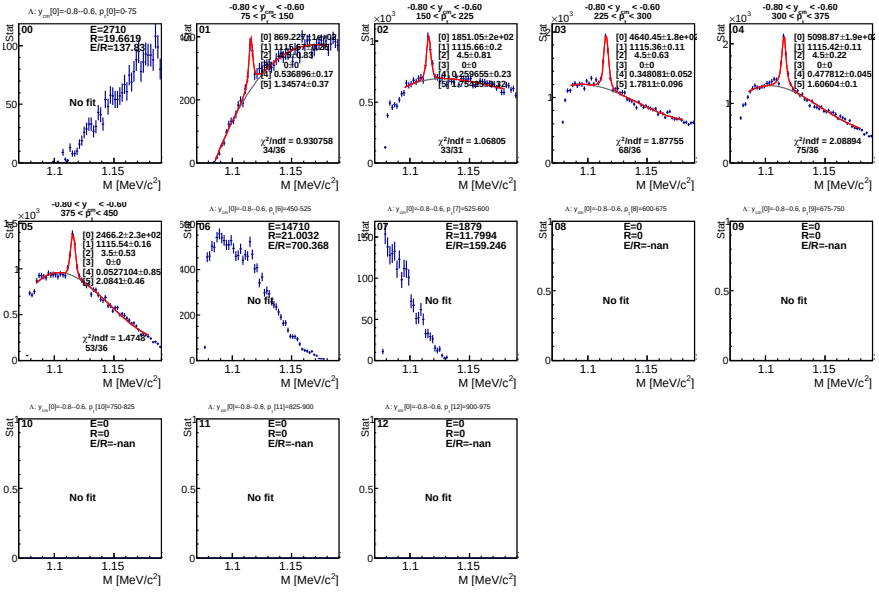

Figure A.9: p_{t}-y^{cms} distribution, $-0.8 < \cos\theta^{\mathrm{cms}} < -0.6$

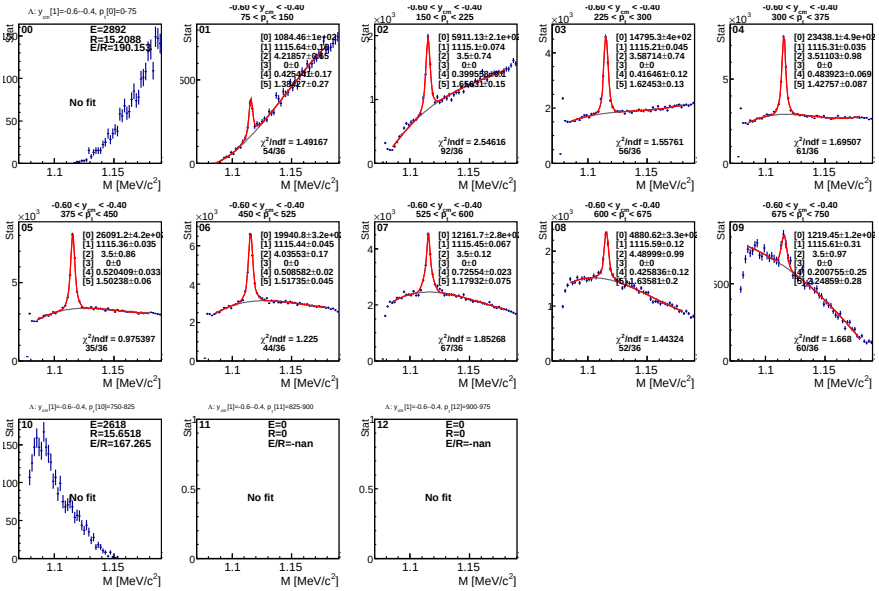

Figure A.10: p_{t}-y^{cms} distribution, $-0.6 < \cos\theta^{\mathrm{cms}} < -0.4$

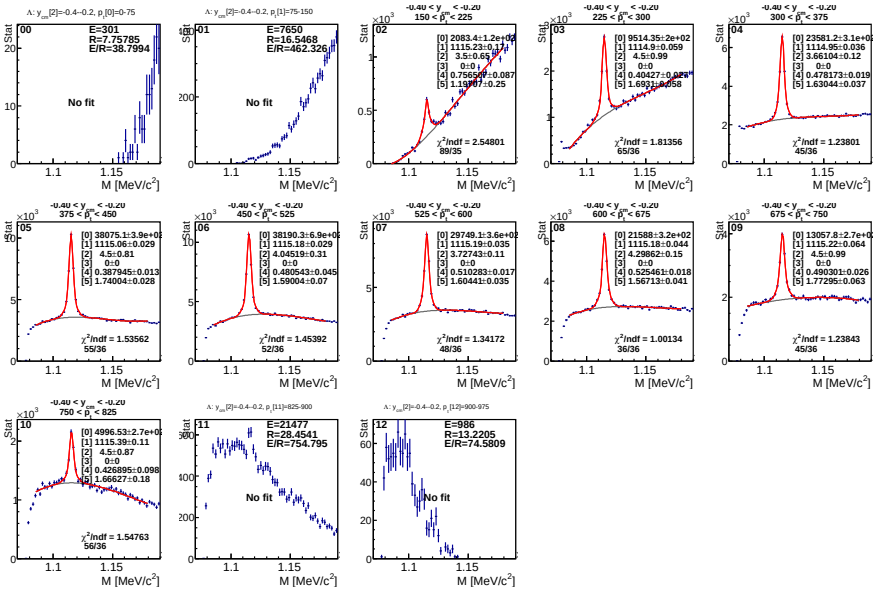

Figure A.11: p_{t}-y^{cms} distribution, $-0.4 < \cos\theta^{\mathrm{cms}} < -0.2$

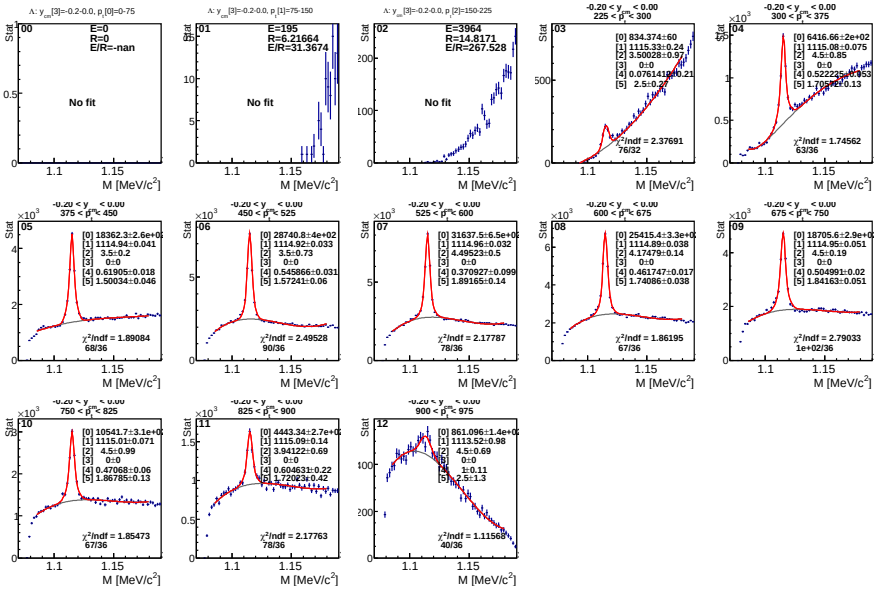

Figure A.12: p_{t}-y^{cms} distribution, $-0.2 < \cos\theta^{\mathrm{cms}} < 0.0$

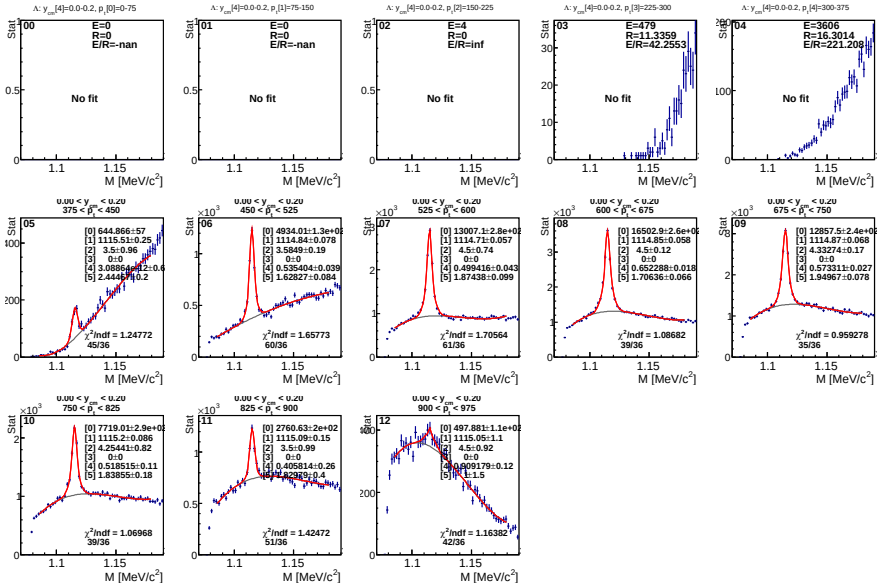

Figure A.13: p_{t}-y^{cms} distribution, $0.0 < \cos\theta^{\mathrm{cms}} < 0.2$

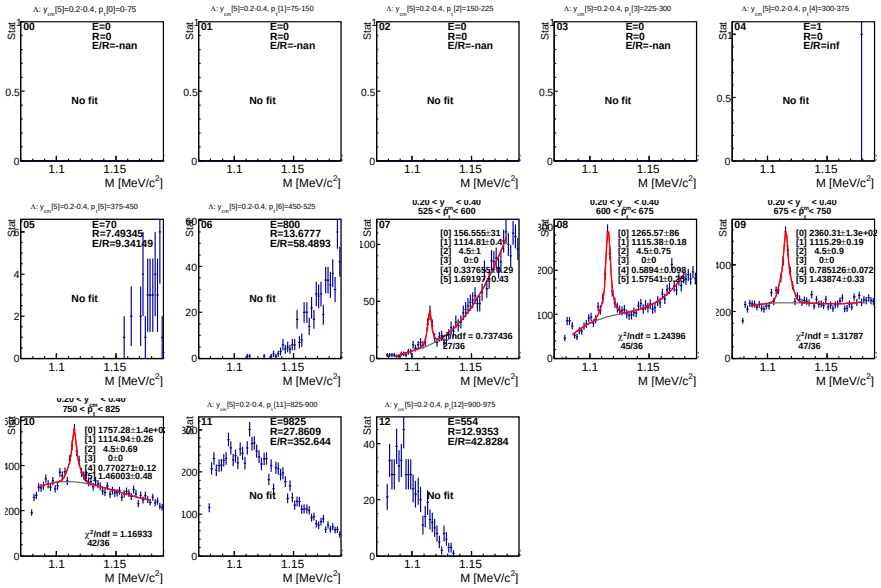

Figure A.14: p_{t}-y^{cms} distribution, $0.2 < \cos\theta^{\mathrm{cms}} < 0.4$

B

Model to experimental data comparison

This appendix shows the comparison of the experimental data with the production model as described in Section 7.5. Here, the y-axis of the figures is presented in the logaryt-mic scale what allows to have better insigh into all major contributing channels in each differential bin.

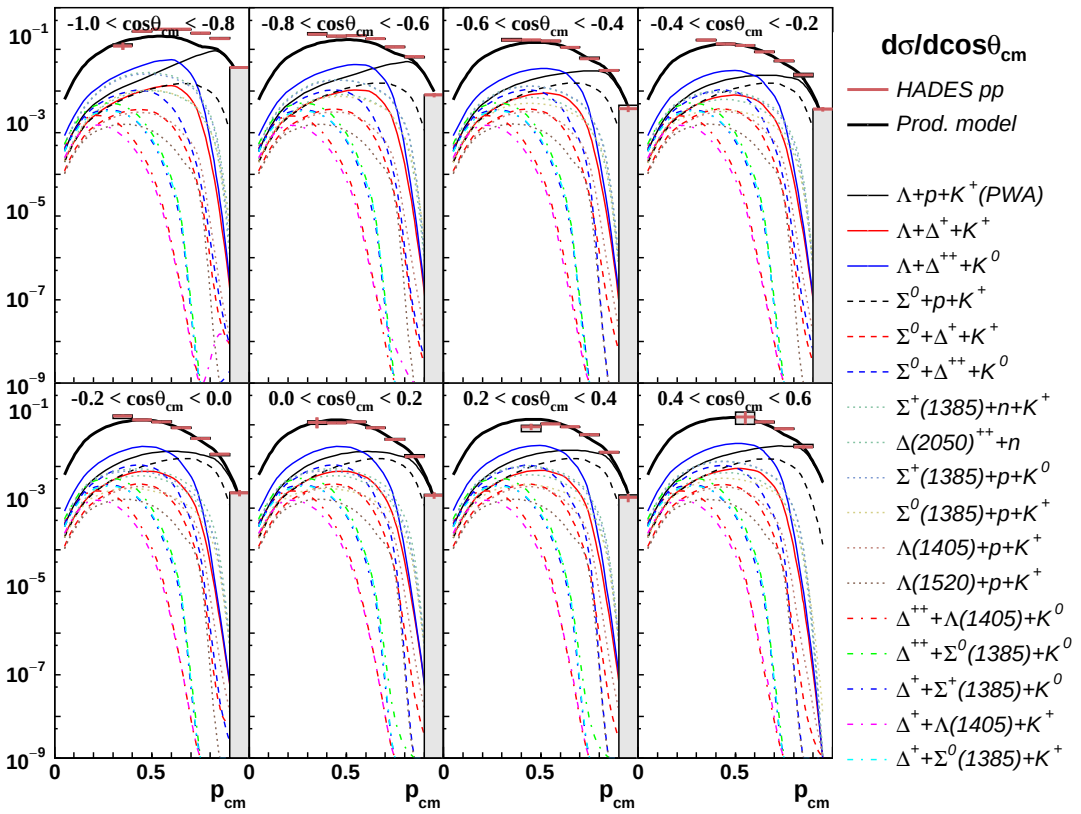

Figure B.1: Differential comparison of corrected experimental data to the production model in the p^{cms}-$\cos\theta^{\mathrm{cms}}$ phase-space. Error bars of the HADES data do not include correlated errors of $7.3\,\%$.

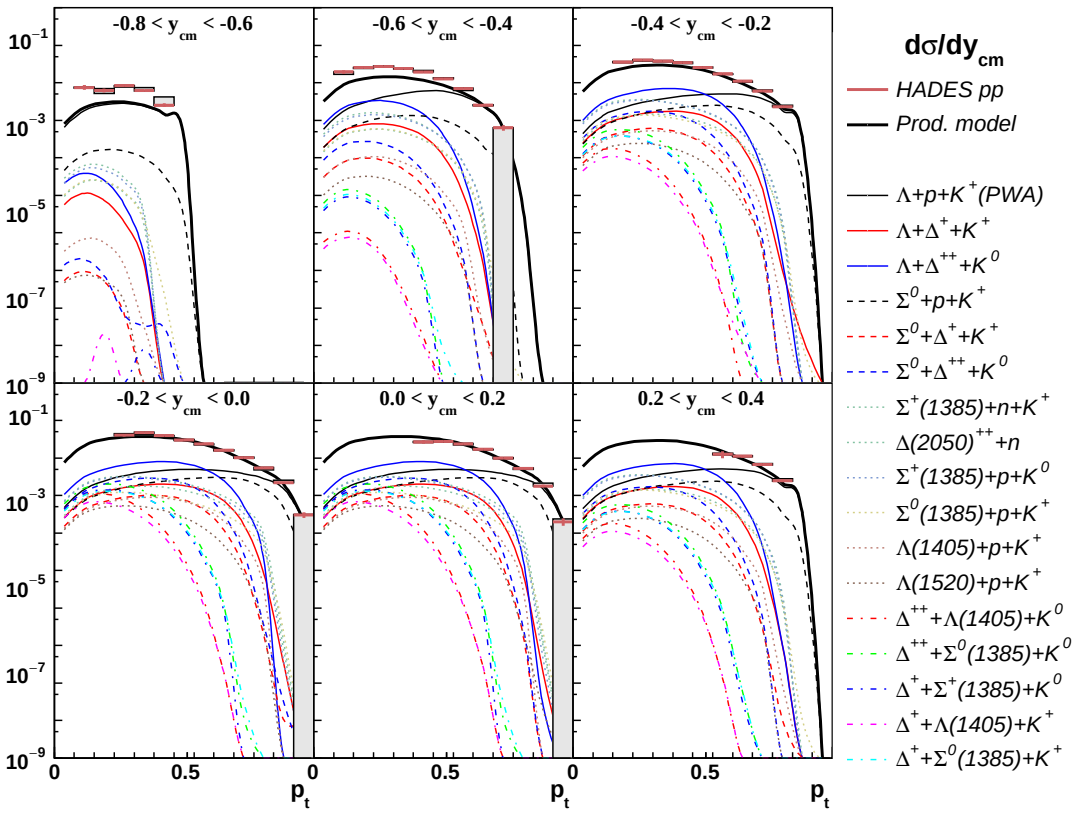

Figure B.2: Differential comparison of corrected experimental data to the production model in the p_{t}-y^{cms} phase-space. Error bars of the HADES data do not include correlated errors of $7.3\,\%$.

C

Experimental yields and simualtion model merging

Pictures in this sections show consecutive steps of the preparing full phase-space distribution to obtain differential cross-section.

In the first step, corrected distribution of the experimental phase-space (Figs. C.1a and C.3a respectively) are fileld in the backward hemisphere ($\cos\theta^{\mathrm{cms}} < 0$ and $y < 0$) with the bins from the simulation model (Figs. C.1b and C.3b respectively).

In the next step, distributions are mirrored around the symmetry axis ($\cos\theta^{\mathrm{cms}} = 0$ and $y = 0$) and the original and mirrored bins are averaged using bin errors as weights:

$$\sigma = \frac{\sigma_{\mathrm{o}}/\delta_{\mathrm{o}}^2 + \sigma_{\mathrm{m}}/\delta_{\mathrm{m}}^2}{1/\delta_{\mathrm{o}}^2 + 1/\delta_{\mathrm{m}}^2}, \qquad \delta = \left(\frac{1}{\delta_{\mathrm{o}}^2} + \frac{1}{\delta_{\mathrm{m}}^2}\right)^{-1/2}, \tag{C.1}$$

where the subscripts o and m denote the original and mirrored bins, σ is the cross-section value in the bin and δ is the bin error.

The final result is shown in Figs. C.2 and C.4 respectively.

C.1 Mirroring in the p^{cms}-$\cos\theta^{\mathrm{cms}}$ distribution

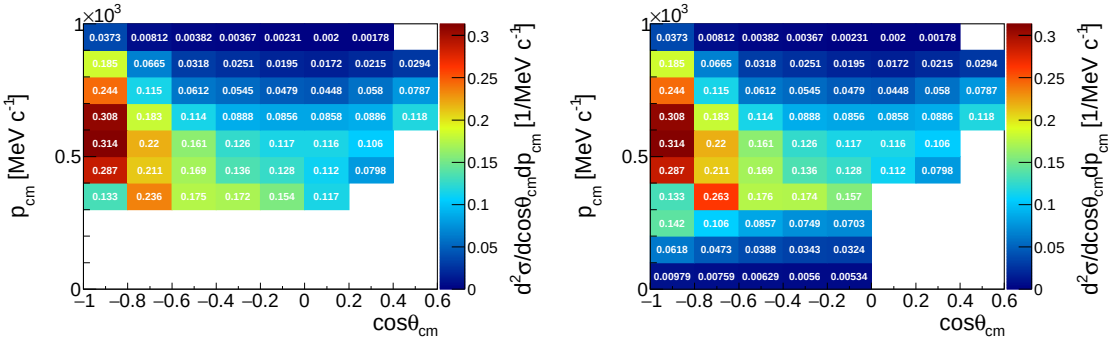

Figure C.1: Original distribution of the experimental data (a) and distribution with the missing backward hemisphere filled with the model data (b).

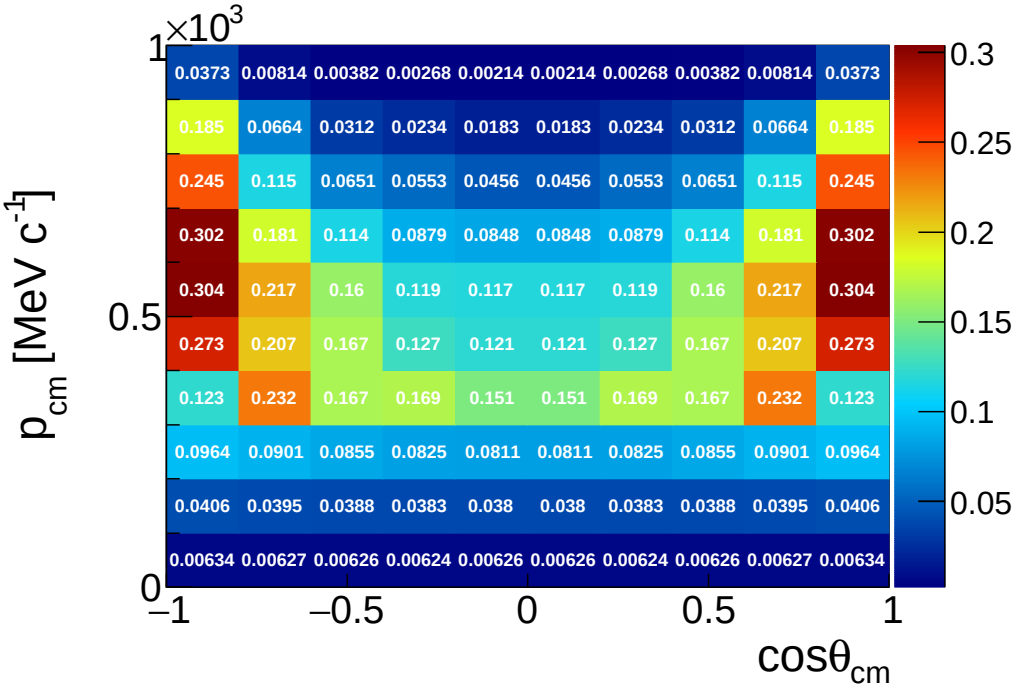

Figure C.2: Distribution from Fig. C.1b after mirroring around $\cos\theta^{\mathrm{cms}} = 0$.

C.2 Mirroring in the p_t-y^{cms} distribution

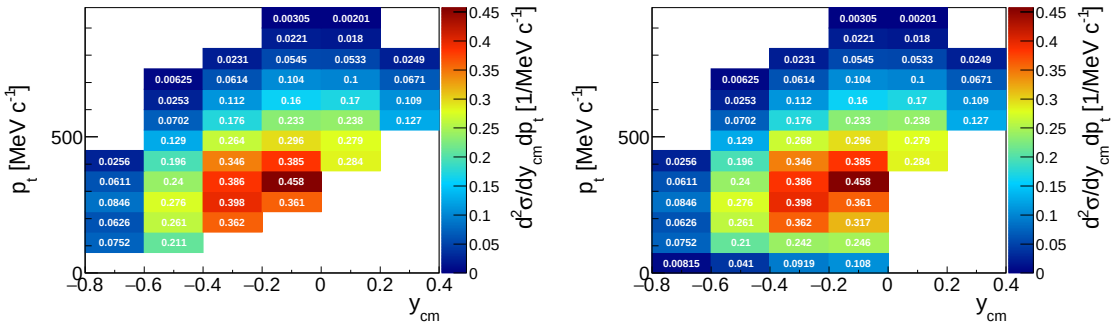

Figure C.3: Original distribution of the experimental data (a) and distribution with the missing backward hemisphere filled with the model data (b).

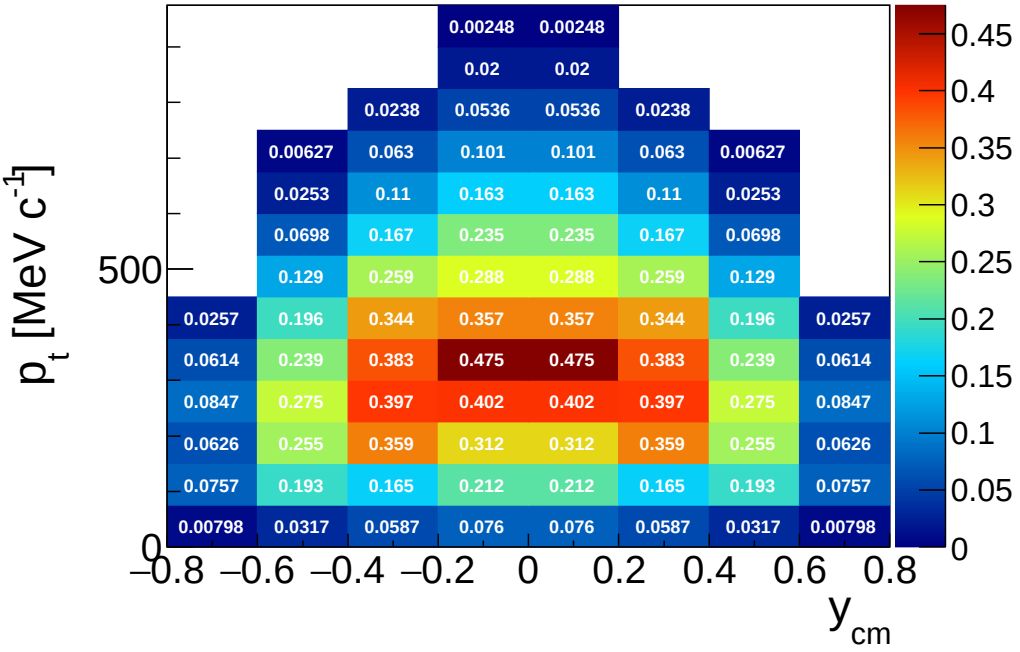

Figure C.4: Distribution from Fig. C.3b after mirroring around $y = 0$.

C.3 Distributions mapping

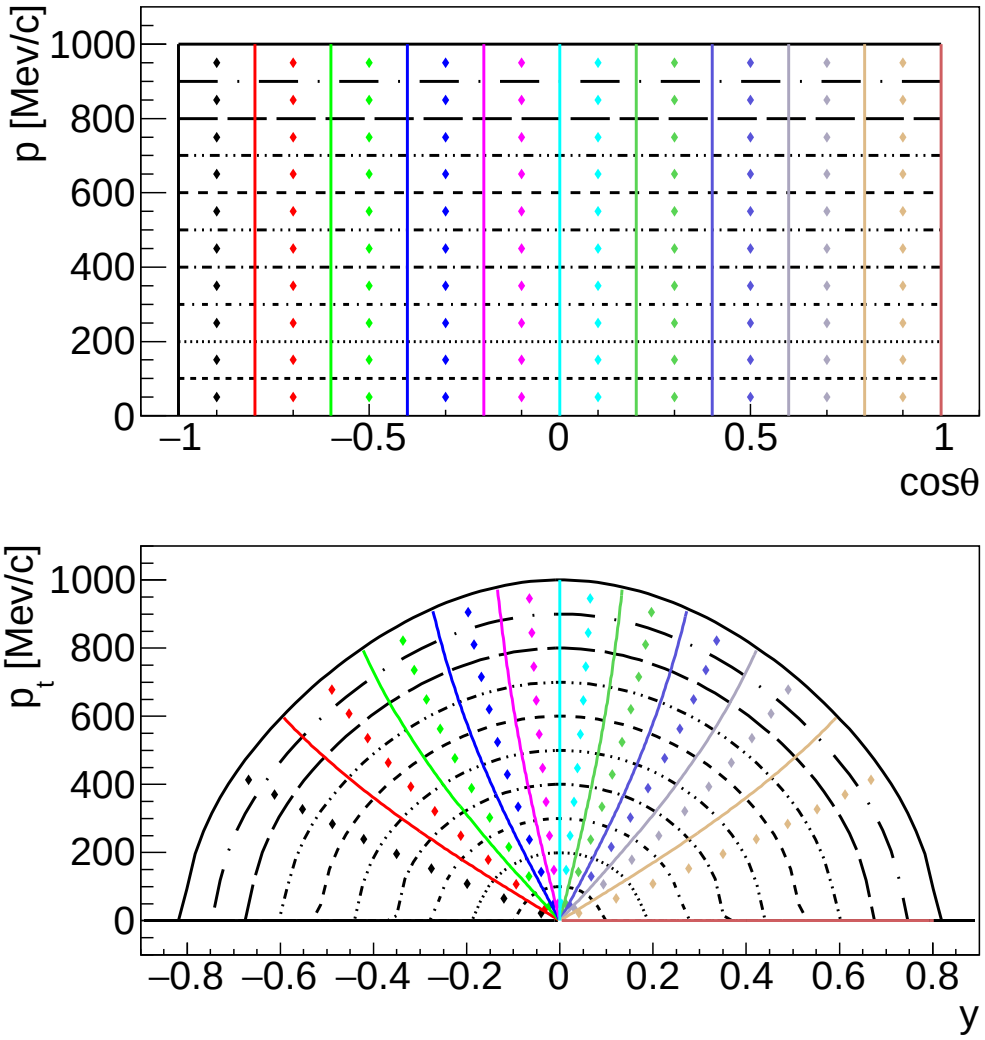

Figure C.5: Mapping of the p^{cms}-$\cos\theta^{\mathrm{cms}}$ distributins to the p_{t}-y^{cms} distributions. The black styled lines shows different momentum lines, the color lines shows different $\cos\theta^{\mathrm{cms}}$ values, and the diamonds points shows centers of the p^{cms}-$\cos\theta^{\mathrm{cms}}$ bins.

List of Figures

List of Tables

Bibliography

[Abd+10] M. Abdel-Bary et al. "Production of Λ and Σ^0 hyperons in proton-proton collisions". *Eur. Phys. J.* A46 (2010). [Erratum: Eur. Phys. J.A46,435(2010)], pp. 27–44. doi: 10.1140/epja/i2010-11023-0;10.1140/epja/i2010-11062-5 (cit. on pp. 82, 84, 104, 105).

[Aga+09] G. Agakishiev et al. "The High-Acceptance Dielectron Spectrometer HADES". *Eur. Phys. J.* A41 (2009), pp. 243–277. doi: 10.1140/epja/i2009-10807-5 (cit. on p. 71).

[Aga+10] G. Agakishiev et al. "In-medium effects on K^0 mesons in relativistic heavy-ion collisions". *Phys. Rev.* C82 (4 2010-10), p. 044907. doi: 10.1103/PhysRevC.82.044907 (cit. on pp. 67, 68).

[Aga+12] G. Agakishiev et al. "Baryonic resonances close to the $\overline{K}N$ threshold: The case of $\Sigma(1385)^+$ in pp collisions". *Phys. Rev.* C85 (3 2012-03), p. 035203. doi: 10.1103/PhysRevC.85.035203 (cit. on pp. 82, 84).

[Aga+13] G. Agakishiev et al. "Baryonic resonances close to the $\overline{K}N$ threshold: The case of $\Lambda(1405)$ in pp collisions". *Phys. Rev.* C87 (2 2013-02), p. 025201. doi: 10.1103/PhysRevC.87.025201 (cit. on pp. 82, 85).

[Aga+14a] G. Agakishiev et al. "Lambda hyperon production and polarization in collisions of p(3.5 GeV)+Nb". *Eur. Phys. J.* A50 (2014), p. 81. doi: 10.1140/epja/i2014-14081-2 (cit. on p. 68).

[Aga+14b] G. Agakishiev et al. "Associate K^0 production in $p + p$ collisions at 3.5 GeV: The role of $\Delta(1232)^{++}$". *Phys. Rev.* C90 (1 2014-07), p. 015202. doi: 10.1103/PhysRevC.90.015202 (cit. on pp. 82, 84, 85).

[Aga+14c] G. Agakishiev et al. "Medium effects in proton-induced K^0 production at 3.5 GeV". *Phys. Rev.* C90 (5 2014-11), p. 054906. doi: 10.1103/PhysRevC.90.054906 (cit. on pp. 82, 85).

[Aga+15] G. Agakishiev et al. "Partial Wave Analysis of the Reaction $p(3.5GeV) + p \rightarrow pK^+\Lambda$ to Search for the "ppK^-" Bound State". *Phys. Lett.* B742 (2015), pp. 242–248. doi: 10.1016/j.physletb.2015.01.032 (cit. on pp. 82, 83).

[Aic91] Jörg Aichelin. ""Quantum" molecular dynamics—a dynamical microscopic n-body approach to investigate fragment formation and the nuclear equation of state in heavy ion collisions ". *Physics Reports* 202.5–6 (1991), pp. 233–360. doi: 10.1016/0370-1573(91)90094-3 (cit. on p. 67).

[Ale+68] G. Alexander et al. "Study of the $\Lambda - N$ System in Low-Energy $\Lambda - p$ Elastic Scattering". *Phys. Rev.* 173 (5 1968-09), pp. 1452–1460. doi: 10.1103/PhysRev.173.1452 (cit. on p. 66).

[Alp+76] K. Alpgård et al. "A triple-Regge analysis of the inclusive reaction pp $\rightarrow$ Λ + X++ at 19 GeV/c ". *Nucl. Phys.* B105.2 (1976), pp. 349–354. doi: 10.1016/0550-3213(76)90271-6 (cit. on pp. 104, 105).

[Ant+13] John Antoniadis et al. "A Massive Pulsar in a Compact Relativistic Binary". *Science* 340.6131 (2013). doi: 10.1126/science.1233232 (cit. on p. 64).

[AS60] V. A. Ambartsumyan and G. S. Saakyan. "The degenerate superdense gas of elementary particles". *Sov. Astron. AJ* 4 (1960), pp. 192–209 (cit. on p. 63).

[BA53] Hans Albrecht Bethe and Julius Ashkin. "Passage of Radiations through Matter". *Experimental Nuclear Physics* 1 (1953). Ed. by E. Segre (cit. on p. 13).

[Bal+] A. Baldini et al. Ed. by H. Schopper. Vol. 12b. Landolt-Börnstein - Group I Elementary Particles, Nuclei and Atoms. Chap. Reaction 1 - 32. doi: 10.1007/10367917_9 (cit. on p. 104).

[Bar+99] S. Bart et al. "Σ Hyperons in the Nucleus". *Phys. Rev. Lett.* 83 (25 1999-12), pp. 5238–5241. doi: 10.1103/PhysRevLett.83.5238 (cit. on p. 66).

[BB98] Shmuel Balberg and Nir Barnea. "S-wave pairing of Λ hyperons in dense matter". *Phys. Rev.* C57 (1 1998-01), pp. 409–416. doi: 10.1103/PhysRevC.57.409 (cit. on p. 63).

[BBG12] Botta, Elena, Bressani, Tullio, and Garbarino, Gianni. "Strangeness nuclear physics: a critical review on selected topics". *Eur. Phys. J.* A48.3 (2012), p. 41. doi: 10.1140/epja/i2012-12041-6 (cit. on p. 66).

[BBS00] M. Baldo, G. F. Burgio, and H.-J. Schulze. "Hyperon stars in the Brueckner-Bethe-Goldstone theory". *Phys. Rev.* C61 (5 2000-04), p. 055801. doi: 10.1103/PhysRevC.61.055801 (cit. on p. 64).

[BBS98] M. Baldo, G. F. Burgio, and H.-J. Schulze. "Onset of hyperon formation in neutron star matter from Brueckner theory". *Phys. Rev.* C58 (6 1998-12), pp. 3688–3695. doi: 10.1103/PhysRevC.58.3688 (cit. on p. 64).

[Ben+09] M. L. Benabderrahmane et al. "Measurement of the In-Medium K^0 Inclusive Cross Section in π^--Induced Reactions at $1.15\mathrm{GeV}/c$". *Phys. Rev. Lett.* 102 (18 2009-05), p. 182501. doi: 10.1103/PhysRevLett.102.182501 (cit. on pp. 67, 68).

[Ber15] Jia Chii Berger-Chen. "The Production of K^0 in p+p Reactions at 3.5 GeV. Inclusive and Exclusive Studies with the HADES Detector". PhD thesis. TU München, 2015 (cit. on pp. 74, 76, 87).

[Bie+15] Jacek Biernat et al. *HADES Cerberos. Technical Design Report*. Tech. rep. 2015-01-15. Internal publication (cit. on pp. 8–10).

[Böt11] Stephan I. Böttcher. *Analysis of a 207 Bi spectrum measured with a Hamamatsu photo diode, a TSH310 based preamp, and the HETI IRENA*. 2011-06-01 (cit. on p. 41).

[Bro+06] AS Brogna et al. "N-XYTER, a CMOS read-out ASIC for high resolution time and amplitude measurements on high rate multi-channel counting mode neutron detectors". *Nuc. Inst. and Meth. A* 568.1 (2006), pp. 301–308 (cit. on pp. 11, 14, 39, 40).

[Bro68] Karl L. Brown. "A First And Second Order Matrix Theory For The Design Of Beam Transport Systems And Charged Particle Spectrometers." *Adv.Part.Phys.* 1 (1968), pp. 71–134 (cit. on p. 7).

[Büs+04] Büscher, M. et al. "Inclusive K+-meson production in proton-nucleus interactions". *Eur. Phys. J. A* 22.2 (2004), pp. 301–317. doi: 10.1140/epja/i2004-10036-6 (cit. on p. 68).

[Bus+12] O. Buss et al. "Transport-theoretical description of nuclear reactions ". *Physics Reports* 512.1–2 (2012). Transport-theoretical Description of Nuclear Reactions, pp. 1–124. doi: 10.1016/j.physrep.2011.12.001 (cit. on p. 83).

[BW65] John N. Bahcall and Richard A. Wolf. "Neutron Stars. I. Properties at Absolute Zero Temperature". *Phys. Rev.* 140 (5B 1965-12), B1445–B1451. doi: 10.1103/PhysRev.140.B1445 (cit. on p. 63).

[CB99] W. Cassing and E.L. Bratkovskaya. "Hadronic and electromagnetic probes of hot and dense nuclear matter1 ". *Physics Reports* 308.2–3 (1999), pp. 65–233. doi: 10.1016/S0370-1573(98)00028-3 (cit. on p. 68).

[Czo18] Jan Czochralski. "Ein neues Verfahren zur Messung der Kristallisationsgeschwindigkeit der Metalle [A new method for the measurement of the crystallization rate of metals]". *Zeitschrift für Physikalische Chemie* 92 (1918), pp. 219–221 (cit. on p. 12).

[Dar] GSI Darmstadt. url: https://www.gsi.de/en/research/accelerator_facility.htm (visited on 2015-12-04) (cit. on p. 4).

[Dem+10] Demorest P. B. et al. "A two-solar-mass neutron star measured using Shapiro delay". *Nature* 467.7319 (2010-10). 10.1038/nature09466, pp. 1081–1083. doi: 10.1038/nature09466 (cit. on p. 64).

[Dev] Analog Devices. *TMP37* (cit. on p. 34).

[Dıa+02] J. Dıaz et al. "Design and commissioning of the GSI pion beam". *Nuc. Inst. and Meth. A* 478.3 (2002), pp. 511–526 (cit. on pp. 5–8).

[DP53] M. Danysz and J. Pniewski. "Delayed disintegration of a heavy nuclear fragment". *Philos. Mag.* 44 (1953), p. 348 (cit. on p. 66).

[DR08] Janusz Dąbrowski and Jacek Ro żynek. "The (π^-, K^+) reaction on ^{28}Si and the Σ-nucleus potential". *Phys. Rev.* C78 (3 2008-09), p. 037601. doi: 10.1103/PhysRevC.78.037601 (cit. on p. 66).

[EC96] W. Ehehalt and W. Cassing. "Relativistic transport approach for nucleus-nucleus collisions from {SIS} to {SPS} energies ". *Nucl. Phys.* A602.3–4 (1996), pp. 449–486. doi: 10.1016/0375-9474(96)00097-8 (cit. on p. 68).

[Eis+71] F. Eisele et al. "Elastic $\Sigma\pm$p scattering at low energies ". *Phys. Lett.* B37.2 (1971), pp. 204–206. doi: 10.1016/0370-2693(71)90053-0 (cit. on p. 66).

[Eis+77] R.L. Eisner et al. "Λ and {K0} production in p$\uparrow$p interactions at 6 GeV/c ". *Nucl. Phys.* B123.3 (1977), pp. 361–381. doi: 10.1016/0550-3213(77)90173-0 (cit. on pp. 104, 105).

[Fri01] M. Friedl. "The CMS silicon strip tracker and its electronic readout". *Doctor Thesis* (2001) (cit. on p. 14).

[Fro+07] I. Frohlich et al. "Pluto: A Monte Carlo Simulation Tool for Hadronic Physics". *PoS* ACAT2007 (2007), p. 076 (cit. on p. 81).

[Fuk+98] T. Fukuda et al. "Cascade hypernuclei in the (K^-, K^+) reaction on ^{12}C". *Phys. Rev.* C58 (2 1998-08), pp. 1306–1309. doi: 10.1103/PhysRevC.58.1306 (cit. on p. 66).

[FW14] Göran Fäldt and Colin Wilkin. "Comparison of the near-threshold production of η- and K-mesons in proton-proton collisions". *Zeitschrift für Physik A Hadrons and Nuclei* 357.3 (2014), pp. 241–243. doi: 10.1007/s002180050239 (cit. on pp. 104, 105).

[GCG98] J. Geiss, W. Cassing, and C. Greiner. "Strangeness production in the {HSD} transport approach from {SIS} to {SPS} energies ". *Nucl. Phys.* A644.1–2 (1998), pp. 107–138. doi: 10.1016/S0375-9474(98)80011-0 (cit. on p. 68).

[Hai+13] J. Haidenbauer et al. “Hyperon–nucleon interaction at next-to-leading order in chiral effective field theory ”. *Nucl. Phys.* A915 (2013), pp. 24–58. doi: 10.1016/j.nuclphysa.2013.06.008 (cit. on p. 66).

[Har+] C. Hartnack et al. “Modelling the many-body dynamics of heavy ion collisions: Present status and future perspective”. *Eur. Phys. J.* A1.2 (), pp. 151–169. doi: 10.1007/s100500050045 (cit. on p. 67).

[Kha+00] P. Khaustov et al. “Evidence of Ξ hypernuclear production in the $^{12}\mathrm{C}(K^-, K^+)^{12}_{\Xi}\mathrm{Be}$ reaction”. *Phys. Rev.* C61 (5 2000-03), p. 054603. doi: 10.1103/PhysRevC.61.054603 (cit. on p. 66).

[KLW90] S. Klimt, M. Lutz, and W. Weise. “Chiral phase transition in the SU(3) Nambu and Jona-Lasinio model ”. *Phys. Lett.* B249.3–4 (1990), pp. 386–390. doi: 10.1016/0370-2693(90)91003-T (cit. on p. 67).

[KN86] D.B. Kaplan and A.E. Nelson. “Strange goings on in dense nucleonic matter ”. *Phys. Lett.* B175.1 (1986), pp. 57–63. doi: 10.1016/0370-2693(86)90331-X (cit. on pp. 63, 67).

[Koh+06] M. Kohno et al. “Semiclassical distorted-wave model analysis of the $(\pi^-, K^+)\Sigma$ formation inclusive spectrum”. *Phys. Rev.* C74 (6 2006-12), p. 064613. doi: 10.1103/PhysRevC.74.064613 (cit. on p. 66).

[Lal09] Rafał Lalik. “Testing modules for multichannel, self-triggering integrated chip n-XYTER dedicated for detector readout in experiments at GSI/FAIR”. MA thesis. Kraków, 2009-12 (cit. on p. 26).

[Lan44] Lev Landau. “On the energy loss of fast particles by ionization”. *J. Phys. (USSR)* 8 (1944) (cit. on pp. 14, 21).

[LLB97] G.Q. Li, C.-H. Lee, and G.E. Brown. “Kaons in dense matter, kaon production in heavy-ion collisions, and kaon condensation in neutron stars ”. *Nucl. Phys.* A625.1–2 (1997), pp. 372–434. doi: 10.1016/S0375-9474(97)00489-2 (cit. on p. 63).

[Lon+15] Diego Lonardoni et al. “Hyperon Puzzle: Hints from Quantum Monte Carlo Calculations”. *Phys. Rev. Lett.* 114 (9 2015-03), p. 092301. doi: 10.1103/PhysRevLett.114.092301 (cit. on p. 65).

[Lou13] Philip Dominic Louis. “Development of a cooling system for a silicon detector”. TU München, 2013 (cit. on p. 32).

[Lut07] Gerhard Lutz. *Semiconductor radiation detectors device physics*. Berlin New York: Springer, 2007 (cit. on p. 12).

[MDG88] D. J. Millener, C. B. Dover, and A. Gal. “Λ -nucleus single-particle potentials”. *Phys. Rev.* C38 (6 1988-12), pp. 2700–2708. doi: 10.1103/PhysRevC.38.2700 (cit. on p. 66).

[Mer] Stefano Meroli. *Two growth techniques for mono-crystalline silicon: Czochralski vs Float Zone.* url: http://meroli.web.cern.ch/meroli/Lecture_silicon_floatzone_czochralski.html (cit. on p. 12).

[Mesa] Mesytec. *Mesytec MHV-4*. url: http://www.mesytec.com/datasheets/MHV-4.pdf (cit. on p. 23).

[Mesb] Mesytec. *Mesytec MPR16*. url: http://www.mesytec.com/datasheets/MPR16.pdf (cit. on p. 21).

[Mic] Micron Semiconductor Ltd. url: http://www.micronsemiconductor.co.uk (cit. on p. 20).

[Mig72] A B Migdal. "Vacuum Stability and Limiting Fields". *Soviet Physics Uspekhi* 14.6 (1972), p. 813 (cit. on p. 63).

[Mil07] D.J. Millener. "Topics in Strangeness Nuclear Physics". Ed. by P. Bydžovský, J. Mareš, and A. Gal. Berlin, Heidelberg: Springer Berlin Heidelberg, 2007. Chap. Hypernuclear Gamma-Ray Spectroscopy and the Structure of p-shell Nuclei and Hypernuclei, pp. 31–79. doi: 10.1007/978-3-540-72039-3_2 (cit. on p. 66).

[NIS15] NIST. *Composition of kapton polyimide film*. 2015. url: http://physics.nist.gov/cgi-bin/Star/compos.pl?matno=179 (visited on 2015-11-10) (cit. on p. 78).

[NK87] Ann E. Nelson and David B. Kaplan. "Strange condensate realignment in relativistic heavy ion collisions ". *Phys. Lett.* B192.1–2 (1987), pp. 193–197. doi: 10.1016/0370-2693(87)91166-X (cit. on pp. 63, 67).

[Oli+14] K. A. Olive et al. "Review of Particle Physics". *Chin. Phys.* C38 (2014), p. 090001. doi: 10.1088/1674-1137/38/9/090001 (cit. on pp. 13, 64, 74).

[Pie+10] J. Pietraszko et al. "Diamonds as timing detectors for minimum-ionizing particles: The HADES proton-beam monitor and START signal detectors for time of flight measurements". *Nuc. Inst. and Meth. A* 618.1–3 (2010), pp. 121–123. doi: 10.1016/j.nima.2010.02.113 (cit. on p. 49).

[RC10] Anar Rustamov and The HADES Collaboration. "Inclusive meson production in 3.5 GeV pp collisions studied with the HADES spectrometer". *AIP Conference Proceedings* 1257.1 (2010), pp. 736–740. doi: 10.1063/1.3483432 (cit. on p. 94).

[Rei50] John R. Reitz. "The Effect of Screening on Beta-Ray Spectra and Internal Conversion". *Phys. Rev.* 77 (1 1950-01), pp. 10–18. doi: 10.1103/PhysRev.77.10 (cit. on p. 66).

[Rio97] Michael Riordan. *Crystal fire : the birth of the information age*. New York: Norton, 1997 (cit. on p. 12).

[Sai] Jogender Saini. *CBM-MUCH readout electronics tests, results and design parameters and configurations* (cit. on pp. 51, 53).

[Sam] Samtec. url: https://wwws.samtec.com/ (cit. on p. 21).

[Saw72] R. F. Sawyer. "Condensed π^- Phase in Neutron-Star Matter". *Phys. Rev. Lett.* 29 (6 1972-08), pp. 382–385. doi: 10.1103/PhysRevLett.29.382 (cit. on p. 63).

[Sca72] D. J. Scalapino. "π^- Condensate in Dense Nuclear Matter". *Phys. Rev. Lett.* 29 (6 1972-08), pp. 386–388. doi: 10.1103/PhysRevLett.29.386 (cit. on p. 63).

[Sch13] Tobias Schmitt. "Tracking studies with silicon detectors for the HADES Pion Tracker". TU München, 2013 (cit. on p. 42).

[Sec+68] B. Sechi-Zorn et al. "Low-Energy Λ-Proton Elastic Scattering". *Phys. Rev.* 175 (5 1968-11), pp. 1735–1740. doi: 10.1103/PhysRev.175.1735 (cit. on p. 66).

[Sie13] Johannes Siebenson. "Strange baryonic resonances below the KN threshold - Results from $p+p$ reactions at the HADES experiment". PhD thesis. TU München, 2013 (cit. on pp. 21–23).

[SMB97] Jürgen Schaffner-Bielich, Igor N. Mishustin, and Jakob Bondorf. "In-medium kaon production at the mean-field level ". *Nucl. Phys.* A625.1–2 (1997), pp. 325–346. doi: 10.1016/S0375-9474(97)81464-9 (cit. on p. 67).

[Sol08] Hans Christian Soltviet. *STATUS n-XYTER engineering run*. 2008 (cit. on p. 33).

[Sor+13] I. Sorokin et al. "Transconductance calibration of n-XYTER 1.0 readout ASIC". *Nuc. Inst. and Meth. A* A714 (2013), pp. 136–140. doi: 10.1016/j.nima.2013.02.013 (cit. on p. 41).

[SR11] H.-J. Schulze and T. Rijken. "Maximum mass of hyperon stars with the Nijmegen ESC08 model". *Phys. Rev.* C84 (3 2011-09), p. 035801. doi: 10.1103/PhysRevC.84.035801 (cit. on p. 64).

[ST83] Stuart L. Shapiro and Saul A. Teukolsky. *Black Holes, White Dwarfs, and Neutron Stars: The Physics of Compact Objects*. Wiley-VCH, 1983-05, p. 664 (cit. on p. 63).

[Sysa] SysCore. *ROC - SysCore Board V2 and V2.2*. url: https://cbm-wiki.gsi.de/foswiki/bin/view/NXYTER/SysCoreV2 (cit. on p. 27).

[Sysb] SysCore. *The nXYTER Read Out Controller – SysCore*. url: http://www.rz.uni-frankfurt.de/39888789/syscore (visited on 2016-02-14) (cit. on p. 27).

[Tak+01] H. Takahashi et al. "Observation of a ${}^{6}_{\Lambda\Lambda}He$ Double Hypernucleus". *Phys. Rev. Lett.* 87 (21 2001-11), p. 212502. doi: 10.1103/PhysRevLett.87.212502 (cit. on p. 66).

[The+14] Ch. Theisen et al. "Musett: A segmented Si array for Recoil-Decay-Tagging studies at VAMOS". *Nuc. Inst. and Meth. A* 747 (2014), pp. 69–80. doi: 10.1016/j.nima.2014.02.016 (cit. on p. 20).

[Tra+11] M. Traxler et al. "A compact system for high precision time measurements ($<$ 14 ps RMS) and integrated data acquisition for a large number of channels". *Journal of Instrumentation* 6.12 (2011), p. C12004 (cit. on p. 11).

[Trb] Trb. *TRB Home Page*. url: http://trb.gsi.de (cit. on p. 26).

[Tru] Ulrich Trunk. *n-XYTER, a DETNI Readout Chip*. Tech. rep. (cit. on p. 15).

[TST97] Kazuo Tsushima, Alexander Sibirtsev, and Anthony William Thomas. "Resonance model study of strangeness production in pp collisions". *Phys. Lett.* B390.1–4 (1997), pp. 29–35. doi: 10.1016/S0370-2693(96)01391-3 (cit. on pp. 83, 84).

[Tsu+99] Kazuo Tsushima et al. "Resonance model study of kaon production in baryon baryon reactions for heavy ion collisions". *Phys. Rev.* C59 (1999). [Erratum: Phys. Rev.C61,029903(2000)], pp. 369–387. doi: 10.1103/PhysRevC.61.029903;10.1103/PhysRevC.59.369 (cit. on pp. 83, 84).

[VDA+14] V.D.Aksinenko et al. *Strangeness in nucleon and nuclei. The HyperNIS project*. 2014 (cit. on p. 66).

[Vid+00] I. Vidaña et al. "Hyperon-hyperon interactions and properties of neutron star matter". *Phys. Rev.* C62 (3 2000-07), p. 035801. doi: 10.1103/PhysRevC.62.035801 (cit. on p. 64).

[Vid+11] I. Vidaña et al. "Estimation of the effect of hyperonic three-body forces on the maximum mass of neutron stars". *EPL (Europhysics Letters)* 94.1 (2011), p. 11002 (cit. on p. 65).

[WCS12] S. Weissenborn, D. Chatterjee, and J. Schaffner-Bielich. "Hyperons and massive neutron stars: The role of hyperon potentials ". *Nucl. Phys.* A881 (2012). Progress in Strangeness Nuclear Physics, pp. 62–77. doi: 10.1016/j.nuclphysa.2012.02.012 (cit. on pp. 63, 65).

[Web01] Fridolin Weber. "Strangeness in neutron stars". *J. Phys. G* 27.3 (2001), p. 465 (cit. on p. 64).

[Web99] Fritz W. Weber. *Pulsars as Astrophysical Laboratories for Nuclear and Particle Physics. Studies in High Energy Physics, Cosmology, and Gravitation*. Inst of Physics Pub, 1999-05, p. 700 (cit. on p. 63).

[Wir13] Joana Wirth. “Development of a cooling system for a silicon particle detector”. TU München, 2013 (cit. on p. 32).

[Wir15] Joana Wirth. “Development of a self-triggered detector system for the detection of secondary pion beams”. MA thesis. TU München, 2015 (cit. on p. 58).

[Yam+15] Y Yamamoto et al. “Hyperon-mixed neutron star with universal many-body repulsion”. *Pacs* 216560 (2015). doi: 10.1140/epja/i2016-16019-0 (cit. on p. 65).